Geophysical Observations of the 24 September 2023 OSIRIS-REx Sample Return Capsule Re-Entry

Elizabeth A. Silber[1,*], Daniel C. Bowman[2], Chris G. Carr[3], David P. Eisenberg[4], Brian R. Elbing[5], Benjamin Fernando[6], Milton A. Garcés[7,8], Robert Haaser[9], Siddharth Krishnamoorthy[10], Charles A. Langston[11], Yasuhiro Nishikawa[12], Jeremy Webster[3], Jacob F. Anderson[13], Stephen Arrowsmith[14], Sonia Bazargan[11], Luke Beardslee[15], Brant Beck[4], Jordan W. Bishop[3], Philip Blom[3], Grant Bracht[4], David L. Chichester[16], Anthony Christe[17], Jacob Clarke[14], Kenneth Cummins[18], James Cutts[10], Lisa Danielson[3], Carly Donahue[3], Kenneth Eack[9], Michael Fleigle[2], Douglas Fox[5], Ashish Goel[10], David Green[19], Yuta Hasumi[12], Chris Hayward[14], Dan Hicks[20], Jay Hix[16], Stephen Horton[11], Emalee Hough[5], David P. Huber[21], Madeline A. Hunt[13], Jennifer Inman[22], S. M. Ariful Islam[11], Jacob Izraelevitz[10], Jamey D. Jacob[5], James Johnson[16], Real J. KC[5], Attila Komjathy[10], Eric Lam[23], Justin LaPierre[24], Kevin Lewis[6], Richard D. Lewis[25], Patrick Liu[23], Léo Martire[10], Meaghan McCleary[22], Elisa A. McGhee[26], Ipsita Mitra[11], Amitabh Nag[9], Luis Ocampo Giraldo[16], Karen Pearson[27], Mathieu Plaisir[18], Sarah K. Popenhagen[7], Hamid Rassoul[18], Miro Ronac Giannone[1,14], Mirza Samnani[10], Nicholas Schmerr[28], Kate Spillman[5], Girish Srinivas[4], Samuel K. Takazawa[7], Alex Tempert[18], Reagan Turley[28], Cory Van Beek[4], Loïc Viens[3], Owen A. Walsh[13], Nathan Weinstein[4], Robert White[29], Brian Williams[7], Trevor C. Wilson[5], Shirin Wyckoff[7], Masa-yuki Yamamoto[12], Zachary Yap[5], Tyler Yoshiyama[7], Cleat Zeiler[29]

[1]Sandia National Laboratories, Geophysics, Albuquerque, NM, 87123, USA
[2]Sandia National Laboratories, Geophysical Detection Programs, Albuquerque, NM, 87123, USA
[3]Los Alamos National Laboratory, Earth and Environmental Sciences Division, PO Box 1663, Los Alamos, NM, 87544, USA
[4]TDA Research Inc, 12345 W 52nd Avenue, Wheat Ridge, CO, 80033, USA
[5]Oklahoma State University, Mechanical and Aerospace Engineering, Stillwater, OK, 74078, USA
[6]Johns Hopkins University, Department of Earth and Planetary Sciences, Baltimore, MD, 21218, USA
[7]University of Hawaii, Infrasound Lab, 73970 Makako Bay Drive 205, Kailua-Kona, HI, 96740, USA
[8]University of Hawaii, Applied Research Lab, 73970 Makako Bay Drive 117, Kailua-Kona, HI, 96740, USA
[9]Los Alamos National Laboratory, ISR-2, P.O. Box 1663, MS-B241, Los Alamos, NM, 87545, USA
[10]NASA Jet Propulsion Laboratory, California Institute of Technology, 4800 Oak Grove Drive, Pasadena, CA, 91109, USA
[11]University of Memphis, Center for Earthquake Research and Information, 3876 Central Ave., Ste. 1, Memphis, TN, 38152, USA
[12]Kochi University of Technology, School of Systems Engineering, 185 Miyanokuchi, Tosayamada, Kami, Kochi, 7828502, Japan
[13]Boise State University, Geosciences, 1910 University Dr, Boise, ID, 83725, USA
[14]Southern Methodist University, Earth Sciences, 3225 Daniel Avenue, Dallas, TX, 75205
[15]Silixa Ltd, 3102 Broadway St., Suite E, Missoula, MT, 59808, USA
[16]Idaho National Laboratory, Nuclear Nonproliferation Division, PO Box 1625, MS2212, Idaho Falls, ID, 83415, USA
[17]RedVox, Inc., 73970 Makako Bay Drive 116, Kailua-Kona, HI, 96740
[18]Florida Institute of Technology, Geospace Physics Laboratory, 150 W. University Blvd., Melbourne, FL, 32901, USA
[19]AWE Blacknest, Brimpton Common, Reading, Berkshire, RG7 4RS, UK
[20]United States Department of Defense, KBR Consultant, Las Cruces, NM, USA

[21]University of Texas-El Paso, Earth, Environmental, and Resource Sciences, 500 W University, El Paso, TX, 79902, USA
[22]NASA Langley Research Center, SCIFLI, Hampton, Virginia, 23681, USA
[23]Air Force Research Laboratory, Sensing Effects & Analysis, 2241 Avionics Circle, Wright-Patterson AFB, Ohio, 45433, USA
[24]Sandia National Laboratories, Atmospheric Science, Albuquerque, NM, 87123, USA
[25]Defense Threat Reduction Agency (DTRA), 8725 John J. Kingman Rd, Stop 6201, Ft. Belvoir, VA, 22060, USA
[26]Colorado State University, Department of Geosciences, 1482 Campus Delivery, Ft. Collins, CO, 80523, USA
[27]Independent Researcher, Bowie, MD, 20715, USA
[28]University of Maryland, Dept. of Geology, College Park, MD, 20742, USA
[29]Nevada National Security Sites, Science and Technology, 2621 Losee Rd, North Las Vegas, NV, 89030, USA

[*]Corresponding Author e-mail: esilbe@sandia.gov

Abstract

Sample Return Capsules (SRCs) entering Earth's atmosphere at hypervelocity from interplanetary space are a valuable resource for studying meteor phenomena. The 24 September 2023 arrival of the OSIRIS-REx (Origins, Spectral Interpretation, Resource Identification, and Security-Regolith Explorer) SRC provided an unprecedented chance for geophysical observations of a well-characterized source with known parameters, including timing and trajectory. A collaborative effort involving researchers from 16 institutions executed a carefully planned geophysical observational campaign at strategically chosen locations, deploying over 400 ground-based sensors encompassing infrasound, seismic, distributed acoustic sensing (DAS), and GPS technologies. Additionally, balloons equipped with infrasound sensors were launched to capture signals at higher altitudes. This campaign (the largest of its kind so far) yielded a wealth of invaluable data anticipated to fuel scientific inquiry for years to come. The success of the observational campaign is evidenced by the near-universal detection of signals across instruments, both proximal and distal. This paper presents a comprehensive overview of the collective scientific effort, field deployment, and preliminary findings. The early findings have the potential to inform future space missions and terrestrial campaigns, contributing to our understanding of meteoroid interactions with planetary atmospheres. Furthermore, the dataset collected during this campaign will improve entry and propagation models as well as augment the study of atmospheric dynamics and shock phenomena generated by meteoroids and similar sources.

1. Introduction

Geophysical sensing of objects entering planetary atmospheres and surfaces is of immense importance for understanding impact-induced physical processes on Earth and beyond. Interplanetary space is teeming with meteoroids, asteroids, and comets (e.g., Belton, 2004; Chapman, 2008), and is sometimes even visited by objects originating from beyond our solar system, such as 1I/'Oumuamua (Meech et al., 2017). While the rate of large, extremely energetic and planet altering impacts has largely dissipated over time since the Late Heavy Bombardment, smaller impacts continue to happen on Earth and elsewhere. For example, the lunar surface is frequently impacted by objects large enough to produce light emissions visible from Earth (e.g., Avdellidou and Vaubaillon, 2019; Ortiz et al., 2006; Ortiz et al., 2015). Moreover, bright flashes seen in the atmosphere of Venus have been attributed to meteoroids (Blaske et al., 2023). On Mars, a freshly formed impact craters have been found (Daubar et al., 2023; Posiolova et al., 2022), and possible seismic and acoustic wave signatures from meteoroid entries were detected by NASA's InSight lander (Garcia et al., 2022).

Unfortunately, it is profoundly difficult to predict impacts of meter-sized and larger objects with sufficient temporal and spatial accuracy and with long enough advance notice to allow comprehensive observational campaign planning. Thus, it is nearly impossible and prohibitively costly to mount a comprehensive observational campaign using a full range of sensing modalities. Therefore, virtually all observations are incidental – instruments either passively "wait" for an event to happen over a certain region (e.g., Devillepoix et al., 2020) or they make a detection as a byproduct of a completely different observational mission (e.g., Jenniskens et al., 2018). While small meteoroids are numerous, objects in a meter-size range are significantly more scarce and thus profoundly more difficult to capture with a multitude of instruments. Even if detailed observations take place, source characterization does not come without its own challenges. Impeding factors include incomplete ground truth, inability to directly measure and sample the object, lack of comparable events (no two natural objects are alike), limitations in models and theoretical considerations, and other uncertainties (Silber, 2024).

Therefore, it is imperative to make use of well-characterized artificial objects that can serve as natural meteoroid/asteroid analogues (e.g., ReVelle et al., 2005). Ideal candidates are space mission sample return capsules (SRCs) that re-enter from interplanetary space and thus achieve speeds that match those of (slow) natural meteors (> 11 km/s). Their speed is also relatively close to the mean speed of natural asteroid entries (25 – 30 km/s) (Janches et al., 2006). Only five sample return missions have re-entered from interplanetary space since the end of the Apollo era:

4

Genesis (ReVelle et al., 2005), Stardust (ReVelle and Edwards, 2006), Hayabusa 1 (Ishihara et al., 2012), Hayabusa 2 (Sansom et al., 2022), and OSIRIS-REx (Origins, Spectral Interpretation, Resource Identification, and Security-Regolith Explorer) (Fernando et al., 2024; Silber et al., 2023a). All five were detected by dedicated geophysical instruments (infrasound or/and seismic) (see Silber et al., 2023a for details).

To understand the relevance and application of artificial objects, such as SRCs, towards the study of larger meteoroid dynamics in the planetary atmospheres, we start with a brief overview of meteor phenomena.

Approximately 10^5 tons per year of extraterrestrial material enter the Earth's atmosphere, ranging in size from dust particles to meters (Plane, 2012). Most particles peak in diameters around 2 x 10^{-4} m (Kalashnikova et al., 2000; Plane, 2012), with only an extremely small fraction corresponding to meter-sized and larger objects (Drolshagen et al., 2017; Moorhead et al., 2017). Typical entry speeds are 11.2 – 72.8 km/s for objects originating in the Solar System (Ceplecha et al., 1998). Speeds greater than ~73 km/s correspond to objects visiting from interstellar space, although some exceptions around that velocity have been noted (Peña-Asensio et al., 2024). Asteroids (≥1m in diameter) and meteoroids (<1 m in diameter), through their collisions with local atmosphere and subsequent ablation, produce a light phenomenon known as a meteor or a shooting star (Ceplecha et al., 1998). Very bright meteors are known as fireballs (brighter than Venus, magnitude -4) and bolides (brighter than magnitude -14 (Belton, 2004)), and exceptionally bright events (exceeding magnitude -20) as superbolides (Ceplecha et al., 1998).

Of particular interest to the scientific and planetary defense communities are the asteroids and a subset of sufficiently large and fast meteoroids that produce shock waves upon entering the upper regions of the atmosphere (Bronshten, 1983; Ceplecha et al., 1998; Silber et al., 2018; Tsikulin, 1970). Specifically, the shock waves can lead to formation of secondary physical phenomena, from low frequency acoustic waves and seismic shaking (e.g., Arrowsmith et al., 2008a; Arrowsmith et al., 2007; Caudron et al., 2016; Ceplecha et al., 1998; Evers and Haak, 2003; Ishihara, 2004; Pilger et al., 2020; ReVelle, 1974; Silber and Brown, 2019) to ionospheric disturbances (e.g., Luo et al., 2020; Perevalova et al., 2015; Yang et al., 2014). When recorded by geophysical instruments, the signatures of these phenomena can be analyzed to infer physical properties and characteristics of the emitting source (e.g., ReVelle, 1976). Smaller meteoroids with diameters 0.1 – 10 cm, while still capable of generating shock waves, are not of interest in this study as in most cases these completely ablate at altitudes between ~70 and 100 km (Ceplecha et al., 1998; Silber and Brown, 2014).

5

Large objects can penetrate deep into the atmosphere, depositing a tremendous amount of energy at mid and low altitudes (typically below 50 km) and sometimes, their fragments may reach the surface as meteorites. A recent example is the Chelyabinsk superbolide, whose arrival caught the scientific community by surprise. The Chelyabinsk impactor was ~18 m in diameter and it deposited energy of approximately 500 kt of TNT equivalent (1 TNT = 1.484 x 10^{12} J), leaving a wake of destruction beneath its path (Brown et al., 2013; Popova et al., 2013).

SRCs can serve as reasonable analogues for meter-sized objects that are generally studied using a variety of sensing modalities, from ground-based (e.g., optical (e.g., Devillepoix et al., 2020), radar (e.g., Janches et al., 2006), infrasound (e.g., Silber and Brown, 2014), seismic (e.g., Edwards et al., 2008)) to space-based instruments (e.g., US government sensors (e.g., Brown et al., 2002), Geostationary Lightning Mapper (GLM) (e.g., Jenniskens et al., 2018)). In this paper, we place an emphasis on geophysical observations that include infrasound (ground-based and airborne), acoustic (audible), seismic, Distributed Acoustic Sensing (DAS), and Global Positioning System (GPS). We will outline the function of these in Section 2.

We present multi-modal observations of the OSIRIS-REx re-entry, the largest geophysical observational campaign of a controlled re-entry ever conducted. Multi-modal, large scale observational campaigns of re-entry and similar phenomena with well-known ground truth require careful planning, coordination, and execution. There is also only one chance to get it right – the object's re-entry cannot be delayed or modified to meet the observation campaign's needs. Given that this was an enormous undertaking that involved many scientists from over a dozen institutions, we felt that it was pertinent to consolidate our efforts into a single publication that will provide a complete contextual picture of the campaign and serve as a scientific reference for data types and sources, study replication, and for building upon this work by others. Furthermore, campaigns like this one provide an unparalleled learning opportunity for future "one shot" terrestrial and space exploration missions.

This paper is organized as follows: in Section 2, we give a brief background on geophysical sensing modalities, and in Section 3 we outline a primer on meteor generated shock waves and how they can be detected by geophysical instruments. The OSIRIS-REx re-entry is presented in Section 4. In Section 5 we describe the institutional involvement and the geographical context, and in Section 6, the field deployment effort and various instruments used. In Section 7, we present the preliminary results, and in Section 8 we outline our conclusions and path forward.

2. A Brief Primer on Geophysical Sensing Modalities

Infrasound is defined as sound waves below the limit of human hearing (<20 Hz). Infrasound sensing finds widespread utility in monitoring natural phenomena such as volcanic eruptions (e.g., Matoza et al., 2019), earthquakes (e.g., Arrowsmith et al., 2011) and meteorological events (Stopa et al., 2012). Additionally, it serves as a critical tool for detecting and characterizing anthropogenic activities, including explosions (e.g., Arrowsmith et al., 2008b; Mutschlecner and Whitaker, 2006; Obenberger et al., 2022) and rockets (e.g., Balachandran and Donn, 1971; Pilger et al., 2021). Infrasound monitoring also supports efforts in nuclear test ban verification (Brachet et al., 2010). The most typical instruments include ground-based sensors. These can be permanent or temporary installations. The latter are useful for short-term observational campaigns. In recent years, there has been an emergence of balloon-borne infrasound sensing (Bowman and Albert, 2018; Silber et al., 2023b) which has opened new avenues for detection and characterization of ground and elevated infrasound sources, and for validation of theoretical predictions (Albert et al., 2023). Balloon-borne infrasound has been proposed as a feasible mode of exploration for planets with thick atmospheres where other sensing modalities are either not possible or are exceedingly more costly (Krishnamoorthy and Bowman, 2023). Balloons also offer a unique vantage point, away from heavy tropospheric noise, and in a presumably quieter region of the atmosphere (Krishnamoorthy et al., 2020). There have been successful detections of high-altitude and ground-based phenomena on balloons, including rocket launches, atmospheric explosions, chemical explosions, storms, and gravity waves (Albert et al., 2023; Bowman and Lees, 2018). While bolide detection by a balloon-borne infrasound sensor has never been confirmed, it is expected that these platforms would readily detect a bolide should one occur in the vicinity.

Much of seismic analysis involves observing and modeling the wavefields generated from sources interior to or on the surface of the Earth. Earthquakes, volcanic disturbances, chemical and nuclear explosions, and artificial energy sources such as vibration-producing trucks or even hand-held hammer blows can provide seismic wavefields that can be modeled to determine the physical characteristics of the Earth over scales from meters to 10,000 km. Impulsive atmospheric sources such as explosions (e.g., Matoza et al., 2022), bolide sonic booms (D'Auria et al., 2006; Langston, 2004; Le Pichon, 2002), or even thunder (Lin and Langston, 2009a; Lin and Langston, 2009b), can be interesting in their own right as well as providing for new wavefields for investigating Earth structure using records from seismometers.

Distributed Acoustic Sensing (DAS) systems are a rapidly emerging technology that provide spatially dense (~1–10 m), extensive (10s of km), and high-fidelity seismic measurements by sensing with fiber-optic cables (e.g., Hartog, 2017). Previous studies have demonstrated that DAS can capture a variety of seismo-acoustic signals including seismic waves from earthquakes and explosions (e.g., Fang et al., 2020; Lindsey et al., 2017), and meteorites (Vera Rodriguez et al., 2023). While seismometers and infrasound sensors have been employed to measure signals from spacecraft re-entry events prior to the OSIRIS-REx sample return capsule (e.g., Edwards et al., 2007; ReVelle and Edwards, 2006), the OSIRIS-REx event is the first instance of DAS deployment to record a re-entry. Similarly, while DAS has not yet been deployed in extraterrestrial settings, data returned from seismometers and/or infrasound sensors have provided information about the seismic activity and structure of the Moon and Mars (e.g., Giardini et al., 2020; Lognonné et al., 2020; Nunn et al., 2020) and the atmosphere of Mars (e.g., Banfield et al., 2020; Ortiz et al., 2022).

Energetic and explosive events near the Earth are well-known to produce acoustic (compression) waves that propagate upward and outward into the atmosphere. When these acoustic waves propagate upward into the ionosphere, they couple with ionospheric plasma, producing electron density fluctuations (Forbes and Roble, 1990; Miller et al., 1986). Wave periods generated by these events range from 2-16 minutes, with ground-level speeds between 300-400 m/s. Speeds dramatically increase with altitude above the mesosphere due to changes in density and increases in background thermosphere temperatures. At altitudes near peak electron density (250-400 km), speeds can range from 700-900 m/s. In all, it takes approximately 8 to 10 minutes for the wave generated at the Earth's surface to propagate to these altitudes.

These waves create electron density perturbation signals that are probed remotely, such as using electromagnetic instruments. Impulsive events like meteors (e.g., Luo et al., 2020; Perevalova et al., 2015; Yang et al., 2014), volcanic eruptions (e.g., Shimada et al., 1990), earthquakes (e.g., Otsuka et al., 2006), tsunamis (e.g., Blewitt et al., 2009), rocket launches (e.g., Afraimovich et al., 2001), and ground explosions (e.g., Fitzgerald, 1997) have been examined using these methods. Here, we are interested in examining the effects of the shock wave generated by the hypersonic OSIRIS-REx SRC re-entry, and how it might affect the ionosphere and signals used to probe it. We employ GPS L-band signals which are frequently used to probe the ionosphere, but signatures often suffer a 1 to 30 minute delay before they impact the ionosphere and can be detected.

3. Meteor Generated Shock Waves

8

In this section, we offer a concise overview of meteor-generated shock waves and their correlation with acoustic and, on occasion, seismic waves (e.g., Edwards et al., 2008; Silber and Brown, 2019). We also briefly outline the similarities between shock waves generated by natural objects and their artificial analogues (Figure 1).

In principle, the mechanisms governing meteor-generated shock waves are broadly relevant to artificial hypersonic analogues (and vice versa), including space mission re-entries, rendering them valuable proxies for investigating meteor phenomena (ReVelle et al., 2005; Silber et al., 2023a).

When a meteoroid (or an asteroid) reaches the continuum flow regime as it descends through the Earth's exponentially denser atmosphere at hypervelocity, it generates a shock wave (Krehl, 2011; Silber et al., 2018 and references therein). Meteoroids travel at extremely high Mach numbers, from 35 to 240. Mach number (M) is the ratio of the meteoroid speed and the local speed of sound. At such speeds, the Mach cone angle (outlining the adiabatically expanding ablational flowfield) is small enough that the shock front can be approximated as a cylinder, therefore forming the so-called cylindrical line source (Plooster, 1970; ReVelle, 1976). The shock travels ballistically, or perpendicularly to the meteoroid flight trajectory, and energy is deposited into the surrounding atmosphere as a function of path length. It is important to note that the fundamental difference in shock waves between the large meteoroids/asteroids and artificial analogues is the fact that the shock waves generated by natural objects are ablationally amplified, while objects such as SRCs have a very limited ablation rate. Another key difference is the significantly higher magnitude and intensity of the hyperthermally driven chemical reactions in the ablationally amplified meteor/asteroid flowfield, which ultimately affects the strength of a shock wave. Moreover, meteoroids and asteroids frequently experience fragmentation, which can occur in the form of continuous fragmentation, gross fragmentation, or some combination of the two (e.g., Silber, 2024; Trigo-Rodríguez et al., 2021). In such cases, the shock wave is no longer generated by the object's hypersonic passage alone, but it also includes the shock with quasi-spherical or spherical geometry (also known as point source). The SRCs do not include such a point source component allowing the hypersonic shock wave to be studied without interference from such signals.

The blast radius (R_0) represents the volume of a region containing superheated adiabatically expanding plasma in the flow-field immediately behind the shock front, where highly non-linear processes take place. The mathematical expression is: $R_0 = (E_0/p_0)^{0.5}$, where E_0 is the energy per unit length and p_0 is the ambient pressure. Assuming no fragmentation, the blast radius can be

approximated as $R_0 \sim Md_m$. where M is the Mach number and d_m is the meteoroid diameter. It is generally accepted that beyond approximately $10R_0$, the shock decays to a weak shock regime, and at some point, to a linear acoustic wave (Plooster, 1970; ReVelle, 1976; Tsikulin, 1970). A comprehensive review of meteor generated shock waves can be found in Silber et al. (2018), and a review on meteor-generated infrasound in Silber and Brown (2019).

Shock waves generated by hypersonic passage of meteoroids (and other impulsive sources) ultimately decay to infrasound, which has the remarkable ability to propagate over vast distances with minimal attenuation (Evans et al., 1972). At a very close range from the source, the acoustic wave might have both inaudible and audible components. A familiar example of the audible component would be a sonic boom generated by a jet when it breaks the sound barrier. The 1908 Tunguska airburst was the first documented bolide-generated infrasound (Whipple, 1930), followed by a dozen or so events during the 1960s and the 1970s (Revelle, 1997; Silber et al., 2009). Since the inception of the Comprehensive Nuclear-Test-Ban Treaty (CTBT) in the mid-1990s (Brachet et al., 2010), infrasound has gained momentum as a vital sensing modality used towards global detection of large bolides (e.g., Pilger et al., 2015; Pilger et al., 2020).

In some instances, infrasound might have enough energy to induce seismic waves, known as air-coupled or atmospheric seismic waves, which can be detected by seismometers and other seismic monitoring instruments (Edwards et al., 2008). The characteristics of these seismic waves, such as their amplitude, frequency, and arrival time, can provide valuable information about the source. It's important to note that while bolide sonic booms can induce seismic waves, the seismic signals produced are typically much weaker and shorter-lived compared to those generated by earthquakes or other large-scale seismic events (e.g., impacts). There are three modes of coupling: (1) direct coupling (the incident acoustic wave induces ground motion); (2) precursory (generated by the infrasound wave impacting the ground at specific incidence angles that allow resonant coupling to subsurface seismic propagation modes that then travel independently to the recording station); and (3) impact (surface and body waves generated when a fragment of a meteoroid hits the surface) (see Cumming, 1989; Edwards et al., 2008).
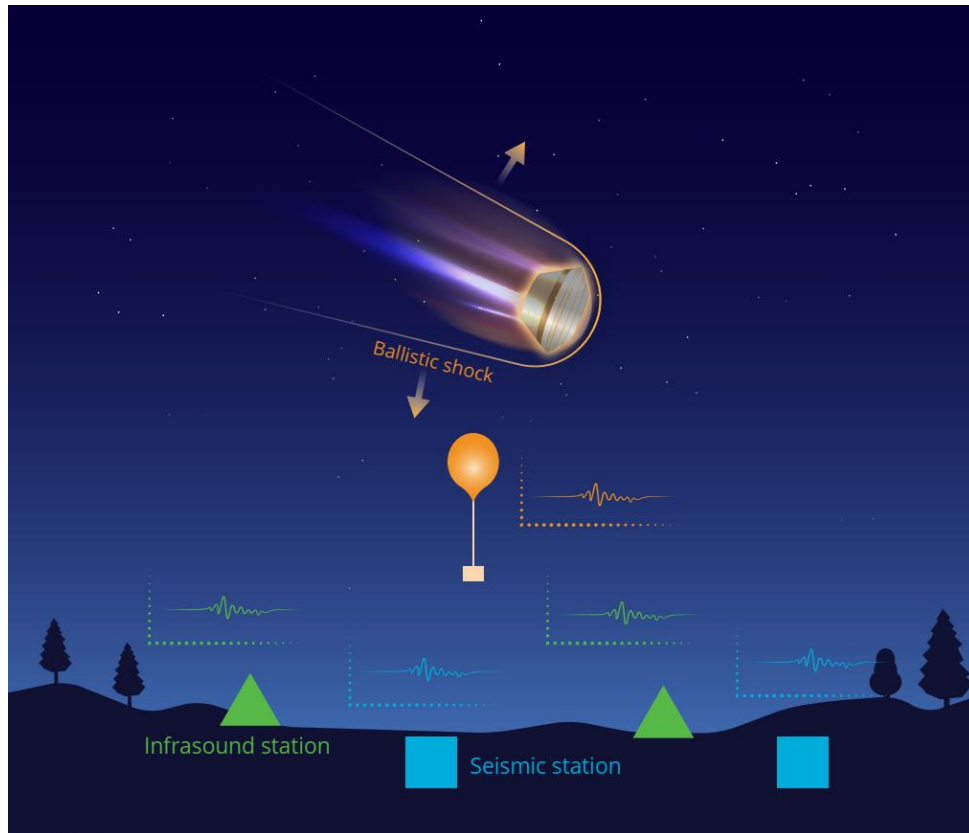
Figure 1: Diagram showing the shock wave generated by a sample return capsule (analogue to meteoroids) as it travels through the atmosphere. Ground-based infrasound and seismic instruments and airborne infrasound instruments could detect the shock waves depending on circumstances. Diagram not to scale. Diagram does not include all possible sensing modalities that might be used in geophysical observations of re-entry.

4. OSIRIS-REx and Geophysical Observation Considerations

Controlled and well-characterized re-entries from interplanetary space at velocities exceeding 11 km/s are exceptionally rare. Only five such re-entries took place since the end of the Apollo era, with the most recent one being OSIRIS-REx in September 2023 (Silber et al., 2023a). Prior to that, Genesis landed in 2004 (ReVelle et al., 2005), Stardust in 2008 (ReVelle and Edwards, 2006), Hayabusa 1 in 2010 (Fujita et al., 2011; Watanabe et al., 2011; Yamamoto et al., 2011), and Hayabusa 2 in 2020 (Nishikawa et al., 2022; Sansom et al., 2022; Sarli and Tsuda, 2017; Yamada and Yoshihara, 2022). The physical parameters for the five SRCs are listed in Silber et al. (2023a). Both Genesis and Stardust landed in the USA, and their signals were detected by instruments installed at West Wendover, UT airport (ReVelle et al., 2005; ReVelle and Edwards, 2006). Genesis was detected via infrasound, and the acoustic signatures generated by the latter three were recorded by both infrasound and seismic instruments. A review describing seismo-

acoustic detections of these four re-entries is given by Silber et al. (2023a), and we therefore keep the discussion to a minimum.

The OSIRIS-REx space mission was designed to collect samples of the near-Earth asteroid Bennu and bring those particles to Earth for analysis (Ajluni et al., 2015; Beshore et al., 2015; Lauretta et al., 2017). This was the first asteroid sample collection mission for the USA. On September 24, 2023, the SRC separated from the main craft and entered the atmosphere at a very shallow angle (nearly horizontal). The SRC is 81 cm wide and has a mass of ~46 kg. The atmospheric interface was at an altitude of 125 km above a point close to San Francisco, CA (14:42 UTC, 8:42 MDT). After a few minutes flight, it safely touched down on the Department of Defense's Utah Test and Training Range (UTTR) at a speed of 5 m/s (18 km/h), slightly faster than originally anticipated (Gran, 2023). The re-entry consisted of several flight phases, including hypersonic, transonic, and dark flight (see Silber et al., 2023a for further details). The drogue parachute was supposed to open at an altitude of ~30.4 km to slow down and stabilize the SRC before the main parachute sequence but it failed due to faulty wiring (Francis et al., 2024). When the main parachute opened at 2.74 km altitude, the drogue was also released but because it was already cut loose, it flew off. The main parachute managed to sufficiently slow the SRC down, facilitating soft landing at 14:52 UTC, a minute earlier than planned (Francis et al., 2024; Gran, 2023).

The SRC return of the OSIRIS-REx mission offered a rare opportunity to record both the incident atmospheric pressure field of the incoming Mach cone at the ground surface and induced seismic motions near the Earth's surface at a known location in time and space. Factors that are important in deducing the effects of the acoustic-seismic interaction at the ground surface include obtaining basic knowledge about the incident wavefield such as its horizontal slowness and azimuth of approach (Lin and Langston, 2009a). It is testament to the accuracy of NASA orbital dynamics that the trajectory and arrival time of the returning capsule could be controlled for a landing in western Utah. However, the exact behavior of the expanding Mach cone and how it interacts with a particular place on the ground depends not only on the precise path geometry but atmospheric winds that can cause lateral variations in sound speed distorting the acoustic wavefront on its descent from the upper atmosphere. In principle, the horizontal phase velocity of the downgoing acoustic wave could vary from infinite velocity (vertical incidence) to approximately 0.33 km/s for near-horizontal wave propagation. Conversion of the atmospheric acoustic wave into propagating P and S body waves or Rayleigh waves will strongly depend on the local wave slowness. Directional attributes, such as particle motion, will also depend on wave azimuth of approach.

The nominal trajectory, based on the entry, descent, and landing (EDL) simulations (Francis et al., 2024) was provided by NASA (M. Moreau, personal communication); the ground track is shown in Figure 2. The color represents the altitude. The peak heating, dynamic pressure, and Mach number as a function of altitude are also shown in Figure 2. We note that any trajectory-related values (geographical coordinates, altitudes, peak heating, dynamic pressure, and Mach number) presented here correspond to the nominal trajectory (Francis et al., 2024) that was released by NASA before the OSIRIS-REx re-entry, and it therefore may not accurately represent the real-time re-entry trajectory. However, it is expected that the two would be in a very close agreement.
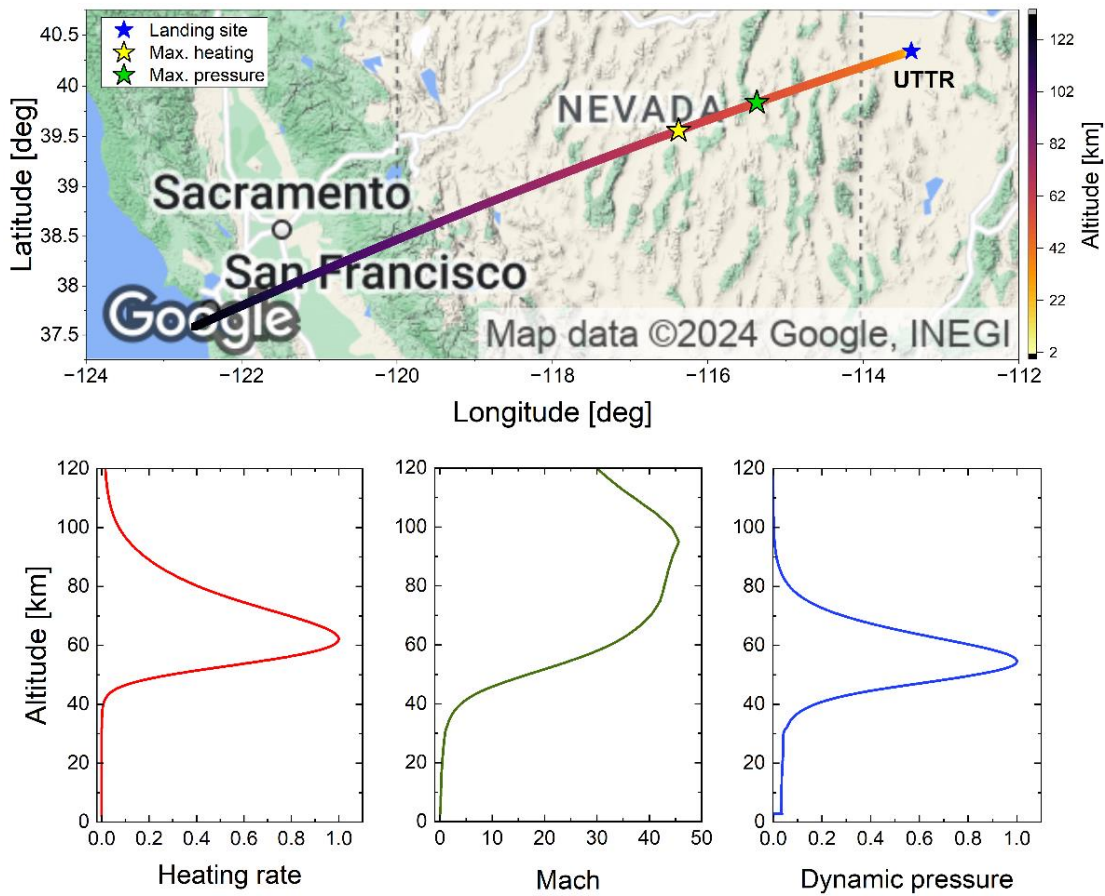

Figure 2: (Top panel) OSIRIS-REx ground track. Yellow and green stars show the points of maximum heating and maximum dynamic pressure, respectively. The landing site is indicated with a blue star. (Bottom panels) The normalized heating rate, Mach number, and normalized dynamic pressure as a function of altitude are shown in the three panels below the map. Trajectory data are courtesy of NASA.

One significant distinction between re-entry phenomena and conventional controlled experiments, such as static sources (e.g., chemical explosions) or sources with constrained lateral movement

at mid- and low altitudes (e.g., rocket launches), is the extensive geographical area (Figure 2) covered and the multitude of potential observation points available to capture the dynamic changes occurring along the trajectory. Consequently, selecting the most relevant regions of interest becomes pivotal to ensure the acquisition of high-fidelity data. Although permanent infrasound and seismic stations are established throughout the USA, the immediate vicinity beneath and adjacent to the trajectory lacks sufficient geophysical instrumentation to reliably capture signals with a high degree of certainty. While incidental detections remain plausible, there exists uncertainty regarding the likelihood of signal recording. This uncertainty stems from the fact that the altitude of the SRC could be too elevated or the SRC ground track would be at a considerable distance from the existing permanent instrument installations. Given the infrequency of re-entry events from interplanetary space, relying solely on distant instruments to gather data entails substantial risk. Therefore, systematic planning of a dedicated observational campaign is imperative.

Our geophysical observational campaign was carefully planned to maximize the scientific output and ensure the highest chance of success while considering various intrinsic and extrinsic factors. These include, but are not limited, to the following:

i.   Signal detection and data collection locations (e.g., identify locations through research and analysis where signals related to the re-entry are most likely to be detected; consider factors such as geological features, topography, and historical data on similar events to pinpoint optimal observation sites and prioritize locations that are accessible for instrumentation setup and maintenance; evaluate the potential for multiple observation points to capture different aspects of the re-entry and enhance data coverage).

ii. Cost considerations (e.g., develop a budget that accounts for all expenses associated with the campaign, including personnel salaries, fieldwork costs, equipment procurement and maintenance, logistics, and administrative expenses; allocate resources strategically to ensure the campaign's financial viability and explore cost-saving measures such as optimizing logistical arrangements to minimize expenses without compromising scientific objectives).

iii. Instrument synergy and deployment (e.g., assess the compatibility and capabilities of different instrumentation options to ensure they complement each other and provide comprehensive data coverage; consider factors such as instrument reliability, data transmission capabilities, and power requirements when selecting deployment locations and configurations; implement contingency plans and redundancy measures to mitigate

the risk of instrument failure and ensure continuous data collection throughout the campaign).

iv. Environmental and infrastructure impact (e.g., conduct environmental risk assessments to identify potential safety hazards associated with fieldwork activities, such as exposure to extreme temperatures, rough terrain, or wildlife encounters; engage with relevant stakeholders, regulatory bodies, and environmental agencies to obtain permits and approvals for fieldwork activities; implement mitigation measures to minimize environmental disruption, such as site restoration efforts and adherence to best practices for minimizing habitat disturbance; coordinate with landowners, facility managers, and infrastructure operators to ensure minimal interference with existing infrastructure and facilities).

v. Personnel allocation (e.g., define roles and responsibilities for scientific and technical staff, students, and collaborators involved in the campaign and provide specialized training to personnel on wilderness safety, navigation techniques, and emergency first aid to enhance their ability to respond to safety incidents in remote locations; foster a collaborative and inclusive work environment that encourages communication, teamwork, and knowledge sharing among team members; prioritize the inclusion of personnel with a cardiopulmonary resuscitation (CPR) certification and wilderness knowledge in field teams to oversee safety protocols and emergency response procedures; establish clear lines of communication and designated safety officers within field teams to facilitate coordination and decision-making in emergency situations).

vi. Timeline and coordination (e.g., schedule safety briefings and training sessions to reinforce safety protocols and address any emerging safety concerns; establish communication protocols for reporting safety incidents or concerns, including designated channels for contacting emergency services and obtaining assistance; incorporate safety checkpoints into the campaign timeline to review safety procedures, assess risks, and adjust plans as necessary to ensure the ongoing safety of all personnel involved).

With respect to the most optimal observational point, the region beneath the peak heating point would be of primary interest since the energy deposition would be the greatest, and the signals the strongest. The peak heating was projected to take place over Eureka, NV, a small town along US Route 50, known as "the loneliest road in America". Therefore, this region was deemed to be ideal for emplacement of geophysical instruments to best capture the signals from OSIRIS-REx.

At the coordinates corresponding to the peak heating (39.5585 N, -116.3852 E, altitude 62.1 km), the dynamic pressure was predicted to be 69% of the maximum. The SRC was estimated to be travelling at Mach 34.8. At this speed the Mach cone angle is only 1.65 degrees. Thus, for the purposes of modeling and signal prediction, the shock can be approximated as a cylindrical line source (Figure 1), travelling ballistically relative to the path of the object (Silber & Brown 2019; ReVelle 1976). Consequently, emplacing some number of instruments roughly perpendicular to the trajectory would theoretically capture the shock decay as a function of distance. Moreover, emplacing instruments in several locations beneath and roughly parallel to the trajectory, would theoretically capture signals generated at different parts of the trail and aid in studying the signal characteristics as a function of altitude and other factors (e.g., velocity, atmospheric specifications).

Another region of scientific interest from the observational standpoint would be the trajectory segment related to the SRC deceleration and the flight regime change from hypersonic to supersonic and finally subsonic. The lower altitude of the SRC would ideally provide ample opportunity for the signals to be detected by geophysical instruments. The maximum dynamic pressure was predicted to occur at an altitude of 54.5 km (39.8365 N, -115.3717 E). Here, the heating would have decreased to 66% of the maximum. In the case of OSIRIS-REx, this is just beyond the Nevada-Utah state line. For reference, the West Wendover, UT airport is due north.

The highest Mach achieved by the SRC was 45.6, at 95 km altitude (38.5178 N, -119.8486 E). Here, the heating rate was estimated at only 11% of the maximum achieved and dynamic pressure at ~0.5% of the maximum. Based on the available parameters, the onset of the shock wave is estimated to occur at an altitude of approximately ~80 km (or slightly higher). The shock wave, as soon as it forms, would also produce infrasound. It would be scientifically interesting to attempt to capture the shock wave as it forms at these altitudes. However, considering that the SRC is at a high altitude and the energy deposition is much lower than at the peak heating point, such an endeavor would carry a high risk of non-detection. Therefore, our observational campaign focused on the geographic region spanning from slightly west of Eureka, NV (roughly the peak heating point) towards east, in the area relatively close to the landing site (Figure 2).

5. Institutional Engagement and Site Selections

5.1 Institutional Engagement

Approximately 80 investigators from over a dozen institutions participated in this historical observational campaign. The primary participating institutions were: Sandia National Laboratories (SNL), Los Alamos National Laboratory (LANL), NASA Jet Propulsion Laboratory (JPL), Air Force Research Laboratory (AFRL), Atomic Weapons Establishment (AWE) Blacknest, Boise State University (BSU), Defense Threat Reduction Agency (DTRA), Idaho National Laboratory (INL), Johns Hopkins University (JHU), Kochi University of Technology (KUT), Nevada National Security Site (NNSS), Oklahoma State University (OSU), Southern Methodist University (SMU), TDA Research Inc. (TDA), University of Hawaii (UH), and University of Memphis (UM). For brevity, affiliations of those who were involved and/or contributed through primary institutions (e.g., student exchange, internships, second-level collaboration, and similar means) are stated at the front of the paper but not reiterated here.

To keep focus on the scientific aspect of the campaign, the main text might not always differentiate who did what unless contextually necessary. While each team had their own scientific objectives, the entire multi-institutional group collaborated towards the common goal of gathering high-fidelity data. In the remainder of this section, we first describe the geographical context, followed by ground-based observations, and conclude with balloon-borne observations. We also include the appendices and supplemental materials (SM) with additional pertinent information, which we will refer to throughout the main text.

5.2 Geographical Context

5.2.1 West Region: Eureka, NV

Two primary locations were selected as deployment sites in the region of Eureka, NV: Eureka Municipal Airport (EUE) (39.6039 N, -116.0036 E) and the Newark Valley (centered at 39.6833 N, -115.7217 E). EUE was selected because it was situated almost directly beneath the OSIRIS-REx re-entry path, was access controlled, and had large areas of pavement for equipment layout. Moreover, for balloon deployment, trajectory calculations using weather model outputs from previous years indicated that the balloons would most likely remain close to the re-entry path if launched from the EUE. Finally, there were very few other suitable sites in the area for multiple balloon releases. The town of Eureka graciously allowed us to use the airport. The Newark Valley was selected because it is traversed by Strawberry Road, which is not traffic heavy, passes through large plots of land owned by the Bureau of Land Management (BLM), and most

importantly, runs north to south with a section situated directly beneath the nominal re-entry trajectory. This is ideal for configuring a transect with instrument installations perpendicular to the nominal trajectory. Permits or confirmation of casual use compliance were obtained from BLM to install infrasound and seismic sensors, as well as DAS. Bean Flat Rest Area (BFRA) was an additional location (39.4996 N, -116.5095 E), further west and very close to the point of peak heating, that was selected for seismic instrument installations. The list of institutions that deployed in the West Region is shown in Table 1. The map is shown in Figure 3.

5.2.2 East Region: Utah-Nevada

The East Region included several locations, chosen because of their proximity to the nominal re-entry trajectory and the ease of access. These included the NV-UT state line, West Wendover Airport (ENV) in Utah, and two locations east of the UTTR. The area around the NV-UT state line (centered around 40.201 N, -114.047 E), was selected because of accessibility and the Bureau of Land Management (BLM) landownership. Importantly, on the Utah side just beyond the NV-UT state line (centered around 40.1738 N, -113.9960 E), there is a local road (N Ibapah Road) that runs approximately north-south beneath the nominal re-entry trajectory. On the Nevada side, US Route 93 runs from the nominal trajectory and north up to ENV (the half-way point is approximately at 40.4773 N, -114.1555 E). ENV (40.7280 N, -114.0212 E) was previously utilized in observing the re-entry of Genesis and Stardust, although their nominal trajectories were significantly closer than that of OSIRIS-REx. Preliminary propagation modeling and hypersonic carpet prediction modeling using averaged atmospheric specifications and winds from previous years showed that signals generated by the OSIRIS-REx SRC would be received at ENV. The airport offered a secure large space that would allow sensor setup without any tampering. Two other locations east of the UTTR were selected, one north of Dugway, UT (40.2571 N, -112.7404 E), and the other one was in Clive, UT (40.7089 N, -113.1167 E). Dugway is ~63 km east, and Clive is ~52 km northeast from the nominal landing site. See Table 1 for institutions that deployed in the East Region. The map is shown in Figure 3.

5.2.3 Distal Region

Distal Region stations consisted of permanent infrasound array stations, which were part of larger networks and wider trial series, as well as dedicated stations that were installed for the purpose of detecting the OSIRIS-REx SRC re-entry. These stations were situated in several areas east (Price, UT), north (Boise, ID) and south (St. George, UT and NNSS, NV) relative to the SRC's nominal trajectory, and at distances ranging from ~250 to ~400 km. The list of institutions that operated these infrasound assets is shown in Table 1.
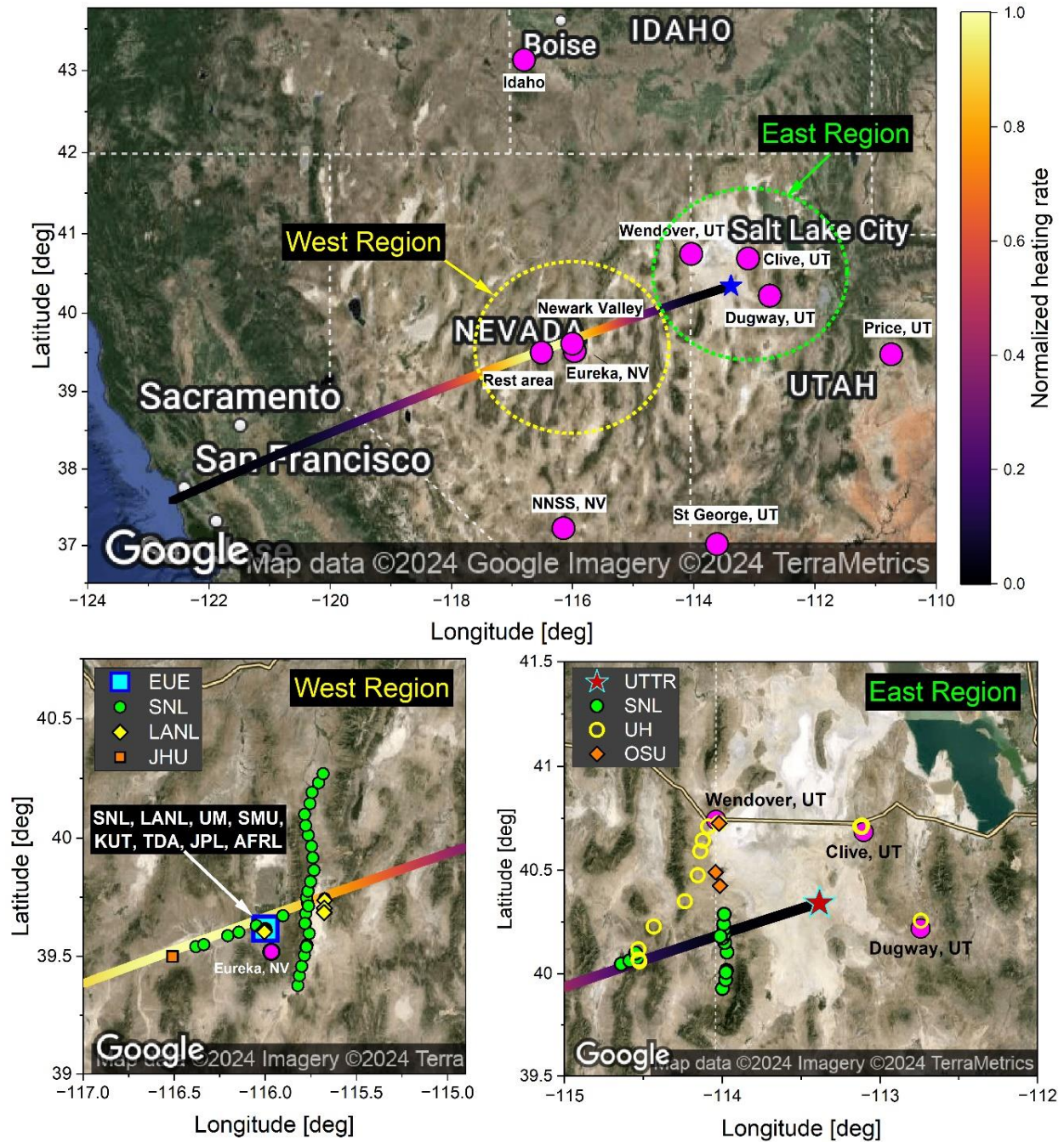
Figure 3: Maps showing deployment regions (top panel). Areas beyond the circled areas are within the Distal Region. Bottom left: Zoomed in West Region. Bottom right: Zoomed in East Region. Pink circles are various landmarks (to be explained further in the text). In the West Region, most institutions deployed at EUE. Installations beyond the airport are plotted separately by institutions for the West and East Regions. Instrument type is further enumerated Appendices B and C.

Table 1: List of institutions that deployed instruments in the various regions.

West Region			East Region		Distal Region
Eureka Airport	**Newark Valley**	**Bean Flat Rest Area**	**West Wendover Airport**	**NV/UT**	**All sites**
SNL, LANL, UM, SMU, KUT, TDA, JPL, AFRL	SNL, LANL	JHU	OSU, UH	UH, AFRL, INL	LANL, AWE, BSU, NNSS

6. Instruments and Deployment

The team deployed over 400 sensors combined among all participating institutions, marking the most instrumented re-entry in history. For clarity, we present instruments and describe field deployments by instrument type (e.g., infrasound, seismic, etc.). Because it is not possible to include the particulars for that many instruments in the main text, we include the detailed list (consisting of the instrument make, sampling rate, the geographical coordinates, and the affiliated institution) in the Tables in the appendices. Our goal was to deploy instruments beneath the trajectory as well as perpendicular to it wherever possible in order to evaluate signal characteristics as a function of the SRC flight along and away from the propagation path (see Figure 3). The numbers and type of instruments each institution deployed are shown in Table 2.

Table 2: Summary of all instruments observing the re-entry of OSIRIS-REx. The detailed list of instruments with geographical coordinates can be found in Appendices.

Institution	Infrasound (single sensor)	Infrasound (array)	Total # of sensors in arrays	Large N-array (# of sensors)	Audible microphone	Smart phone	Seismic	DAS	GPS	Balloons
SNL	47	3 (x4)	12	-	-	2	19	-	-	6
LANL	6	2 (x4) + 1 (x6)	14	-	1	1	6	2	5	
AWE	-	1 (x4)	4	-	-	-	-	-	-	
BSU	-	3 (x4), 1 (x44)	56	-	-	-	-	-	-	
JHU	-	-	-	-	-	-	11	-	-	
JPL	-	-	-	-	-	-	-	-	-	2
KUT	-	1 (x4)	4	-	5	-	-	-	-	
OSU	12	1 (x4)	4	-	-	-	-	-	-	
SMU	-	1 (x4)	4	-	-	-	-	-	-	
TDA	-			114	-	-	-	-	-	
UH, AFRL, INL	-	-	-	-	-	33	-	-	-	
UM	-	2 (x4)	8	-	-	-	20 + 96	-	-	
	65	16	106	114	6	36	56	2	5	8

6.1 Ground-based Infrasound and Audible Acoustic

SNL deployed three 4-element arrays and 47 single sensor stations in the West and East Regions. The three infrasound arrays, deployed in the West Region, consisted of analog and digital Hyperion sensors arranged in a triangular formation. Hyperion sensors are manufactured by Hyperion Technology Group, Inc. and are widely used in a variety of infrasound monitoring applications (e.g., Bowman and Albert, 2018). One array was at the EUE, in the northeast corner, and the other two were in Newark Valley along Strawberry Rd. We aimed to arrange the arrays into an "L", such that two arrays are positioned roughly parallel to the nominal OSIRIS-REx trajectory (~10-12 km shortest path), and one perpendicular to it (~24 km shortest path). The reasoning is that such configuration could potentially capture the signals from different parts of the trail and help evaluate signal properties as it propagates away from the re-entry path. Each array had two colocated seismic nodes. The instruments were powered by marine deep-cycle batteries and solar panels. Timing was tracked through GPS.

In addition to the three arrays, SNL and DTRA also deployed 46 single stations consisting of Gem infrasound loggers (Figure 4A) in various locations (30 in the West Region, and 16 in the East Region). Gems (version 1.01) are self-contained sensor loggers optimized for deployment and maintenance in large numbers (i.e., small, lightweight, low power consumption, cable-free, and fast deployment process) (Figure 4A) (Anderson et al., 2018). They sample at 100 Hz, with a flat response between 0.039-27.1 Hz and root-mean-square self-noise of 1.55 mPa (0.5-2 Hz) and 3.9 mPa (0.1-20 Hz). Gem infrasound loggers have previously been used in campaigns using large numbers of sensors (Anderson et al., 2023; Rosenblatt et al., 2022; Scamfer and Anderson, 2023), campaigns where ease of concealment was essential (Ronan, 2017; Tatum et al., 2023), and airborne infrasound recording requiring a lightweight sensor (Bowman and Albert, 2018; Bowman and Krishnamoorthy, 2021; Krishnamoorthy et al., 2020; Silber et al., 2023b). Twenty-three Gems were installed along Strawberry Rd. to form a transect relative to the nominal trajectory, extending both north and south. Out of these, 11 were to the south relative to the nominal trajectory (~44 km due south, and ~40 km shortest distance), and 12 to the north (~56 km due north, and ~51 km shortest distance). The approximate separation between stations was 5 km. The sensors were powered with batteries and portable solar panels. To reduce the adverse effect of wind noise, Gems were emplaced inside bushes, but the solar panels were left exposed. The remaining 7 Gems were deployed about 3-5 km from and parallel to the nominal ground track, extending from the point of peak heating towards east, just beyond Strawberry Rd. The total end-to-end distance was ~65 km. In the Eastern Region, SNL deployed 15 Gems. Four of these were very close to the nominal trajectory (~1 – 3 km) and in the vicinity of US Route 93 Alternate (NV). Some ~45 km to the east, ten Gems were installed along the NV-UT state line, forming a 41 km long transect (N Ibapah Rd.), with an additional Gem positioned slightly to the west to coincide with the nominal re-entry path. All instruments were installed two days before the OSIRIS-REx re-entry and removed either immediately after the re-entry or the next day.

TDA Research deployed a 115-element Large N-array, collocated with SNL's infrasound array in the northeast corner of EUE, in a 100 x 100 m array. The sensors (Figure 4E), designed and built by TDA Research Inc., were previously tested during a controlled field experiment. This observational campaign was the second fielding, and the first time the sensors were used against a real-life event. TDA's sensors are low cost, and specifically designed to be networked into large and dense arrays with hundreds of sensors and wirelessly stream data to a central computer. The array design is modular and flexible, and its size can be anywhere from 5 sensors up to 500 sensors added in groups of five. These sensors have a sensitivity of <0.1 Pa and a sampling frequency of 200 Hz (that can be increased up to 330 Hz if needed). Each sensor has an on-

board battery with a battery lifetime of approximately nine days. They also come equipped with a solar panel that will recharge a day's worth of power in 1-2 hours of sunlight and will fully recharge the sensors in 9-13 hours. They are located using a differential GPS system with accuracy of <1cm and clocks from all sensors in the array are synced to within 1 ms. The sensors weigh 0.703 kg each and are 33 cm tall when fully assembled. TDA's sensors minimize wind noise by sampling at only 1.3 cm off the ground, taking advantage of the ground's boundary layer to reduce effective wind speed by 75%.

There were three teams from LANL, two in the West Region (DAS/seismo-acoustic, and GPS (see Section 6.5)), and one in the Distal Region. The DAS/seismo-acoustic LANL team in the West Region deployed DAS at EUE and Newark Valley, also collocating infrasound (Figure 4B) and seismic sensors. Infrasound sensors (Hyperion IFS-3000) were installed at strategic locations along the DAS fiber (for complete instrumentation details, see Appendix). Additionally, at the Newark Valley site, a PCB microphone sampling at 50 kHz was deployed near the DAS interrogator setup location, and a personal iPhone was filming during the re-entry.
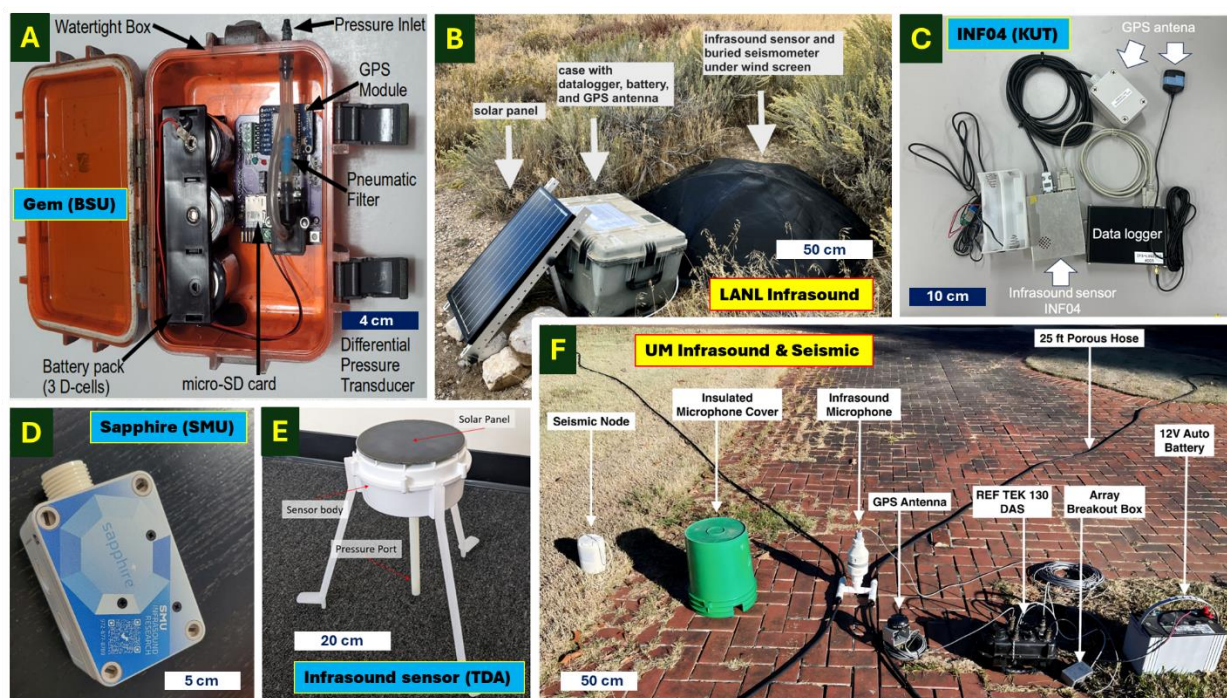

Figure 4: Representative examples of infrasound and seismic sensors and their field installations. (A) Gem Infrasound logger developed by BSU (photo credit: J. Anderson); (B) infrasound installation (LANL) (photo credit: C. Carr); (C) INF04 infrasound sensor (KUT) (photo credit: Y. Nikishawa); (D) Sapphire infrasound sensor (SMU) (photo credit: E. Silber); (E) TDA's infrasound sensor (photo credit: D. Eisenberg); (F) Infrasound and seismic instruments (UM) (photo credit: S. Bazargan).

The Distal region LANL team (alongside AWE, BSU, and NNSS) focused on infrasound data collection at distal infrasound stations. The high speed of arrival and the known time and path made this an ideal opportunity to test LANL's shock wave propagation estimate algorithms (Blom et al., 2024). Three arrays were deployed by LANL, one in Price, UT, one in St. George UT, and one on the north side of the NNSS, NV. These sites were chosen because an early estimate of regional infrasound arrivals indicated that they were likely to occur at these locations. The sensors deployed were Hyperion IFS-3000 infrasound sensors. Digitization was done with RefTek 130 digitizers powered by batteries that were kept charged by solar panels. These three arrays were deployed during the week prior to the re-entry. There were no team activities on the day of the re-entry.

At EUE, KUT deployed five microphones, as well as four infrasound sensors (SAYA INF04), the same kind as those used to observe Hayabusa 1 and Hayabusa 2 SRCs (Figure 4C). Hayabusa 1 was also observed with Chaparral microbarometers (Ishihara et al., 2012; Sansom et al., 2022; Yamamoto et al., 2011). The sampling rate of SAYA INF04 was 100 Hz (using Mathematical Assist Design Lab's INFLOG 2020). These infrasound sensors were arranged to form an elongated north-south triangle array (see Appendix for sensor locations).

UM installed a four-element infrasound array at each of two subarrays of the seismic array (described in the next section) at EUE. Instruments were made by VLF Designs and are flat to pressure between 0.25 to 25 Hz. These were placed on the ground surface within a plastic bucket insulated with 10cm rubber foam. Four porous 7.5m hoses attach to the bottom pressure manifold of the microphone. The four elements were arranged in a triangular configuration with a central element. Elements communicated with a RefTek 130 digitizer via 30 m cables to a breakout box that routed infrasound signals to channels 1-4. Timing was through GPS. The instruments and digital acquisition system were powered by a 12V car battery (Figure 4F). The rationale for having two infrasound arrays was to ensure that we could record the atmospheric pressure signal at a minimum of one position with the other being a backup. The small aperture (~60m) infrasound arrays precluded high resolution for determining the incident wave slowness and azimuth for the expected near-vertical incidence angle for the incoming N-wave. However, having four instruments in each array added an additional redundancy in measuring the incident wave pressure to compare with the test seismometer that was placed at the center of each array.

SMU deployed four lightweight portable Sapphire sensors (Figure 4D) at the EUE. The Sapphire is an infrasound nodal recorder developed at SMU inspired by the Gem infrasound node (Anderson et al., 2018) and similar in design (although developed independently) to the node

described by den Ouden et al. (2021). The Sapphire response is reasonably flat above 0.1 seconds with a sensor that is factory calibrated to 0.25% amplitude response, enabling the recorder to apply the factory calibration constant and log pressures in units of pascals thus for most experiments avoiding the need to do instrument corrections. The unit records continuously for about two weeks on four AA batteries, recording at 128 Hz with a GPS controlled clock. Although the Sapphire sensor has a higher self-noise than more expensive infrasound microphones, its low-cost, good calibration, quick deployment, and small size make it convenient for many experiments that expect reasonable signal-to-noise (SNR) in the 1-5 Hz band.

OSU set up their instruments at the ENV, deploying three different models of microbarometers. A 4-sensor infrasonic array was formed with Chaparral Physics Model 64S sensors and deployed at ENV. Each sensor had a nominal sensitivity of 0.08 mV/Pa and a flat response to within 3 dB from 0.01 Hz to 245 Hz. Each sensor was mounted within a weatherproof case (1300 Case, Pelican). A single data acquisition system (PGS-140 4-channel, Pegasus) was used to record the Chaparral Physics sensors at 1000 Hz. The nominal separation between each sensor and the center sensor was 60 m, which produced an aperture of 112 m. OSU also deployed eight model ISSM23 microbarometers manufactured by the Wilson Engineering Research and Development (WERD). These sensors had a nominal frequency range of 0.1 to 200 Hz and had on-board sampling at 400 Hz. One of the sensors malfunctioned during the deployment leaving only seven that successfully recorded the re-entry. Four of the sensors were arranged in a triangle with an aperture of 51 m and centered on the Chaparral Physics array center sensor, with the fourth WERD sensor colocated at the center. The remaining three WERD sensors were positioned around the southwest sensor of the Chaparral Physics array with an aperture of 51 m.

OSU also deployed five Gem infrasound loggers (Anderson et al., 2018). Each sensor was secured within an enclosure that was then secured inside of a small Styrofoam box with the side walls replaced with the windscreens developed in Swaim et al. (2023). Three of the Gem sensors were arranged in a triangle with an aperture of 49 m and the east corner of the triangle colocated with the center Chaparral Physics sensor (and the one WERD sensor). It should also be noted that the UH also colocated a RedVox sensor at this central location, and UH colocated several of their sensors with OSU sensors. The remaining two Gem sensors were located between ENV and the OSIRIS-REx SRC flight path to the south of the airport. These Gem sensors were 26 km and 34 km south of the ENV deployment.

UH, along with AFRL and INL, deployed smart phones with RedVox app which utilizes the phone's built-in microphone (Garcés et al., 2022) in a variety of locations, including the West, East, and

Distal Regions. Deployment locations in the East Region included Clive, UT, Dugway, UT, and around US Route 93 Alternate, NV.

The BSU infrasound campaign used Gem infrasound sensors (version 1.01). The instruments used belong to BSU and were deployed as part of a temporary network active between July-October 2023. The southwest Idaho infrasound network operated by BSU was deployed in Reynolds Creek Experimental Watershed (Seyfried et al., 2018) from July-October 2023 with objectives of recording a prescribed wildland fire and regional signals in addition to the OSIRIS-REx entry. The large array ("TOP") included 44 sensors approximately in a rectangle with overall dimensions of 210 m x 120 m; its large size was intended to facilitate detecting weak signals while providing precise backazimuths in beamforming operations. Additionally, three four-element small arrays (JDNB, JDSA, JDSB), were deployed within 1.5 km of TOP, helping to increase the spatial extent of the overall network. The smaller dimensions of these arrays are due to being constrained to small protected zones within the anticipated prescribed burn area. When possible, sensors were placed in or under shrubs in order to mitigate wind noise in these treeless sites.

6.2 Seismic

SNL deployed two seismic nodes colocated with each infrasound array. The nodes were buried at EUE because we had permission to dig holes. However, land permits at the other two arrays did not allow for digging and the nodes were placed on the surface. An additional 12 seismic nodes were deployed at EUE, distributed across a large area. As mentioned in the previous section, LANL installed 6 seismometers colocated with infrasound sensors (see Appendix for further details).

At EUE, UM also set up seismic sensors. A 1 km aperture, phased seismic array was sized to fit in the northern part of county land associated with the EUE (see Appendix C). The EUE was chosen because of its proximity to the ground track of the incoming capsule trajectory (within 10 km) and because Eureka County allowed seismometers to be buried. The phased array is relatively unusual and based on the "Golay 3x6" geometry (F. Followill, personal communication 2006). It consists of 6 tripartite subarrays arranged in a surprisingly open geometry following design principles of minimizing the number of array elements while maximizing the array spatial bandwidth (Followill et al., 1997). This can be seen in the co-array diagram that shows uniform sampling in space (Figure S16 in Appendix A). The broadband array response (Nawab et al., 1985) shows a highly focused beam that can resolve the slowness of the expected infrasound signal to 0.02 s/km. Instrumentation for the seismic array elements consisted of Magseis-Fairfield three-component nodal seismometers (see Appendix C). These seismometers have a low-

frequency corner near 5 Hz, have self-contained GPS timing, and power and data storage for 30 day deployments. Installation consists of digging a 20 cm deep hole with a posthole shovel such that the top of the seismometer is within 5 cm of the surface in order to maintain GPS lock. Seismometers were oriented with respect to the North using a magnetic compass. Instruments were installed on September 21 and 22 at locations determined using a handheld GPS receiver. Thus, location accuracy is estimated to be within 3m of the target locations. Note that 20 seismic sensors served to detect OSIRIS-REx. The refraction profiles included 48 vertical component geophones and 48 horizontal component geophones but these were not used to detect the SRC signals.

At the BFRA site, JHU installed Fairfield ZLand 3-component nodes equipped with GPS timing and inbuilt power supply. These are deployed from a handheld terminal and placed in a small hole in the ground. Recovery also uses this terminal. The sampling rate is 2000 Hz. Instruments were placed into an 11-station array, in a cross-shape with the long axis aligned parallel to the OSIRIS-REx trajectory. The field site was left unattended, and instruments were collected back in the afternoon after the re-entry.

6.3 DAS with Co-located Seismo-acoustic Sensors

LANL deployed single mode optical fiber at two sites: EUE and in Newark Valley. Fiber was laid on the ground (deployment photos are in Appendix A). An AP Sensing instrument (N5225B-R100) was used at the airport to probe 4.5 km of fiber. The AP Sensing DAS had a sampling frequency of 500 Hz, a gauge length of 5 m, and a channel spacing of 1.23 m. In Newark Valley, a Silixa iDASv2 (Version 2.4.1.111) and an Alcatel OptoDAS were connected to 7.5 km of single mode optical fiber. The iDAS used a sampling frequency of 500 Hz, a gauge length of 10 m, and a channel spacing of 2.0 m. The OptoDAS used a sampling frequency of 10 kHz, with a gauge length of 5.1 m, and a channel spacing of 1.02 m. All DAS units operated intermittently for testing purposes in addition to during the re-entry, unlike the seismometers and infrasound sensors that operated continuously. LANL installed six of each colocated seismometers (Geospace HS-1 3 Component) and infrasound sensors (Hyperion IFS-3000) at strategic locations along the DAS fiber (for complete instrumentation details, see Appendix). The seismometers and infrasound sensors recorded at 200 Hz with each seismometer-infrasound sensor pair connected to a RefTek 130 datalogger with timing information provided by Garmin GPS 16x-HVS antennas. All instruments were deployed specifically for the purposes of capturing the re-entry. Instruments were installed over several days prior to the re-entry, and removed by the evening of 24 September 2023 (local time).
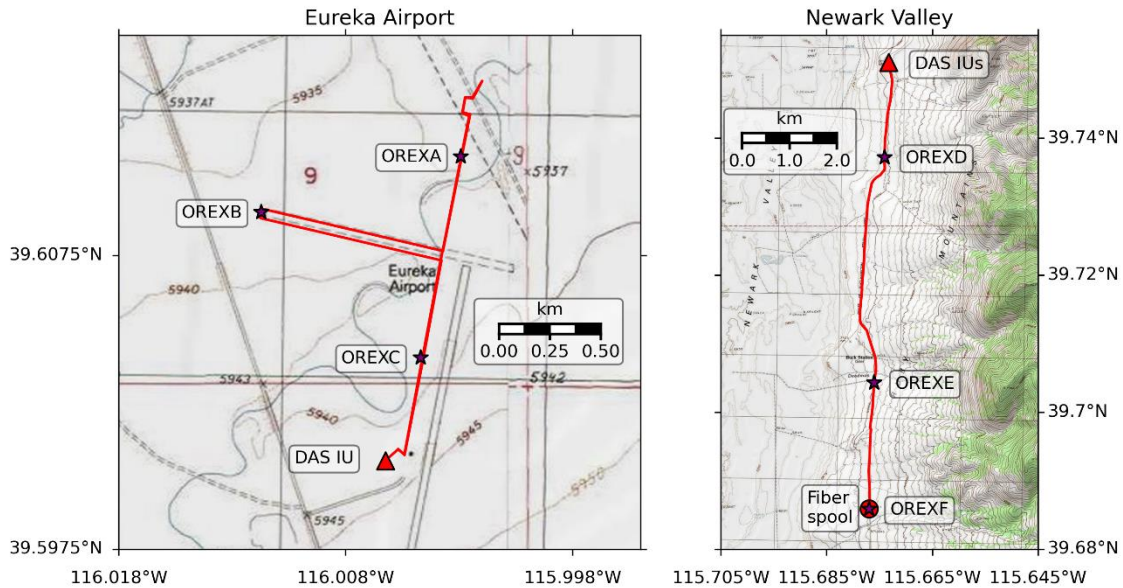
Figure 5: Map of DAS and colocated seismometers and infrasound instruments deployed at two sites: (left) the Eureka Airport and (right) in Newark Valley. OREXA, B, C, D, E, and F are colocated seismometer/infrasound pairs. DAS IU(s) indicates the DAS interrogator unit(s). At the Eureka airport, fiber was placed running from the DAS IU towards OREXC, and continuing along the edge of the main taxi runway before bending 90 degrees towards the west (towards OREXB) along the cross runway, then returning to the main taxiway and continuing north towards OREXA. The fiber returned from the turnaround point to the north of OREXA and continued directly towards OREXC without returning to OREXB. In Newark Valley, the fiber ran from the DAS IU south past OREXD, OREXE, and OREXF. A spool with the remaining fiber was placed near OREXF.

6.4 Balloons

SNL and JPL deployed balloons carrying sensor payloads. There are several types of balloons capable of bearing infrasound payloads. All of them depend on relatively low winds at the launch site, and some have additional restrictions, such as requiring sunlight to fly. To increase the odds that at least one balloon would be successfully deployed during the OSIRIS-REx overflight, SNL and JPL deployed two helium zero-pressure balloons, two helium meteorological balloons, two 7 m diameter heliotrope solar hot-air balloons towed aloft using helium meteorological balloons, and two 'cloudskimmer' 3.5 m heliotrope solar-hot air balloons. Each balloon carried a parachute to slow the payload during descent. They also carried a flight termination system that ended the deployment when the balloon crossed a pre-programmed geofence and/or after a certain amount of time had elapsed. Some balloons utilized Balloon Ascent Technologies Bounder and others used a High Altitude Science Stratocut termination system. The balloons were tracked using StratoTrack Automatic Package Retrieval System (APRS) radios that transmitted during flight and

28

a SPOT TRACE unit that reported the payload position after landing using the Globalstar satellite network. The location of this equipment on the balloon is shown in Figure 6.
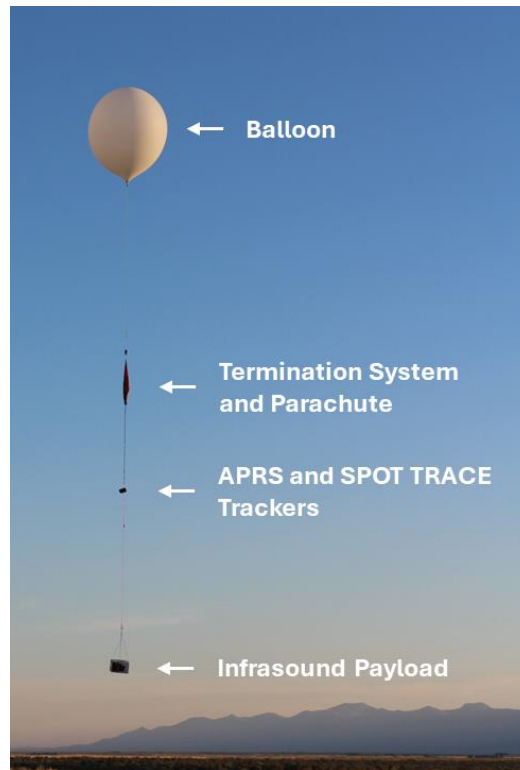

Figure 6: Example infrasound balloon configuration from the OSIRIS-REx deployment. This is the low-altitude weather balloon just after release. Photo credit: R. Lewis.

Helium zero pressure balloons climb until they reach their neutral buoyancy altitude. Two zero pressure balloons with a maximum capacity of 4300 cu ft (121.8 m^3) were fielded, each targeting a different altitude in the lower stratosphere. The sensor packages consisted of Paroscientific Digiquartz 15A-IS microbarometers and an InertialSense μINS inertial measurement with a Raspberry Pi flight computer and custom-built interface board (similar to Brissaud et al., 2021). The Paroscientific microbarometers recorded at 158 Hz with an internal five-stage anti-alias filter set at 25.1 Hz, providing a pre-digitized output. The inertialSense IMU was sampled at 15 Hz. Each balloon had two sensor packages separated by a 33 m tether. The inertialSense IMU also provided timing information from the Global Navigation Satellite Systems (GNSS) network to the Paroscientific barometers through the custom interface board for timestamps accurate to 1 microsecond for time-of-flight analysis.

Meteorological balloons climb continuously until they either burst or the flight is terminated by other means. Despite relatively high levels of wind noise during ascent, Popenhagen et al. (2023)

found that distant acoustic events could be recorded on such platforms. Thus, we deployed two meteorological balloons with infrasound payloads: a Kaymont 3000 g envelope released early with a rapid ascent rate and a Kaymont 600 g envelope released later with a very slow ascent rate. The rapid ascent balloon was meant to capture the OSIRIS-REx signal in the lower/middle stratosphere, and the slow ascent balloon was meant to capture the signal within a few acoustic wavelengths of the ground. Each balloon carried two InfraBSU microbarometers (Marcillo et al., 2012) and a Camas condenser microphone (Slad and Merchant, 2021) digitized on a DiGOS DATA-CUBE recorder digitizing at 400 Hz. One of the two infraBSU microbarometers was polarity reversed, which assists in discriminating between true pressure signals and spurious non-pressure fluctuations like those caused by electronic interference (Bowman et al., 2019).

Heliotrope solar hot-air balloons rise into the lower stratosphere, where they maintain a constant altitude until sunset or the flight is terminated by other means (Bowman et al, 2020). They are less expensive and can be launched at a more rapid cadence than zero pressure balloons but have more restrictive launch conditions. This constant altitude greatly reduces wind noise on infrasound microbarometers, permitting much fainter signals to be recorded. However, the OSIRIS-REx overflight occurred too close to dawn, meaning the heliotropes would not be able to reach their neutral buoyancy in time to record the acoustic signal. Therefore, two 7 m diameter heliotropes were towed aloft by meteorological balloons and then released into sunlight, achieving level flight before the OSIRIS-REx event. After dawn, two 3.5 m 'cloudskimmer' heliotropes were launched from the ground in the hopes that their slow ascent rate would reduce wind noise to acceptable levels. One 7 m heliotrope carried a single Gem microbarometer (Anderson et al., 2018), and the other carried two Gem microbarometers separated by a 30.5 m long tether. The Cloudskimmer balloons each carried an Android cellphone running the RedVox infrasound recording app (Garcés et al., 2022; Popenhagen et al., 2023). The RedVox phones recorded pressure data at 800 Hz.

Starting about a week before the re-entry, trajectory calculations were performed at least daily in order to refine our launch times and ascent rates. The area of operation was challenging, with restricted airspace on three sides. Furthermore, the OSIRIS-REx landing site was to the east of Eureka Airport – exactly where the balloons were expected to go. Therefore, we set termination geofences to prevent balloons from drifting into restricted airspace, including the OSIRIS-REx landing site.

Balloons were launched in two batches: an initial salvo meant to capture signals at high altitude (>20 km) and the second intended for very low altitude recordings (within several acoustic

wavelengths of the ground). The first batch included the 7 m heliotrope balloons towed aloft using helium-filled meteorological balloons, one meteorological balloon with an infrasound payload, and the two helium zero pressure balloons. The first balloon was launched at 11:54 UTC, and all but one had been launched by 12:12 UTC. The final zero pressure balloon was launched at 13:12 UTC. The second batch consisted of a very slowly ascending meteorological balloon and the two cloudskimmer heliotropes. The meteorological balloon was released at 14:00 UTC and the last cloudskimmer was released at 14:13 UTC.

Despite gusty winds in the town of Eureka, conditions were calm at the airport due to a strong temperature inversion that had set up overnight. Winds began to pick up around 14:05 UTC, resulting in the decision to add helium to the cloudskimmers to help them get off the ground faster. Because of the rising wind and the imminent arrival of the OSIRIS-REx SRC, we opted not to launch the spare heliotrope balloon. Instead, we left the still-recording spare payloads at the launch site and proceeded to the pilots' lounge. After the capsule overflight, the balloon flights were automatically terminated. Payloads from the low altitude meteorological balloon and both cloudskimmers were recovered on the same day. The remainder of the payloads were recovered the following day.

6.5 GPS

LANL's GPS team deployed in the West region, with the aim of measuring and characterizing ionospheric Total Electron Content (TEC) signatures (via GPS L-band measurements) as well as atmospheric current and electric field signatures. Analyses involve modeling and measuring signature speed and period, geolocating likely sources, and estimating source strength using the LANL/GPS Rex-five stations with controlled/compact placement and large data-rate collections to probe small-scale ionospheric effects. The most significant caveat of this method, of course, is that ionospheric TEC signatures with the highest signal-to-noise ratio (SNR) are known to be tens of minutes delayed from any source in the troposphere. The LANL/GPS team deployed five GPS/GNSS Ground Stations at EUE along the runways: four along one taxiway (stations Rex-2, Rex-3, Rex-4 and Rex-5), and one at the end of its orthogonal dirt runway (station Rex-1). The geographical coordinates are listed in the appendix. Septentrio PolaRX5s GPS receivers were used in all stations with Veraphase 6000/High-Precision Full GNSS Spectrum Antennas. Standard solar panels and voltage regulators were used to supply power. Power expectations were designed to ensure that consistent power was maintained.

When properly calibrated, GPS Ground stations measure the group and phase dispersion of L-band signals (1-2 GHz) to all GNSS satellites simultaneously. These measured quantities

determine the integrated electron density along the line-of-sight or Total Electron Content (TEC) to each satellite. Nearly all of that dispersion occurs in the ionosphere, and mostly near the altitude of peak ionization (250-400 km). As a result, these lines of sight, mapped though the ionosphere, can be used to scan for small changes and to characterize and locate atmosphere-impacting events perturbing the upper atmosphere.

The GPS stations, atmospheric current, and electric field measuring instrumentation were set up a few days prior to the OSIRIS-REx SRC re-entry to ensure all units were working properly and calibrated. The GPS stations were deployed less than 400 m apart from one another to allow detection of small-scale ionospheric disturbances. The most widely separated stations were 2000 m apart, nearly spanning the EUE main taxiway. In addition, the data-measuring interval was set to 50 ms to enhance the resolution of small time-scale measurements of ionospheric disturbances. The OSIRIS-REx SRC re-entry occurred nearly an hour after dawn under clear skies.

7. Preliminary Results

Here we present a snapshot of the preliminary data and our initial results. Nearly all instruments located near the nominal trajectory (i.e., direct arrivals) successfully detected the signals produced by the re-entry of OSIRIS-REx. Additionally, numerous stations in the Distal Region also captured the signals. Illustrative examples of detections are shown throughout this section to demonstrate the remarkable success of this largest ever geophysical observational campaign of a re-entry. We note that some results are omitted from this paper because detailed analyses are underway by various teams and will be disseminated as separate studies in due course.

7.1 Witness Reports

During the anticipated time window during which the OSIRIS-REx SRC overflight was expected to take place, the teams in the West Region exercised the so-called silent observation time. At EUE, some team members were stationed at the airport entrance to prevent inadvertent vehicular intrusion into the observation zone. The highway adjacent to EUE is commonly busy, and with steady tractor-trailer traffic. We asked the local police if they could assist in temporarily closing the highway during the overflight, but the request needed to be escalated with the Nevada State police. Despite lacking direct confirmation regarding the feasibility of our request, the EUE team observed a notable absence of vehicular activity for several minutes prior to re-entry, indicative of a road closure. The area was nearly windless and very quiet, and the only dominant audible noise

came from birds and a rooster. Regrettably, approximately one minute before the anticipated OSIRIS-REx overflight, we noted a gradual resumption of vehicular activity. By the time traffic returned to full speed, the OSIRIS-REx SRC had already passed but not before some traffic noise started to become apparent. At EUE, the experiences in audible perception of a possible sound generated by the OSIRIS-REx re-entry varied. Some people perceived it as a single soft "thump", some as a double "thump", while others heard nothing. Notably, the observed audible signatures (or lack of thereof) exhibited strong dependence on the locality where the witnesses were present at the time. The sound may have gone unnoticed if individuals were engaged in casual conversation.

In Newark Valley, during the silent observation time, team members observed several airplanes, bird noise, and various wind noises. One team member out of six likely saw the OSIRIS-REx SRC. Four observers in Newark Valley heard a double boom at 14:45:52 UTC, other observers recorded the time to the minute as 14:45 UTC. Newark Valley observers perceived the sound as coming from the east (two observers), southwest (one observer), northwest (one observer). The four Newark Valley observers agreed the sound was distinct and unmistakable given the quiet conditions but could have been missed if a loud conversation had been happening. A clip from the video recorded by Carr's personal phone is included in a .tar.gz package. The animation clip begins at 14:45:40 UTC and ends at 14:46:00 UTC. A double boom is audible about 11 seconds into the clip, corresponding to 14:45:51 UTC. The sample return capsule is not visible in the recording. A more detailed account of the LANL team's visual and audible observations in Newark Valley can be found in Appendix A. There were no visual or audible observations from the BFRA site at the time of re-entry.

In the East Region, both the OSU and UH teams heard the sound. The entire OSU team viewed the re-entry from their lodging location (40.7347 N, -114.0805 E). One audible boom was heard at 14:46 UTC that was not loud but easily noticeable. The JSU team, situated at 39.2646 N, -116.0269 E at the time of re-entry, heard a clear single "thud" at 14:46:45 UTC. The OSU team had noted that the sound would likely be brushed off as another ancillary source of noise if not expected. It was very calm with little to no wind (i.e., no wind at the observation location as perceived by the team), and mostly clear skies. The team members located in Clive, UT also heard a soft, double "thump" resulting from the sonic boom.

7.2 Signal Detections on Ground-based Sensors

All SNL's arrays and most Gems detected clear signals generated by the OSIRIS-REx SRC re-entry. A plot with the arrivals received at Gem stations south of the nominal re-entry path is shown

in Figure 7. The timeseries were filtered with a highpass filter at 10 s. The difference in timing is due to the airwave travelling a longer path to more distant stations. The N-wave indicates a ballistic arrival. Station A05 was closest to the nominal trajectory (~13 km), and A01 the farthest (~40 km). More detailed analysis is needed to determine whether all stations received the signal from a single point of the re-entry path or perhaps from different points along the trajectory. The latter is more plausible when one considers the ballistic nature of the shock wave.
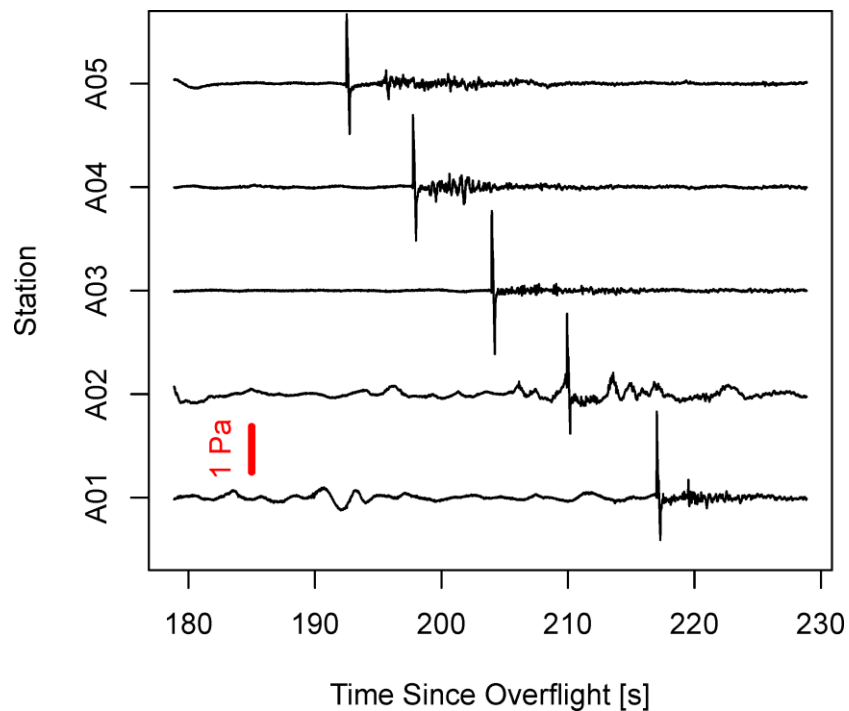
Figure 7: Signals received at Gem stations situated south of the nominal re-entry path in Newark Valley (Strawberry Rd). The timeseries were filtered (highpass, 10 s). The x-axis is in seconds from 14:45:50 UTC.

All the instruments deployed by LANL in the West Region captured the signal from the capsule. All seismometers and infrasound sensors recorded high SNR signals (Figure 8). The Silixa DAS data recorded a move out of the signal as it propagated along the fiber that can be seen without any pre-processing (Figure 8 shows data from fiber wrapped around a spool near OREXF). The AP Sensing (EUE) and OptoDAS (Newark Valley) recorded the signal, but the signal is only visible after data preprocessing. In the examples shown in Figure 8, we manually pick arrivals because the SNR is so large (red circles in Figure 8). For infrasound detection, we choose the corner at the start of the increase in pressure of the incoming N-wave (peak amplitude). For the seismic records, we pick the corresponding corner at the start of the rise towards the first high SNR peak amplitude on the vertical channel. For the DAS detection, we pick the corresponding corner at the

start of the rise toward the maximum peak in strain. Detection metadata are in Appendix A, Table S1.
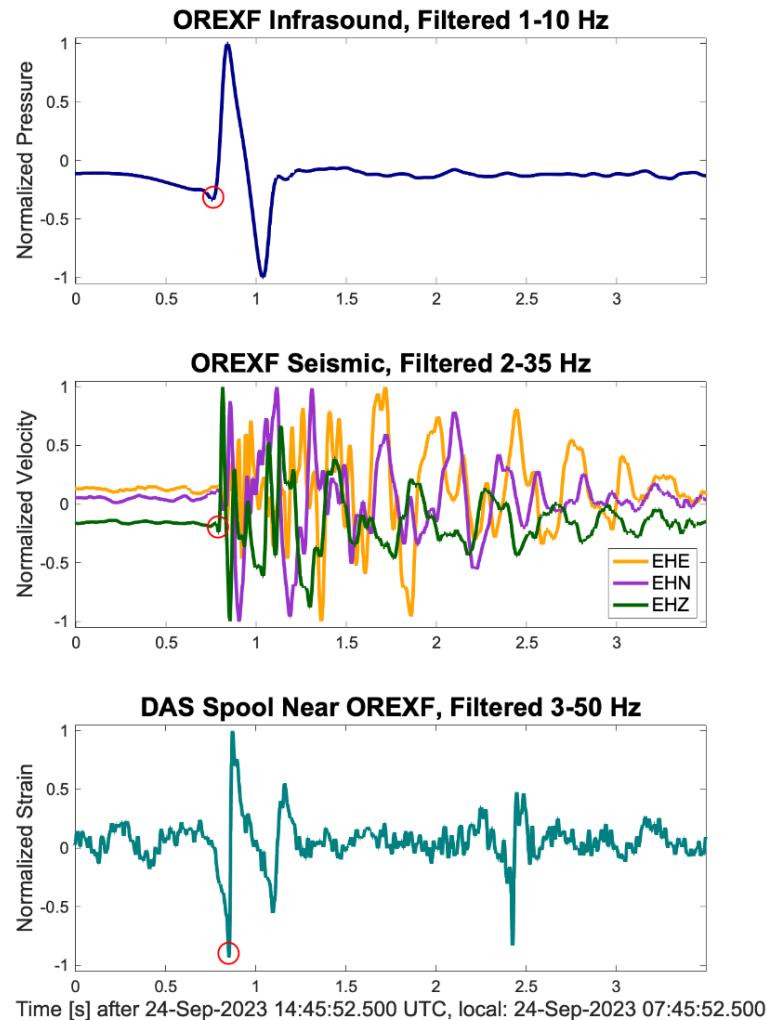

Figure 8: High SNR arrivals on the co-located OREXF (top) infrasound and (middle) 3-channel seismic sensors and (bottom) on fiber wrapped around a spool near OREXF, the sensor is at 7436 m from the interrogator at channel 3718. Data are filtered with a bandpass filter from [1-10] Hz for the infrasound channel, [2-35] Hz for the seismic channels, and [3-50] for the DAS channel. Time picks are shown with open circles.

TDA's Large N-array started collecting data at 19:23 UTC on September 23 and stopped collecting data at 15:05 UTC the next day, shortly after the re-entry. At the time of the re-entry (14:46 UTC), 114 of the 115 sensors were collecting data and detected the N-wave generated by the OSIRIS-REx SRC (clearly visible in Figure 9).
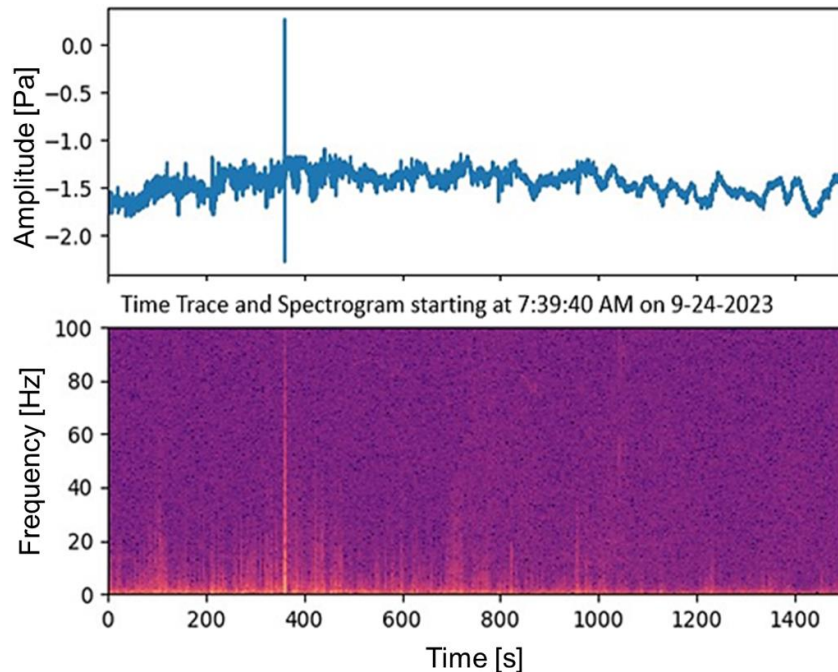
35

Figure 9: Signal detected at one of the TDA sensors of the large-N array. The strong signal is clearly visible just before the 400-second mark. The upper panel shows the timeseries while the lower panel shows the spectrogram.

Three of the four SMU infrasound sensors made a detection, clearly noticeable even without any data filtering (see Appendix A). KUT's infrasound instruments and microphones also detected the signal generated by the OSIRIS-REx SRC re-entry, with the arrival time around 14:45:59 UTC (see Appendix). The apparent direction of arrival was north-to-south, as expected. JHU recorded a clear sonic boom on all seismic stations, arriving at approximately 14:46 UTC. The lateral offset from the nominal trajectory was less than 2km.

All passive seismic and infrasound sensors deployed by UM recorded the capsule return signal. UM also obtained an extensive dataset of refraction waveforms to be used in developing P and S velocity functions for the sediments of Diamond Valley using body wave arrival times and high frequency surface wave dispersion. The refraction profile data are necessary to develop appropriate Earth models at the site. These velocity models are important for inferring the efficiency of the acoustic to seismic interaction and to understand how secondary seismic waves distort the acoustic source function as seen by a seismic instrument. Seismic signatures can be affected by local P-to-S conversions, creation of Rayleigh waves, and by the absolute values of both the P and S wave velocities in the near surface (e.g., Langston, 2004).

36

Broadband frequency-slowness analysis of the seismic array data gives an apparent velocity of 2.9 km/s and azimuth of approach of the acoustic N-wave of N02°E. We observed significant differences of both acoustic and seismic signals between the western and eastern infrasound arrays (Figure 10) suggesting differences in atmospheric wave propagation and differences in local seismic site responses. Indeed, we also saw significant differences in the seismic responses between northern and southern stations (Figure 10), suggesting the development of secondary Rayleigh waves.
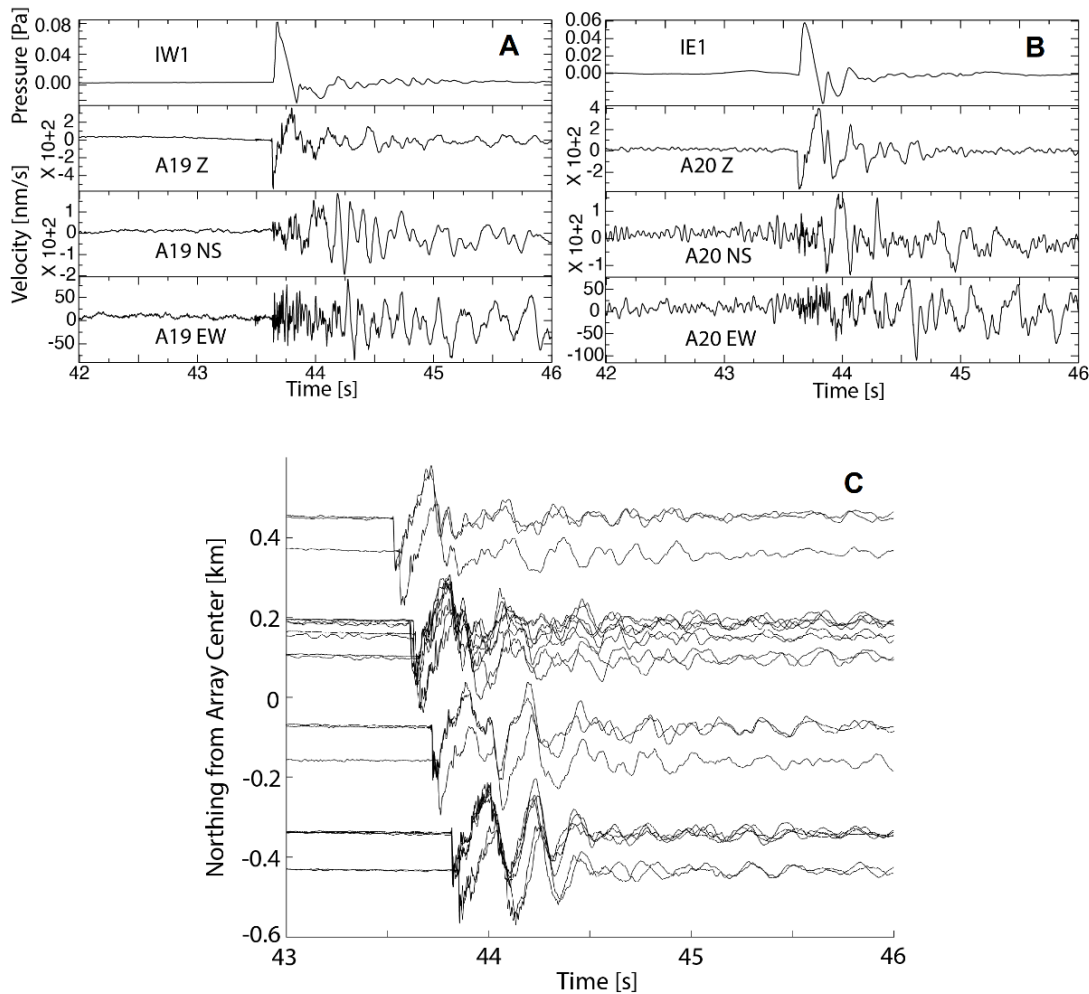

Figure 10: Comparison of pressure and ground velocity data at the central elements of the western (A) and eastern (B) UM seismo-acoustic arrays. Pressure and velocity amplitude values are provisional pending further calibration of the instruments. Time is relative to 14:45:13.818 UTC. (C) Vertical velocity waveforms from the Golay 3x6 array plotted as a function of distance from an azimuth of 0°, i.e., the data have been plotted along a virtual north-south profile with north at the top of the figure. Waveform amplitudes have been normalized. Note the large oscillating secondary arrivals for stations in the south. Time is relative to 14:45:13.818 UTC.

Smart phones running the RedVox infrasound recording app detected strong signals (see Appendix). OSU's sensors at ENV that were operational during the re-entry (14 out of 15 sensors) detected a signal at 14:47:16.5 UTC. All of these sensors were ~58 km from the perpendicular intersection of the OSIRIS-REx SRC trajectory. The received wave was an N-wave with more broadband coherent "rumbling" after the initial arrival. Figure 11 shows the signal recorded by the Chaparral array. The sensors situated south of ENV also captured the signal from the re-entry. The signal first arrived at Gem 092 at 14:46:02.7 UTC and then at Gem 074 at 14:46:17.2 UTC. These two sensors were ~25 km and ~33 km, respectively, from the perpendicular intersection of the OSIRIS-REx SRC trajectory. Both sensors had a dominant N-wave arrival with some broadband coherent "rumbling" after the initial arrival.
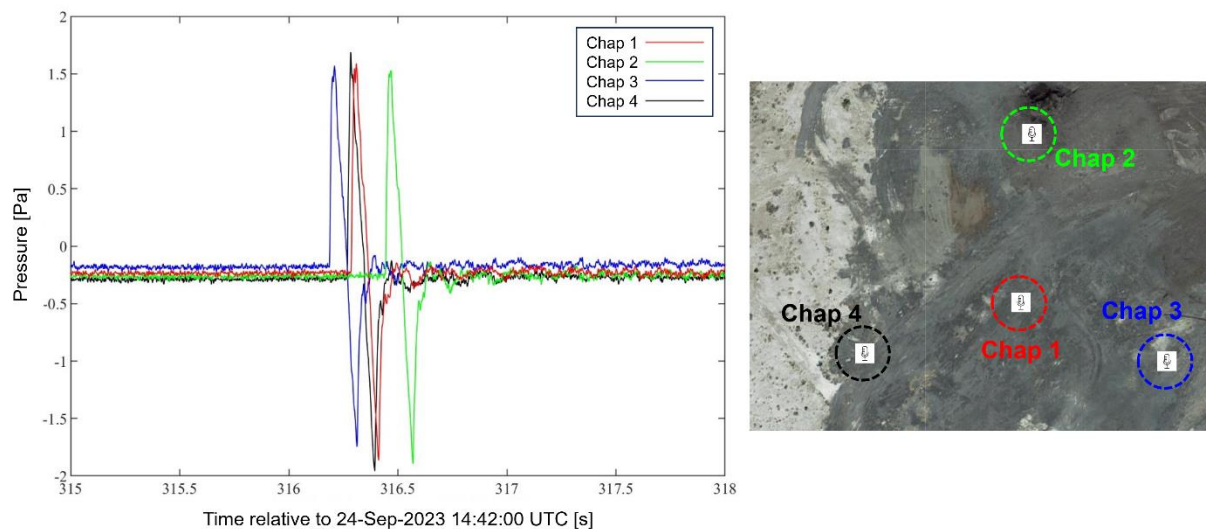

Figure 11: Left panel: Time trace from the four Chaparral Physics model 64s sensors in OSU Array 1 located at the Wendover Airport. Right panel: Satellite image showing the orientation of the sensors (Chap 1-4) with colors matching those in the left panel, which shows the signal was arriving from the south-southeast direction. The width across the map is 175 m.

In the Distal Region, early analysis from the BSU's Idaho stations show possible signals. At this location, we recorded good data from 47 of 66 sensors during the OSIRIS-REx entry. Causes of sensor failure include dead batteries, disturbance by cattle, and theft/loss. The AWE's station at the NNSS detected the signal (Figure 12). All LANL's sensors in the Distal Region performed well. The array near Price, UT did not detect the OSIRIS-REx re-entry. However, the other two arrays (NNSS array (Figure 12) and the St. George, UT array), did capture signals from the re-entry. The stations at NNSS are situated ~260 km from the point of peak heating.

Infrasound signals in the 1-4 Hz passband were observed on two small aperture 4-element arrays at ~420km west-southwest of the OSIRIS-REx landing site (Figure 12) exhibited backazimuths (the direction from which the signal arrived) of ~345° (i.e., from just west of north) consistent with signal generation along the re-entry trajectory. The arrays are separated by a horizontal distance of 1500m and a vertical distance of 300m, with PSDJK (AWE) located on top of a mesa and OREX1 (LANL) located in the base of a steep-sided valley.

Although the signals at each array are qualitatively similar in terms of duration and waveform variation, beamforming results at OREX1 have a higher resolution likely due to the larger array aperture of 160 m (compared to 100 m for PSDJK). Despite the close proximity of the arrays there are significant differences in the temporal variations of background noise amplitudes. On the mesa, PSDJK exhibits low noise in the period prior to the OSIRIS-REx signal, such that a persistent high-frequency low-amplitude acoustic source can be observed towards the west. During and after the OSIRIS-REx signal the noise amplitude at PSDJK increases, obscuring the low-amplitude signal. The opposite is observed at OREX1 in the valley; here, high amplitude noise prior to the OSIRIS-REx signal obscures the persistent source to the west. During and after the OSIRIS-REx signal the noise amplitude drops allowing the persistent source to be observed. This indicates how wind generated noise at an array can be highly localized, and the impact it has upon signal detection.
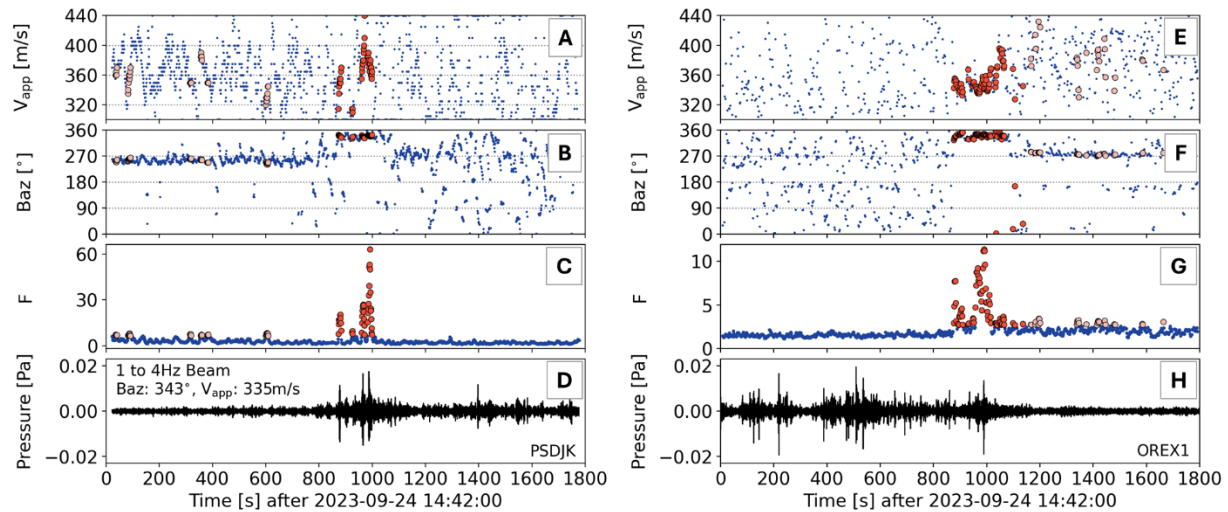

Figure 12: Left: AWE's PSDJK array. Right: LANL's OREX1 array. Panels top to bottom show values of apparent velocity (V_{app}), backazimuth (Baz) and F-statistic (F) corresponding to the beam direction that exhibits the highest signal coherence across consecutive 4 s long windows (overlapping by 50%). Orange dots represent time periods for which there is a >95% probability that the window contains a signal with a signal-to-noise ratio greater than, or equal to, four. The lowermost panel shows the 1 to 4 Hz beam for a backazimuth of approximately 345°. Note that the OSIRIS-REx signal is seen above a persistent low signal-to-noise ratio signal arriving from a backazimuth of approximately 260°.

7.3 Balloon-borne Infrasound

The high-altitude meteorological balloons and heliotropes traveled furthest west (relative to other balloons) due to their relatively low ascent rates (Figure 13) and were over halfway to the capsule's altitude at the time of overflight (Figure 13). The zero pressure balloons were about 50 km from the launch site at the time of the overflight. The cloudskimmers and low altitude meterological balloon were still quite close to the launch site because they were released just before the overflight. Ground winds were generally low, allowing for the successful inflation and launch of the balloons. While a strong tropospheric jet was present, the winds were not rapid enough to carry the balloons into the termination zone before the OSIRIS-REx SRC re-entered. The balloon data are being analyzed and will be published in the near future.
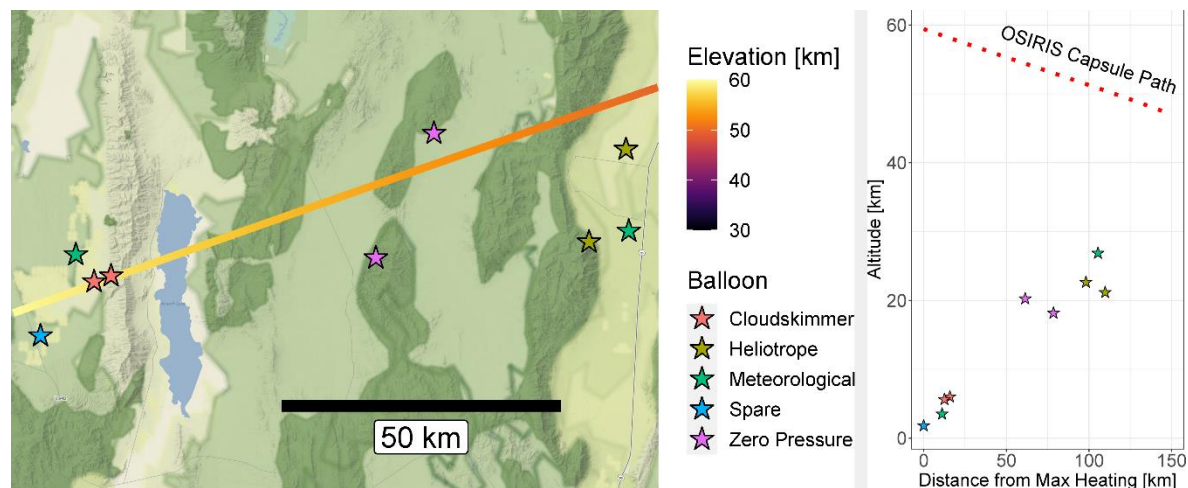

Figure 13: Left: Locations of OSIRIS-REx balloons compared to OSIRIS-REx flight path and altitude. Map imagery from Stadia Maps. Right: Altitude of balloon payloads at the time of OSIRIS signal arrival compared to the altitude of the OSIRIS-REx capsule.

7.4 GPS

LANL GPS team observed several signatures originating from the incoming OSIRIS-REx (SRC) (Figure 14). Several faint signatures were detected in the TEC along lines of sight from our GPS ground units through the ionospheric peak density altitudes, arriving more than 10 minutes after the re-entry as expected (having traversed 300 km from maximum shock-wave altitudes to the ionospheric peak) (Figure 14, left panel). Estimated ionospheric signatures were traveling at speeds expected in the thermosphere (greater than 800 m/s), much faster than ground speeds (343 m/s). We were also able to observe signatures (possibly moving at faster speeds) in the refined GPS scintillation measurements. In addition, data from 12 publicly available GPS ground

stations within 300 km of Eureka (NV) were used to approximate the location of the final descent after the parachute deployment stage (Figure 14, right panel). The immediate results of the observational campaign are encouraging. The LANL GPS team will continue to examine the data from the OSIRIS-REx capsule return and refine their analysis methodologies.
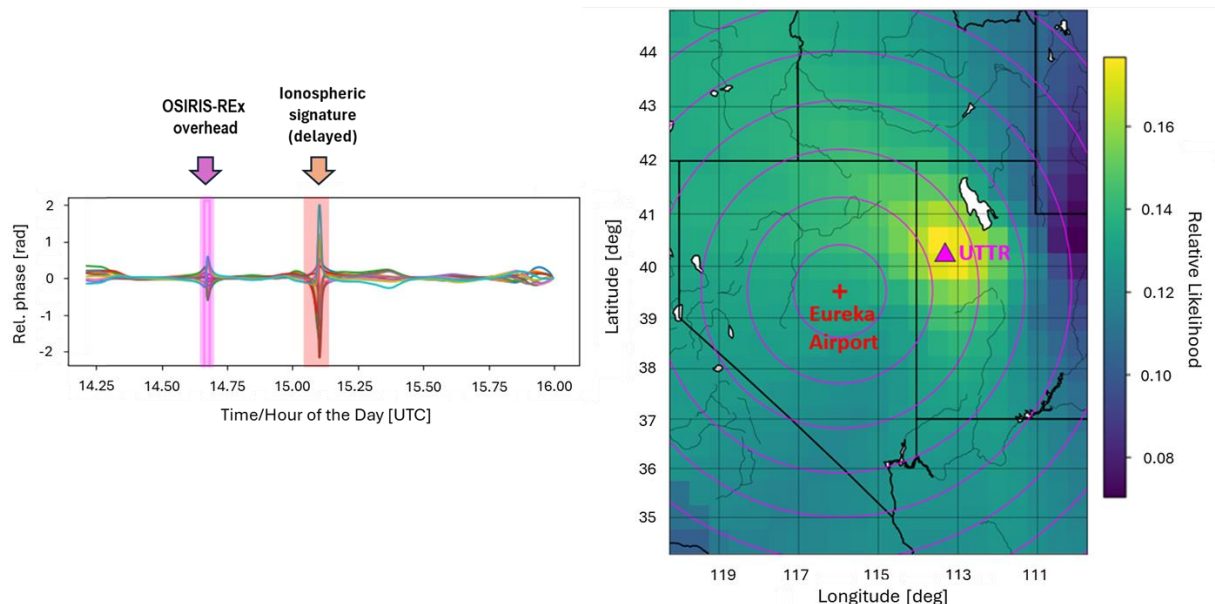

Figure 14: Left: Relative LANL GPS filtered precision TEC measurements, identifying 10-minute acoustic signatures. Right: Most likely acoustic source location identified from 10-minute TEC waves derived from public GNSS data.

8. Conclusions

NASA's OSIRIS-REx SRC returned to Earth on September 24, 2023, delivering precious cargo consisting of physical samples of the asteroid Bennu. This was the first asteroid sample return mission for the USA. Considering that SRCs come from interplanetary space at hypervelocity, they can serve as ideal analogues for studying meteor phenomena. The most recent re-entry over the USA was in 2006 with the return of NASA's Stardust mission. The OSIRIS-REx SRC's hypersonic flight through the atmosphere provided an exceptionally rare opportunity to carry out geophysical observations of a well-characterized source with known parameters, including timing and trajectory.

A large team of researchers from 16 institutions gathered to perform a coordinated geophysical observational campaign at strategically and carefully selected locations that were projected to provide robust and high-fidelity data. Over 450 ground-based sensors including infrasound,

seismic, DAS, and GPS were deployed. Moreover, several balloons carrying infrasound sensors were launched with the aim of capturing the signals at high altitude. This was the largest geophysical observational campaign of a re-entry ever performed, collecting a wealth of valuable data that is expected to promote scientific inquiry for many years to come.

The observational campaign was highly successful, with detections on nearly all instruments, near and far. Here, we present our early results collectively, noting that more focused studies will be disseminated in due course. Data collected during this effort will be eventually made openly available.

Here we summarize our preliminary findings and conclusions:

i. Infrasound and Seismic: The campaign to record the OSIRIS-REx capsule return seismo-acoustic signals was remarkably successful. Nearly all passive instrumentation at the variety of vantage points recorded the signal generated by the re-entry. Most instruments performed well, including arrays, single stations, Large N-array, and smart phones. A diverse range of instruments recorded the signal at distances from beneath the nominal trajectory to several hundreds of kilometers from the nominal trajectory. The seismic array design proved to be able to accurately determine the wave characteristics of the incoming acoustic signal, and we observed interesting seismo-acoustic interactions at our infrasound subarrays. Our refraction work is also an important element of the experiment since it will yield baseline information on near-surface P and S wave velocities that are important constraints on the nature of the acoustic-seismic interaction.

i. DAS: As expected, within each site (Eureka Airport and Newark Valley), detections sweep across the instruments from North to South, with instruments closer to the trajectory recording arrivals before instruments further from the trajectory. This event marks the first time that DAS recorded a re-entry event. In Newark Valley in particular, the arrivals were clear across much of the 7.5 km of deployed fiber, despite the simple placement of cable directly onto the ground (no trenching). This is particularly promising in light of rapid deployment observation campaigns, where trenching may be logistically prohibitive.

ii. Balloons: A diverse set of balloon-borne acoustic stations were fielded during the OSIRIS-REx observation campaign, with the hope that at least one of them would succeed. Fortunately, every airborne sensor recorded data during the overflight. While careful planning and experienced launch crews played a major role in this achievement, the weather played a critical part as well.

iii. GPS: The GPS observational campaign was successful. Several faint signatures generated by the OSIRIS-REx SRC during re-entry were detected in the total electron content (TEC) and L-band scintillation (directly). Additionally, we were able to infer the location of the final descent after the parachute using data from a dozen publicly available GPS ground stations.

This largest to-date observational campaign of a hypersonic re-entry with a multitude of geophysical instruments provided valuable insight and data collection that can serve as a blueprint not only for terrestrial applications but also for future space mission planning. Future campaigns should attempt to capture the onset of the shock wave as the object transitions into the continuum flow regime. Having radiosondes launched in various locations along the ground track to collect atmospheric data up to 40 km altitude would be of immense value. Moreover, seismic instruments extending over a longer region would further help constrain the source. Because we prioritized the West Region where the likelihood of capturing the signal would be the greatest, we did not have any dedicated seismic sensors further east. Future balloon campaigns should focus on broadening the horizontal range between the sensors and the reentering object, as well as deployments at a wider array of azimuths.

Acknowledgements:

Data availability:

Tables with the locations of the instruments are in Appendices. Tables A1 and A2 are also available in machine readable format. Data from some components of this observational campaign will be made openly available in the future. UM data collected from this experiment will be openly available from the Seismological Facility for the Advancement of Geoscience (SAGE) of the EarthScope Consortium in September 2025. Currently, the data are forming part of a PhD

thesis at the University of Memphis. LANL/GPS observational data may be released at a later date. SMU data will be made available in the near future.

Appendix A

Los Alamos National Laboratory (LANL)

Deployment Photos (DAS)
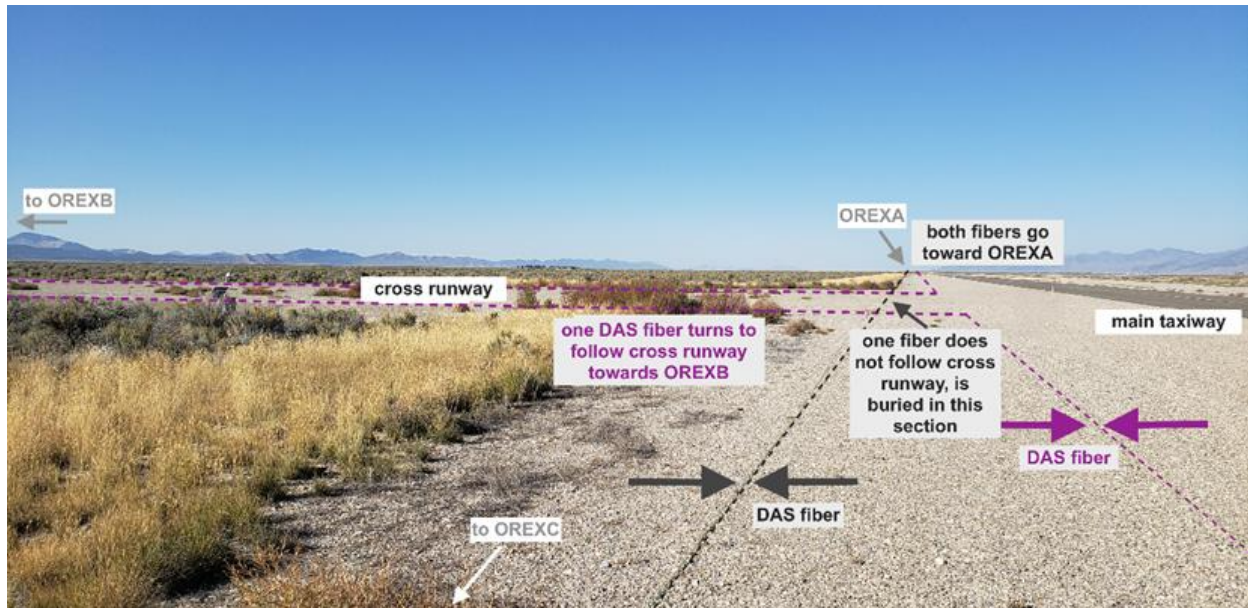
Figure S1: DAS fiber deployment at the Eureka Airport (photo credit: C. Carr).
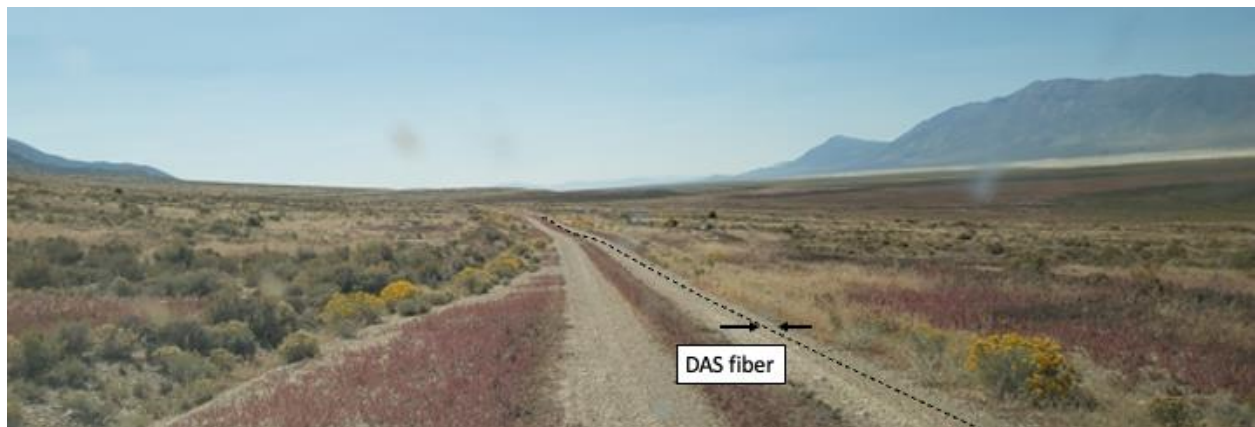
Figure S2: DAS fiber deployment in Newark Valley (photo credit: C. Carr).

Deployment Photos (GPS)

Figure S3: GPS Ground Station: Rex-2 (photo credit: R. Hasser).

Visual and Audio Observations in Newark Valley

In preparation for observing the re-entry on the morning of 24 September 2023, in Newark Valley, two team members stood at the trailer containing the DAS interrogator unit to monitor operation during the overflight. One team member sat about 50m to the north-northwest of the trailer and one team member laid on the ground about 60m to the north of the trailer. The team members maintained a quiet observation time from 07:35 AM to 08:10 AM local (14:35 – 15:10 UTC 24 Sept 23) in sunny weather. While conditions were calm earlier in the morning, as the sun rose in the valley, the wind increased such that during the quiet observation time observers described the wind as breezy. During the quiet observation time, team members observed several airplanes, bird noise, and various wind noises. At the airport, the two team members were outside the hangar and noted the weather was sunny and slightly windy. The airport observers noted that traffic noise from the nearby highway was present during the re-entry time frame.

One team member out of six likely saw the SRC. The team member (Carr) lying on the ground in Newark Valley observed a very bright whitish-yellow streaking flash. They estimated afterwards the streak covered about 5 degrees, starting nearly vertically overhead and moving roughly toward the NE. They estimated the time as 07:43:06 AM local (14:43:06 UTC) based on counting seconds since the last check of their GPS watch; they did not look at the watch at the time to maintain visual observation overhead. The other three team members in Newark Valley did not see the capsule. Team members at the airport reported they had no visual observations of the capsule.

Most team members in Newark Valley and at Eureka Airport heard a sound, though perceptions of the sound and direction of sound origin varied. Four observers in Newark Valley heard a double boom, Carr recorded the time as 07:45:52 AM local (14:45:52 UTC), other observers recorded the time to the minute as 07:45 AM local (14:45 UTC). Newark Valley observers perceived the sound as coming from the east (two observers), southwest (one observer), northwest (one observer). The four Newark observers agreed the sound was distinct and unmistakable given the quiet conditions but could have been missed if a loud conversation had been happening. At the airport, one team member heard a faint "pop" sound (time not recorded).

Carr recorded a video (duration 35 minutes, 20 seconds) with their personal cell phone, starting just after 07:35:00 AM local time (14:35 UTC) on 24 September 2023. Timing was determined by their personal GPS-enabled smart watch, and the video timing is within a second but slightly behind the time as recorded by the watch at the start of the video. Timing resolution is limited by the watch and phone. A clip from the video is included in a .tar.gz package, the clip begins at 07:45:40 AM local (14:45:40 UTC) and ends at 07:46:00 AM local (14:46:00 UTC). A double boom is audible about 11 seconds into the clip, corresponding to 07:45:51 AM local (14:45:51 UTC). This is consistent with a written observation by Carr of an audible double boom at 07:45:52 AM local (14:45:52 UTC) based on the watch. The sample return capsule is not visible in the recording.

Signal Detection Metadata

Table S1: Detection times for LANL seismometers, infrasound sensors, the DAS spool near OREXF, human observers, and a cell phone. We manually picked arrivals on unfiltered data because the SNR is so large. For infrasound detection, we chose the corner at the start of the increase in pressure of the incoming N-wave. For the seismic records, we pick the corresponding corner at the start of the rise towards the first high SNR peak amplitude on the vertical channel. For the DAS detection, we pick the corresponding corner at the start of the rise toward the maximum peak in strain. Ground distance (last column) represents the distance measured along a perpendicular back azimuth to the closest ground path of the nominal trajectory.

Instrument or Observer	Signal notes	Detection time (local) on 24 Sept 2023	Detection time (UTC) on 24 Sept 2023	Latitude (°N)	Longitude (°E)	Distance to trajectory
OREXA - infrasound sensor	N wave	7:45:57.440	14:45:57.440	39.6109883	-116.002932	5.6 km
OREXA - seismometer	impulsive arrival with coda	7:45:57.480	14:45:57.480	39.6109883	-116.002932	5.6 km
OREXB - infrasound sensor	N wave	7:45:57.520	14:45:57.520	39.60899	-116.011737	5.6 km
OREXB - seismometer	impulsive arrival with coda	7:45:57.560	14:45:57.560	39.60899	-116.011737	5.6 km
OREXC - infrasound sensor	N wave	7:45:57.720	14:45:57.720	39.6040433	-116.004643	6.3 km
OREX C - seismometer	impulsive arrival with coda	7:45:57.755	14:45:57.755	39.6040433	-116.004643	6.3 km
OREXD - infrasound sensor	N wave	7:45:51.595	14:45:51.595	39.7372017	-115.674093	1.8 km
OREXD - seismometer	impulsive arrival with coda	7:45:51.625	14:45:51.625	39.7372017	-115.674093	1.8 km
OREXE - infrasound sensor	N wave	7:45:52.485	14:45:52.485	39.7043	-115.676033	5.2 km
OREXE - seismometer	impulsive arrival with coda	7:45:52.520	14:45:52.520	39.7043	-115.676033	5.2 km
OREXF - infrasound sensor	N wave	7:45:53.255	14:45:53.255	39.6858783	-115.676975	7.1 km
OREXF - seismometer	impulsive arrival with coda	7:45:53.290	14:45:53.290	39.6858783	-115.676975	7.1 km
DAS spool near OREXF	peak in strain	7:45:53.352	14:45:53.352	39.6875	-115.67696	7.1 km
Chris Carr	visual bright streak	7:43:06 (estimated)	14:43:06 (estimated)	39.7516	115.6736	0.3 km
Chris Carr	audible double boom	7:45:52	14:45:52	39.7516	115.6736	0.3 km
Chris Carr cell phone	audible double boom	7:45:51	14:45:51	39.7516	115.6736	0.3 km
Carly Donahue	audible double boom	7:45	14:45	39.7511	-115.6734	0.4 km
Luke Beardslee	audible double boom	7:45	14:45	39.7511	-115.6734	0.4 km
Lisa Danielson	audible double boom	7:45	14:45	39.7515	-115.6737	0.4 km
Loïc Viens	audible faint pop	not recorded	not recorded	39.600158	-116.0058	6.6 km

Johns Hopkins University (JHU)

Deployment Photos

Figure S4: One of the seismic nodes deployed by JHU at the Beans Flat Rest Area (photo credit: B. Fernando).

Kochi University of Technology (KUT)

Signal Detection
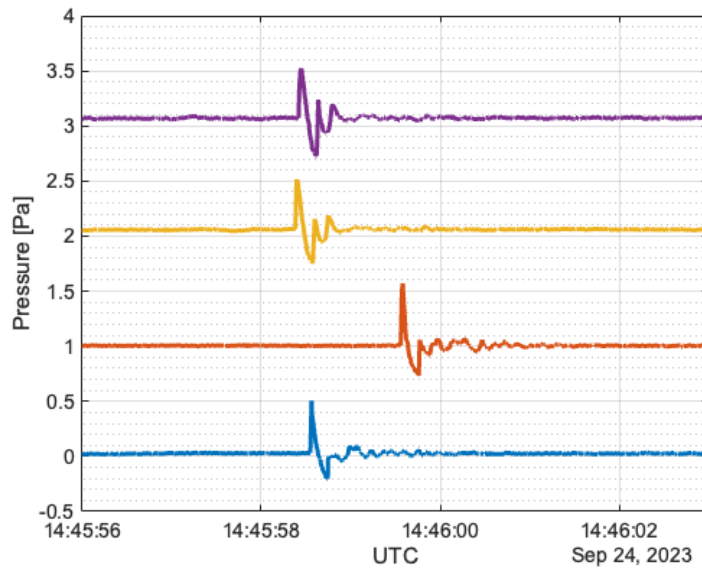
Figure S5: The signals recorded by the INF04 sensors deployed at EUE by KUT.
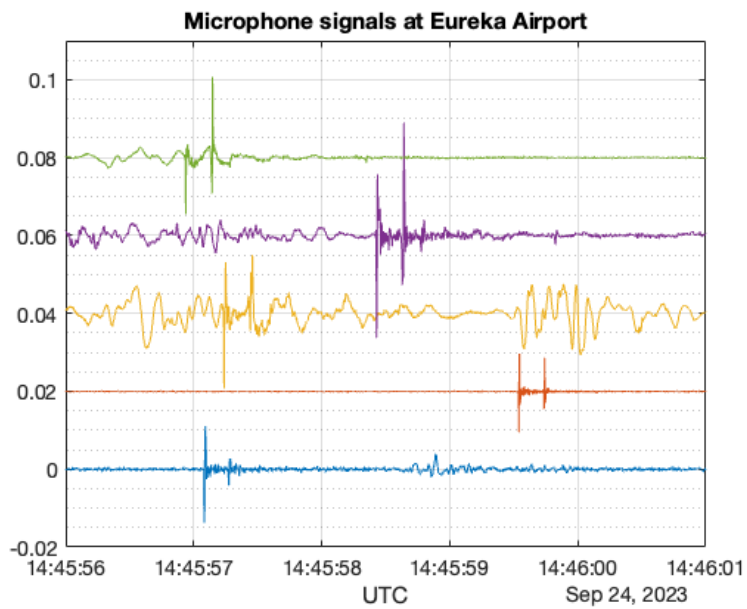
Figure S6: The signals recorded by microphones at EUE.

Oklahoma State University (OSU)

Deployment Photos
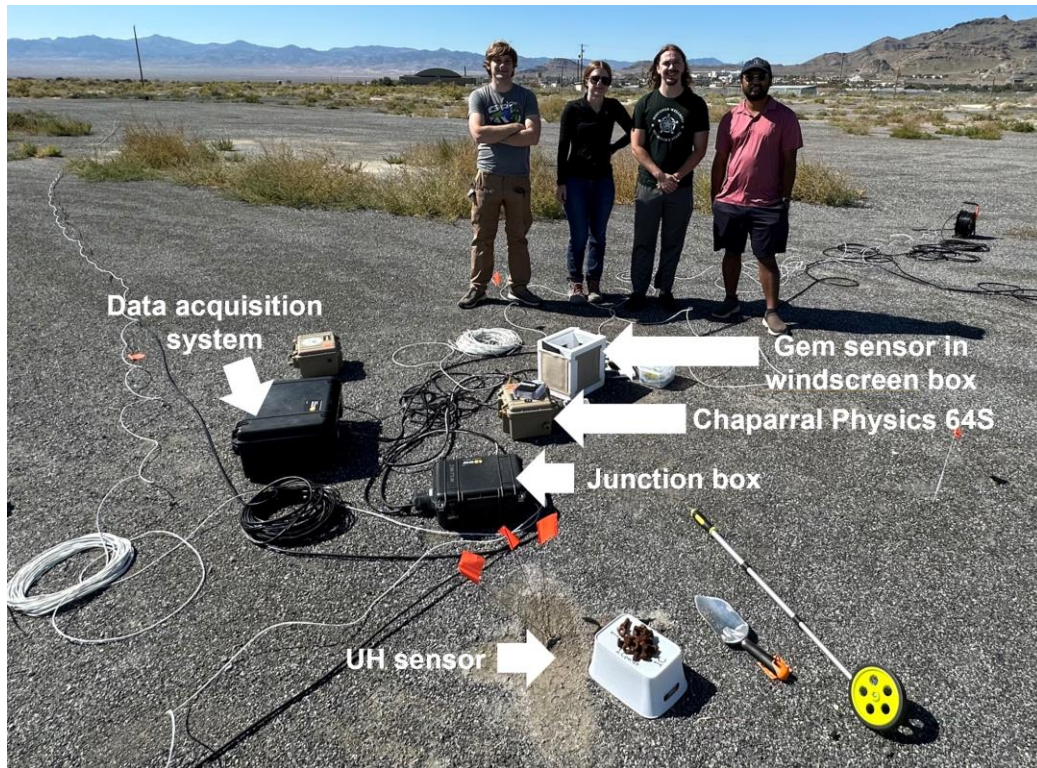
Figure S7: OSU Team (L to R: Douglas Fox, Kate Spillman, Trevor Wilson, and Real KC) at the Wendover Airport near the central location where four different sensors were co-located (Chaparral Physics 64s, GEM, WERD ISSM23, and RedVox deployed by the University of Hawaii). Photo credit: M. Garcés.

Figure S8: (a) Photo of the four Chaparral Physics 64s sensors in their cases before the OSIRIS-REx SRC re-entry deployment. (b) One of the Chaparral Physics sensors deployed near a RedVox sensor deployed by UH (photo credit: B. Elbing).
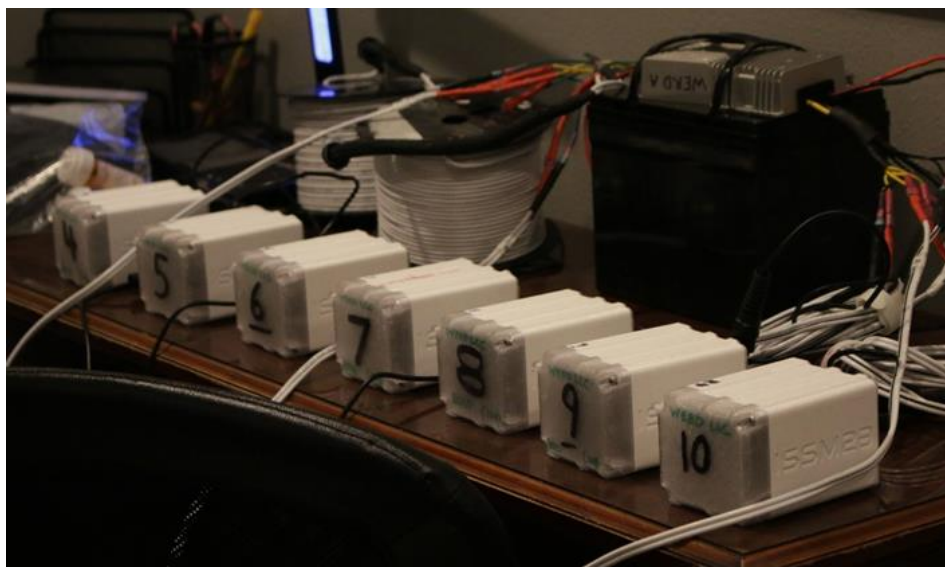
Figure S9: Picture of the seven WERD ISSM23 sensors being tested the night before the deployment for the OSIRIS-REx SRC re-entry deployment (photo credit: B. Elbing).
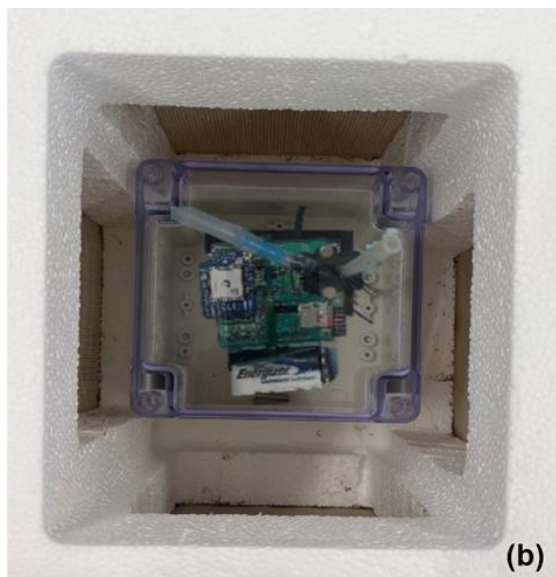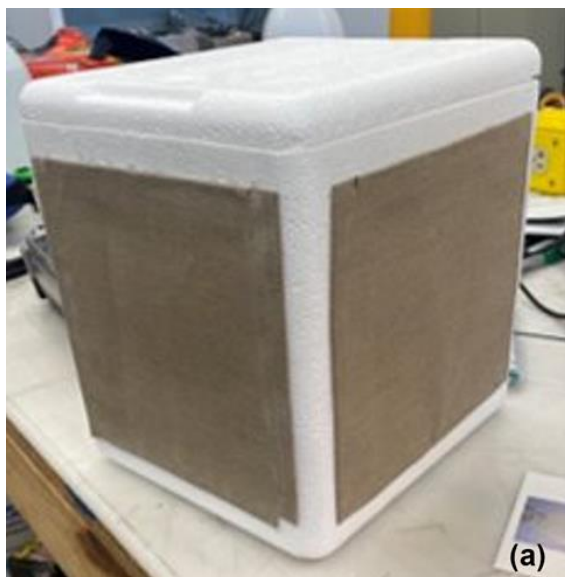
Figure S10: (a) Picture of one of the windscreen boxes (Swaim et al., 2023) that housed a GEM sensor. (b) View from above with the cover removed showing a single GEM sensor held within an enclosure and positioned within the windscreen box (photo credit: B. Elbing).

Signal Detection
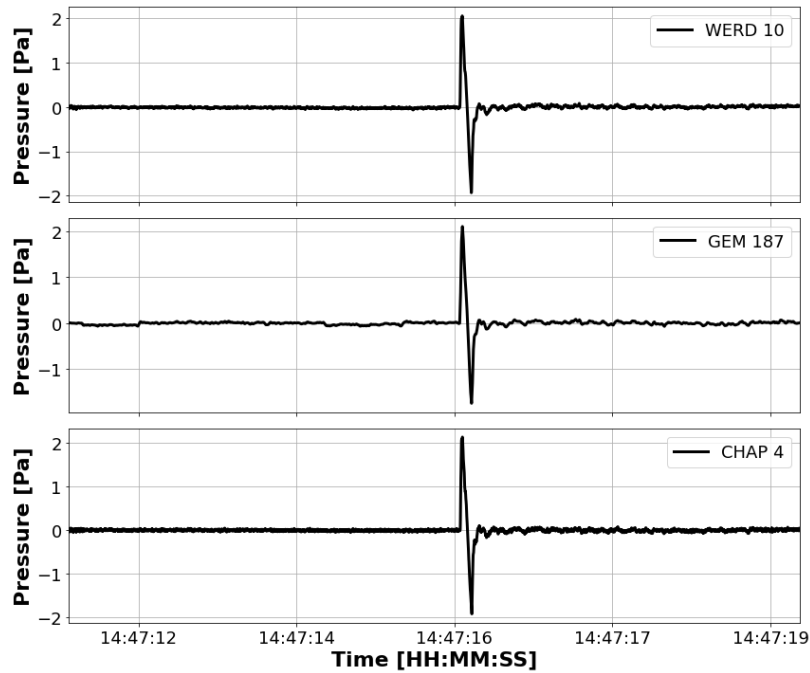
Figure S11: Signal detection at the West Wendover Airport, UT. The figure shows a comparison between the three sensor types used.

South Methodist University (SMU)

Signal Detection
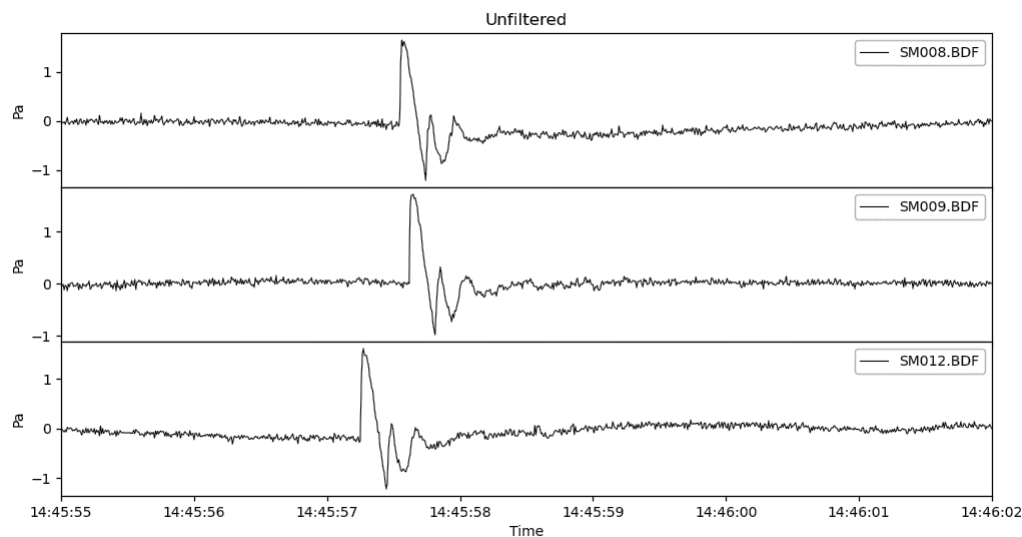
Figure S12: Signal detection at the Eureka Airport, NV. The timeseries shown are unfiltered. Time is shown in UTC.

Signal Detections
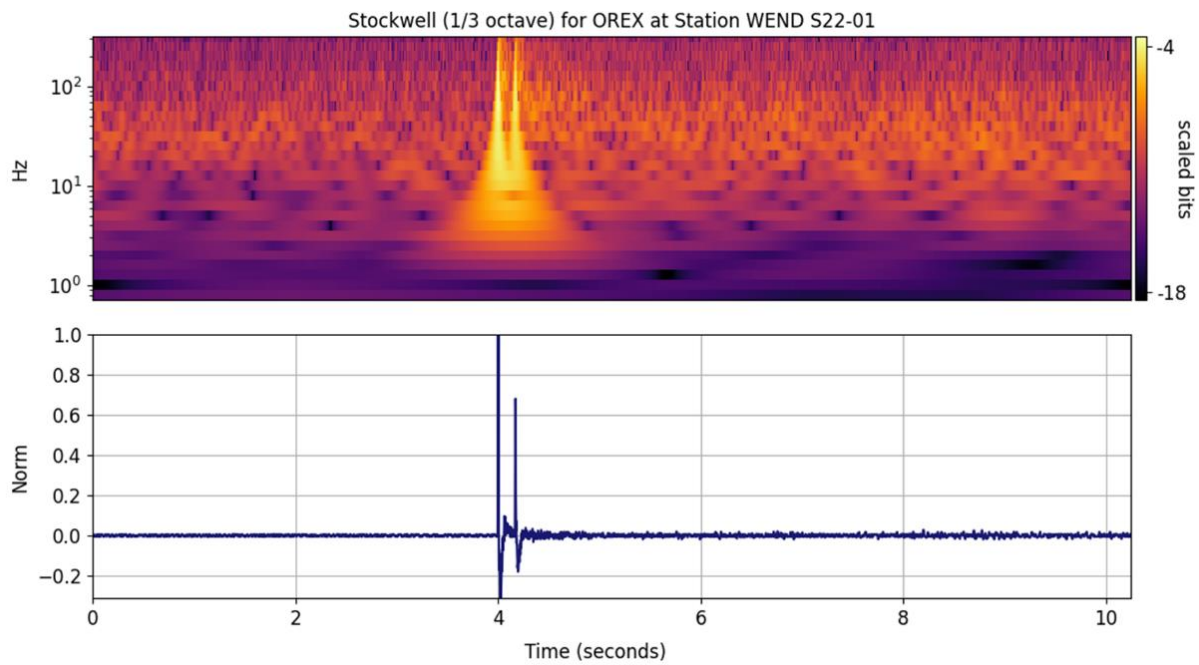
Figure S13: Signal detection at West Wendover Airport, UT. The time series in the lower panel shows the smartphone microphone equivalent high-pass filter response of the N-wave, the time between the two distinct peaks is the N wave duration. The upper panel shows the multiresolution time-frequency representation of the signal using a Stockwell transform (Garces, 2023), and showing the lower-frequency components of the N-wave. All channels of the Wendover array showed nearly identical waveforms time shifted by their arrival time.
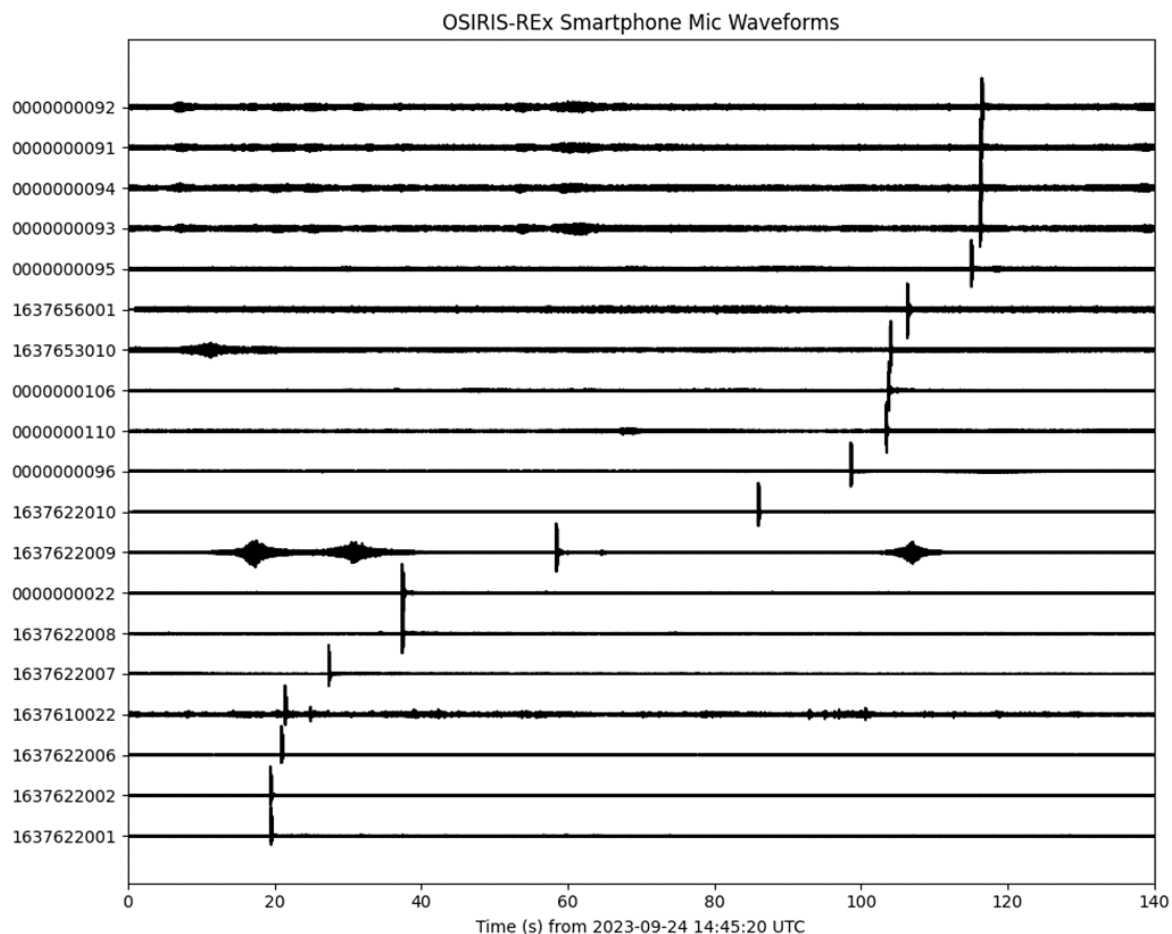
Figure S14: Detections made by smartphones, ordered by arrival time. The arrival waveforms and spectra are similar to those in Figure S13, but the N wave duration depends on the source height and speed. The timing of the arrivals corresponds to the time of closest approach of the source plus the time it would take to reach the station. This arrival pattern is only possible from hypersonic and supersonic sources.

University of Memphis (UM)

Figure S15: University of Memphis seismo-acoustic array experiment. Yellow triangles show the location of the 3 component seismic nodes in the Golay 3x6 array configuration (A1 through A18). Red triangles show the center infrasound instrument and co-located 3 component seismic node for the western and eastern infrasound arrays (A19 + IW1, A20 + IE1). Green triangles show locations for infrasound microphones. Green lines show locations for the P and SH refraction profiles near the western and eastern infrasound arrays. The red lines show the boundary of the airport property.
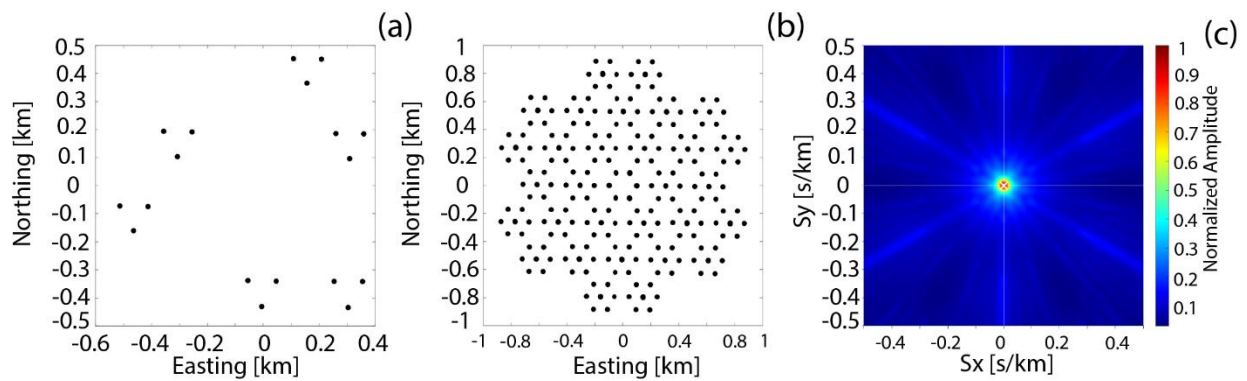
Figure S16: Geometry and response of the Golay 3x6 Array. (a) shows the OSIRIS-REx array design. (b) is the co-array which consists of distances and azimuths between all pairs of stations of the array. (c) is the broadband array response for a vertically incident plane wave for the frequency band 0.25 to 35Hz.

Appendix B

Table A1: Infrasound instrument installation data. This table is available in machine readable format.

Institution	Instrument field name	Instrument type	Sampling rate [Hz]	Location	Lat (N) [deg]	Lon (E) [deg]	Comments
SNL	C1	Gem	100	Utah	39.92841	-113.99949	Single sensor
SNL	C2	Gem	100	Utah	39.97127	-113.97749	Single sensor
SNL	C3	Gem	100	Utah	40.01614	-113.97312	Single sensor
SNL	C4	Gem	100	Utah	40.006113	-113.9766	Single sensor
SNL	C5	Gem	100	Utah	40.10518	-113.97008	Single sensor
SNL	C6	Gem	100	Utah	40.1518	-113.98394	Single sensor
SNL	C7	Gem	100	Utah	40.17377	-113.99698	Single sensor
SNL	C8	Gem	100	Utah	40.19454	-113.98697	Single sensor
SNL	C9	Gem	100	Utah	40.21743	-113.99005	Single sensor
SNL	C10	Gem	100	Utah	40.24075	-113.99157	Single sensor
SNL	C11	Gem	100	Utah	40.28813	-113.98843	Single sensor
SNL	A1	Gem	100	Eureka Airport	39.37657	-115.82061	Single sensor
SNL	A2	Gem	100	Eureka Airport	39.41789	-115.81251	Single sensor
SNL	A3	Gem	100	Eureka Airport	39.45742	-115.80031	Single sensor
SNL	A4	Gem	100	Eureka Airport	39.50356	-115.78451	Single sensor
SNL	A5	Gem	100	Eureka Airport	39.54794	-115.77042	Single sensor
SNL	A6	Gem	100	Eureka Airport	39.59715	-115.75859	Single sensor
SNL	A7	Gem	100	Eureka Airport	39.64012	-115.77885	Single sensor
SNL	A8	Gem	100	Eureka Airport	39.681	-115.7779	Single sensor
SNL	A9	Gem	100	Eureka Airport	39.72717	-115.76785	Single sensor
SNL	A10	Gem	100	Eureka Airport	39.74884	-115.77333	Single sensor
SNL	A11	Gem	100	Eureka Airport	39.77546	-115.76523	Single sensor
SNL	A12	Gem	100	Eureka Airport	39.81548	-115.75109	Single sensor

SNL	A13	Gem	100	Eureka Airport	39.86349	-115.73202	Single sensor
SNL	A14	Gem	100	Eureka Airport	39.91697	-115.73846	Single sensor
SNL	A15	Gem	100	Eureka Airport	39.96471	-115.74647	Single sensor
SNL	A16	Gem	100	Eureka Airport	40.01179	-115.76422	Single sensor
SNL	A17	Gem	100	Eureka Airport	40.05231	-115.77848	Single sensor
SNL	A18	Gem	100	Eureka Airport	40.09891	-115.7832	Single sensor
SNL	A19	Gem	100	Eureka Airport	40.14403	-115.75413	Single sensor
SNL	A20	Gem	100	Eureka Airport	40.19088	-115.74343	Single sensor
SNL	A21	Gem	100	Eureka Airport	40.23178	-115.70692	Single sensor
SNL	A22	Gem	100	Eureka Airport	40.26937	-115.68173	Single sensor
SNL	T1	Gem	100		39.54136	-116.38015	Single sensor
SNL	T2	Gem	100		39.55026	-116.33675	Single sensor
SNL	T3	Gem	100		39.58732	-116.20592	Single sensor
SNL	T4	Gem	100		39.60226	-116.1448	Single sensor
SNL	T5	Gem	100		39.63018	-116.04795	Single sensor
SNL	T6	Gem	100		39.67194	-115.90301	Single sensor
SNL	T7	Gem	100		39.71323	-115.7629	Single sensor
SNL	T8	Gem	100		39.74373	-115.6735	Single sensor
SNL	T10	Gem	100		40.04763	-114.64058	Single sensor
SNL	T11	Gem	100		40.06358	-114.58548	Single sensor
SNL	T12	Gem	100		40.07789	-114.53723	Single sensor
SNL	T13	Gem	100		40.09932	-114.54961	Single sensor
SNL	T14	Gem	100		40.18212	-114.01282	Single sensor
SNL	HA1-W	Hyperion	100		39.61691	-115.99818	Array
SNL	HA1-E	Hyperion	100		39.61691	-115.99764	Array
SNL	HA1-N	Hyperion	100		39.60727	-115.99791	Array
SNL	HA1-C	Hyperion	100		39.61705	-115.99794	Array
SNL	HA2-E	Hyperion	100		39.63933	-115.78173	Array
SNL	HA2-W	Ultra Light	100		39.63933	-115.78227	Array

SNL	HA2-C	Ultra Light	100		39.63945	-115.78200	Array
SNL	HA2-N	Hyperion	100		39.63969	-115.78200	Array
SNL	HA3-W	Hyperion	100		39.54036	-115.77476	Array
SNL	HA3-C	Hyperion	100		39.54048	-115.77450	Array
SNL	HA3-E	Hyperion	100		39.54036	-115.77423	Array
SNL	HA3-N	Hyperion	100		39.54072	-115.7745	Array
LANL	OREXA	Hyperion 3000	200		39.6109883	-116.002932	Single sensor
LANL	OREXB	Hyperion 3000	200		39.60899	-116.011737	Single sensor
LANL	OREXC	Hyperion 3000	200		39.6040443	-116.004643	Single sensor
LANL	OREXD	Hyperion 3000	200		39.7372017	-115.674093	Single sensor
LANL	OREXE	Hyperion 3000	200		39.7043	-115.676033	Single sensor
LANL	OREXF	Hyperion 3000	200		39.6858783	-115.676975	Single sensor
LANL	OREX1, e1	Hyperion IFS-3000	100	Price, UT	39.4751582	-110.7433235	Array
LANL	OREX1, e2	Hyperion IFS-3000	100	Price, UT	39.475359	-110.7451219	Array
LANL	OREX1, e3	Hyperion IFS-3000	100	Price, UT	39.4739251	-110.7449485	Array
LANL	OREX1, e4	Hyperion IFS-3000	100	Price, UT	39.474677	-110.7442959	Array
LANL	OREX3, e1	Hyperion IFS-3000	100	St George, UT	37.0151557	-113.616179	Array
LANL	OREX3, e2	Hyperion IFS-3000	100	St George, UT	37.0149832	-113.6170342	Array
LANL	OREX3, e3	Hyperion IFS-3000	100	St George, UT	37.0155959	-113.6171397	Array
LANL	OREX3, e4	Hyperion IFS-3000	100	St George, UT	37.0162369	-113.6170218	Array
LANL	OREX3, e5	Hyperion IFS-3000	100	St George, UT	37.0160341	-113.6162266	Array
LANL	OREX3, e6	Hyperion IFS-3000	100	St George, UT	37.0155697	-113.6161785	Array

LANL	OREX2, e1	Hyperion IFS-3000	500	NNSS, NV	37.224998	-116.149168	Array
LANL	OREX2, e2	Hyperion IFS-3000	500	NNSS, NV	37.223915	-116.149249	Array
LANL	OREX2, e3	Hyperion IFS-3000	500	NNSS, NV	37.223589	-116.148195	Array
LANL	OREX2, e4	Hyperion IFS-3000	500	NNSS, NV	37.224247	-116.1488	Array
UM	IW1	VLF Designs IAM-1	1000	Eureka Airport	39.61159286	-116.004319	Array
UM	IW2	VLF Designs IAM-1	1000	Eureka Airport	39.61172807	-116.0040416	Array
UM	IW3	VLF Designs IAM-1	1000	Eureka Airport	39.61178112	-116.0045212	Array
UM	IW4	VLF Designs IAM-1	1000	Eureka Airport	39.61133569	-116.0043187	Array
UM	IE1	VLF Designs IAM-1	1000	Eureka Airport	39.61150004	-115.997155	Array
UM	IE2	VLF Designs IAM-1	1000	Eureka Airport	39.61165862	-115.9968662	Array
UM	IE3	VLF Designs IAM-1	1000	Eureka Airport	39.61124095	-115.9972107	Array
UM	IE4	VLF Designs IAM-1	1000	Eureka Airport	39.61162776	-115.9974629	Array
KUT		microphone		Eureka Airport	39.6166	-115.9986	Single sensor
KUT		microphone		Eureka Airport	39.6165	-115.9974	Single sensor
KUT		INF04	100	Eureka Airport	39.6175	-115.9974	Array
KUT		INF04	100	Eureka Airport	39.6175	-115.9986	Array
KUT		INF04	100	Eureka Airport	39.6138	-116.0046	Array
KUT		microphone		Eureka Airport	39.6138	-116.0046	
KUT		INF04	100	Eureka Airport	39.5893	-116.0049	Array
KUT		microphone		Eureka Airport	39.5893	-116.0049	
BSU	JDSA1	GEM, Infrasound Loggers 1.01	100	Southwest Idaho	43.12185907	-116.7856059	Array

BSU	JDSA2	GEM, Infrasound Loggers 1.01	100	Southwest Idaho	43.12192087	-116.7855215	Array
BSU	JDSA3	GEM, Infrasound Loggers 1.01	100	Southwest Idaho	43.12178317	-116.7855284	Array
BSU	JDSA4	GEM, Infrasound Loggers 1.01	100	Southwest Idaho	43.12181649	-116.7856906	Array
BSU	JDSB1	GEM, Infrasound Loggers 1.01	100	Idaho	43.12157218	-116.7879959	Array
BSU	JDSB2	GEM, Infrasound Loggers 1.01	100	Idaho	43.12160936	-116.7879871	Array
BSU	JDSB3	GEM, Infrasound Loggers 1.01	100	Idaho	43.12155341	-116.7879649	Array
BSU	JDSB4	GEM, Infrasound Loggers 1.01	100	Idaho	43.12156295	-116.788055	Array
BSU	JDNB1	GEM, Infrasound Loggers 1.03	100	Idaho	43.12543365	-116.7875822	Array
BSU	JDNB2	GEM, Infrasound Loggers 1.04	100	Idaho	43.12547297	-116.7875298	Array
BSU	JDNB3	GEM, Infrasound Loggers 1.05	100	Idaho	43.12541687	-116.7875265	Array
BSU	JDNB4	GEM, Infrasound Loggers 1.06	100	Idaho	43.12543144	-116.7876213	Array
BSU	TOP01	GEM, Infrasound Loggers 1.08	100	Idaho	43.12550998	-116.8013974	Array
BSU	TOP02	GEM, Infrasound Loggers 1.09	100	Idaho	43.12560459	-116.8015603	Array
BSU	TOP03	GEM, Infrasoun	100	Idaho	43.12572902	-116.8017619	Array

		d Loggers 1.10					
BSU	TOP04	GEM, Infrasound Loggers 1.11	100	Idaho	43.12584698	-116.8019344	Array
BSU	TOP05	GEM, Infrasound Loggers 1.12	100	Idaho	43.12596533	-116.8020799	Array
BSU	TOP06	GEM, Infrasound Loggers 1.13	100	Idaho	43.12606252	-116.8021671	Array
BSU	TOP07	GEM, Infrasound Loggers 1.14	100	Idaho	43.12620928	-116.8023396	Array
BSU	TOP08	GEM, Infrasound Loggers 1.15	100	Idaho	43.12634974	-116.8024834	Array
BSU	TOP09	GEM, Infrasound Loggers 1.16	100	Idaho	43.12643686	-116.8026145	Array
BSU	TOP10	GEM, Infrasound Loggers 1.17	100	Idaho	43.12655189	-116.8027244	Array
BSU	TOP11	GEM, Infrasound Loggers 1.18	100	Idaho	43.12666905	-116.8028433	Array
BSU	TOP12	GEM, Infrasound Loggers 1.19	100	Idaho	43.12677948	-116.8030524	Array
BSU	TOP13	GEM, Infrasound Loggers 1.20	100	Idaho	43.12674003	-116.803228	Array
BSU	TOP14	GEM, Infrasound Loggers 1.21	100	Idaho	43.1266241	-116.8033681	Array
BSU	TOP15	GEM, Infrasound Loggers 1.22	100	Idaho	43.12663831	-116.8035886	Array
BSU	TOP16	GEM, Infrasound Loggers 1.23	100	Idaho	43.1265124	-116.8036435	Array

BSU	TOP17	GEM, Infrasound Loggers 1.24	100	Idaho	43.1264339	-116.8038132	Array
BSU	TOP18	GEM, Infrasound Loggers 1.25	100	Idaho	43.12634576	-116.8039767	Array
BSU	TOP19	GEM, Infrasound Loggers 1.26	100	Idaho	43.12624488	-116.804096	Array
BSU	TOP20	GEM, Infrasound Loggers 1.27	100	Idaho	43.12617945	-116.8042248	Array
BSU	TOP21	GEM, Infrasound Loggers 1.28	100	Idaho	43.1260073	-116.8041484	Array
BSU	TOP22	GEM, Infrasound Loggers 1.29	100	Idaho	43.12583556	-116.8039579	Array
BSU	TOP23	GEM, Infrasound Loggers 1.30	100	Idaho	43.12569345	-116.8037969	Array
BSU	TOP24	GEM, Infrasound Loggers 1.31	100	Idaho	43.12556656	-116.8036705	Array
BSU	TOP25	GEM, Infrasound Loggers 1.32	100	Idaho	43.12546093	-116.8035615	Array
BSU	TOP26	GEM, Infrasound Loggers 1.33	100	Idaho	43.1252966	-116.8034484	Array
BSU	TOP27	GEM, Infrasound Loggers 1.34	100	Idaho	43.1251737	-116.8032903	Array
BSU	TOP28	GEM, Infrasound Loggers 1.35	100	Idaho	43.12508251	-116.8030776	Array
BSU	TOP29	GEM, Infrasound Loggers 1.36	100	Idaho	43.12494683	-116.8029506	Array
BSU	TOP30	GEM, Infrasoun	100	Idaho	43.12481786	-116.8028627	Array

BSU							
		d Loggers 1.37					
BSU	TOP31	GEM, Infrasoun d Loggers 1.38	100	Idaho	43.124690 91	- 116.80277 94	Array
BSU	TOP32	GEM, Infrasoun d Loggers 1.39	100	Idaho	43.124723 95	- 116.80260 6	Array
BSU	TOP33	GEM, Infrasoun d Loggers 1.40	100	Idaho	43.124788 58	- 116.80246 12	Array
BSU	TOP34	GEM, Infrasoun d Loggers 1.41	100	Idaho	43.124902 61	- 116.80235 62	Array
BSU	TOP35	GEM, Infrasoun d Loggers 1.42	100	Idaho	43.124980 12	- 116.80221 25	Array
BSU	TOP36	GEM, Infrasoun d Loggers 1.43	100	Idaho	43.125083 85	- 116.80209 25	Array
BSU	TOP37	GEM, Infrasoun d Loggers 1.44	100	Idaho	43.125152 8	- 116.80194 92	Array
BSU	TOP38	GEM, Infrasoun d Loggers 1.45	100	Idaho	43.125231 29	- 116.80182 97	Array
BSU	TOP39	GEM, Infrasoun d Loggers 1.46	100	Idaho	43.125353 78	- 116.80169 28	Array
BSU	TOP40	GEM, Infrasoun d Loggers 1.47	100	Idaho	43.125392 79	- 116.80155 33	Array
BSU	TOP41	GEM, Infrasoun d Loggers 1.48	100	Idaho	43.125501 01	- 116.80198 04	Array
BSU	TOP42	GEM, Infrasoun d Loggers 1.49	100	Idaho	43.125448 89	- 116.80228 24	Array
BSU	TOP43	GEM, Infrasoun d Loggers 1.50	100	Idaho	43.125565 76	- 116.80258 17	Array

BSU	TOP44	GEM, Infrasound Loggers 1.51	100	Idaho	43.12561661	-116.8028346	Array
TDA	AA 1	TDA sensor	200	Eureka Airport	39.61752711	-115.9986176	Large N-array
TDA	AA 2	TDA sensor	200	Eureka Airport	39.61752834	-115.9986619	Large N-array
TDA	AA 3	TDA sensor	200	Eureka Airport	39.61754657	-115.998621	Large N-array
TDA	AA 4	TDA sensor	200	Eureka Airport	39.61752664	-115.9985874	Large N-array
TDA	AA 5	TDA sensor	200	Eureka Airport	39.61749151	-115.9986127	Large N-array
TDA	AB 1	TDA sensor	200	Eureka Airport	39.61752118	-115.9984251	Large N-array
TDA	AB 2	TDA sensor	200	Eureka Airport	39.6175235	-115.9984637	Large N-array
TDA	AB 3	TDA sensor	200	Eureka Airport	39.61754496	-115.9984252	Large N-array
TDA	AB 4	TDA sensor	200	Eureka Airport	39.61752115	-115.9983805	Large N-array
TDA	AB 5	TDA sensor	200	Eureka Airport	39.61748155	-115.9984185	Large N-array
TDA	AC 1	TDA sensor	200	Eureka Airport	39.61751905	-115.9982339	Large N-array
TDA	AC 2	TDA sensor	200	Eureka Airport	39.61753585	-115.9982558	Large N-array
TDA	AC 3	TDA sensor	200	Eureka Airport	39.61753085	-115.9982101	Large N-array
TDA	AC 4	TDA sensor	200	Eureka Airport	39.61750178	-115.9982132	Large N-array
TDA	AC 5	TDA sensor	200	Eureka Airport	39.61749968	-115.9982592	Large N-array
TDA	AD 1	TDA sensor	200	Eureka Airport	39.61752679	-115.9980451	Large N-array
TDA	AD 2	TDA sensor	200	Eureka Airport	39.61753938	-115.9980647	Large N-array

TDA	AD 3	TDA sensor	200	Eureka Airport	39.6175409 99	-115.9980263	Large N-array
TDA	AD 4	TDA sensor	200	Eureka Airport	39.6175080 2	-115.9980294	Large N-array
TDA	AD 5	TDA sensor	200	Eureka Airport	39.6175067 3	-115.9980685	Large N-array
TDA	AE 1	TDA sensor	200	Eureka Airport	39.6175257 8	-115.9978596	Large N-array
TDA	AE 2	TDA sensor	200	Eureka Airport	39.6175448 8	-115.9978823	Large N-array
TDA	AE 3	TDA sensor	200	Eureka Airport	39.6175433 4	-115.997839 9	Large N-array
TDA	AE 4	TDA sensor	200	Eureka Airport	39.6175081 4	-115.9978419	Large N-array
TDA	AE 5	TDA sensor	200	Eureka Airport	39.6175073 4	-115.9978785	Large N-array
TDA	AG 1	TDA sensor	200	Eureka Airport	39.6175045 9	-115.9973942	Large N-array
TDA	AG 2	TDA sensor	200	Eureka Airport	39.6175266 5	-115.9974294	Large N-array
TDA	AG 3	TDA sensor	200	Eureka Airport	39.6175272 6	-115.9973741	Large N-array
TDA	AG 4	TDA sensor	200	Eureka Airport	39.6174873 3	-115.9973661	Large N-array
TDA	AG 5	TDA sensor	200	Eureka Airport	39.6174738 2	-115.9974161	Large N-array
TDA	AO 1	TDA sensor	200	Eureka Airport	39.6172974 1	-115.9973552	Large N-array
TDA	AO 2	TDA sensor	200	Eureka Airport	39.6173284 5	-115.9973682	Large N-array
TDA	AO 3	TDA sensor	200	Eureka Airport	39.6173155 6	-115.9973271	Large N-array
TDA	AO 4	TDA sensor	200	Eureka Airport	39.6172718 2	-115.9973251	Large N-array
TDA	AO 5	TDA sensor	200	Eureka Airport	39.6172850 8	-115.9973932	Large N-array

TDA	AL 1	TDA sensor	200	Eureka Airport	39.61731577	-115.9980295	Large N-array
TDA	AL 2	TDA sensor	200	Eureka Airport	39.61733268	-115.9980542	Large N-array
TDA	AL 3	TDA sensor	200	Eureka Airport	39.61733605	-115.998002	Large N-array
TDA	AL 4	TDA sensor	200	Eureka Airport	39.61729622	-115.9980052	Large N-array
TDA	AL 5	TDA sensor	200	Eureka Airport	39.61729946	-115.9980556	Large N-array
TDA	AH 1	TDA sensor	200	Eureka Airport	39.61731637	-115.9985973	Large N-array
TDA	AH 2	TDA sensor	200	Eureka Airport	39.61730556	-115.9986386	Large N-array
TDA	AH 3	TDA sensor	200	Eureka Airport	39.61735896	-115.9985988	Large N-array
TDA	AH 4	TDA sensor	200	Eureka Airport	39.61732078	-115.9985483	Large N-array
TDA	AH 5	TDA sensor	200	Eureka Airport	39.61727528	-115.9985985	Large N-array
TDA	AP 1	TDA sensor	200	Eureka Airport	39.6171509	-115.9985694	Large N-array
TDA	AP 2	TDA sensor	200	Eureka Airport	39.61712029	-115.9985639	Large N-array
TDA	AP 3	TDA sensor	200	Eureka Airport	39.61714777	-115.9986103	Large N-array
TDA	AP 4	TDA sensor	200	Eureka Airport	39.61718634	-115.9985563	Large N-array
TDA	AP 5	TDA sensor	200	Eureka Airport	39.61715099	-115.9985163	Large N-array
TDA	AT 1	TDA sensor	200	Eureka Airport	39.61713803	-115.9980301	Large N-array
TDA	AT 2	TDA sensor	200	Eureka Airport	39.61711037	-115.9980552	Large N-array
TDA	AT 3	TDA sensor	200	Eureka Airport	39.61715787	-115.9980779	Large N-array

TDA	AT 4	TDA sensor	200	Eureka Airport	39.6171711 5	-115.99799 66	Large N-array
TDA	AT 5	TDA sensor	200	Eureka Airport	39.6171211 4	-115.99798 58	Large N-array
TDA	AW 1	TDA sensor	200	Eureka Airport	39.6171168 3	-115.99735 92	Large N-array
TDA	AW 2	TDA sensor	200	Eureka Airport	39.6171139 63	-115.99739 22	Large N-array
TDA	AW 3	TDA sensor	200	Eureka Airport	39.6171130 69	-115.99732 74	Large N-array
TDA	AW 4	TDA sensor	200	Eureka Airport	39.6170944 91	-115.99733 06	Large N-array
TDA	AW 5	TDA sensor	200	Eureka Airport	39.6170971 9	-115.99739 5	Large N-array
TDA	BE 1	TDA sensor	200	Eureka Airport	39.6168962 1	-115.99799 75	Large N-array
TDA	BE 2	TDA sensor	200	Eureka Airport	39.6169213 8	-115.99796 83	Large N-array
TDA	BE 3	TDA sensor	200	Eureka Airport	39.6168753 4	-115.99796 46	Large N-array
TDA	BE 4	TDA sensor	200	Eureka Airport	39.6168708 8	-115.99802 3	Large N-array
TDA	BE 5	TDA sensor	200	Eureka Airport	39.6169141 1	-115.99803 22	Large N-array
TDA	BB 1	TDA sensor	200	Eureka Airport	39.6169688 5	-115.99856 9	Large N-array
TDA	BB 2	TDA sensor	200	Eureka Airport	39.6169701 81	-115.99853 62	Large N-array
TDA	BB 3	TDA sensor	200	Eureka Airport	39.6169357 57	-115.99856 49	Large N-array
TDA	BB 4	TDA sensor	200	Eureka Airport	39.6169667 74	-115.998611 1	Large N-array
TDA	BB 5	TDA sensor	200	Eureka Airport	39.6170018 5	-115.99857 61	Large N-array
TDA	BI 1	TDA sensor	200	Eureka Airport	39.6167824 9	-115.99855 38	Large N-array

TDA	BI 2	TDA sensor	200	Eureka Airport	39.6167814 1	-115.9985191	Large N-array
TDA	BI 3	TDA sensor	200	Eureka Airport	39.6167568 4	-115.9985499	Large N-array
TDA	BI 4	TDA sensor	200	Eureka Airport	39.6167814 3	-115.9986053	Large N-array
TDA	BI 5	TDA sensor	200	Eureka Airport	39.6168184 7	-115.9985575	Large N-array
TDA	BL 1	TDA sensor	200	Eureka Airport	39.6166917 1	-115.9979882	Large N-array
TDA	BL 2	TDA sensor	200	Eureka Airport	39.6166775 3	-115.9979595	Large N-array
TDA	BL 3	TDA sensor	200	Eureka Airport	39.6166710 6	-115.9980087	Large N-array
TDA	BL 4	TDA sensor	200	Eureka Airport	39.6167066 6	-115.9980145	Large N-array
TDA	BL 5	TDA sensor	200	Eureka Airport	39.6167143 5	-115.9979715	Large N-array
TDA	BO 1	TDA sensor	200	Eureka Airport	39.6167325 7	-115.9973895	Large N-array
TDA	BO 2	TDA sensor	200	Eureka Airport	39.6167155 5	-115.9973527	Large N-array
TDA	BO 3	TDA sensor	200	Eureka Airport	39.6167096 8	-115.9974107	Large N-array
TDA	BO 4	TDA sensor	200	Eureka Airport	39.6167592 5	-115.997413	Large N-array
TDA	BO 5	TDA sensor	200	Eureka Airport	39.6167563 7	-115.9973539	Large N-array
TDA	BS 1	TDA sensor	200	Eureka Airport	39.6165019 4	-115.9979802	Large N-array
TDA	BS 2	TDA sensor	200	Eureka Airport	39.6164810 3	-115.9980106	Large N-array
TDA	BS 3	TDA sensor	200	Eureka Airport	39.6165210 7	-115.9980084	Large N-array
TDA	BS 4	TDA sensor	200	Eureka Airport	39.6165205 3	-115.9979524	Large N-array

TDA	BR 1	TDA sensor	200	Eureka Airport	39.61652715	-115.9981568	Large N-array
TDA	BR 2	TDA sensor	200	Eureka Airport	39.61649997	-115.9981276	Large N-array
TDA	BR 3	TDA sensor	200	Eureka Airport	39.61650461	-115.998182	Large N-array
TDA	BR 4	TDA sensor	200	Eureka Airport	39.61654842	-115.9981822	Large N-array
TDA	BR 5	TDA sensor	200	Eureka Airport	39.61654919	-115.9981286	Large N-array
TDA	BQ 1	TDA sensor	200	Eureka Airport	39.61653333	-115.9983295	Large N-array
TDA	BQ 2	TDA sensor	200	Eureka Airport	39.61649627	-115.9983174	Large N-array
TDA	BQ 3	TDA sensor	200	Eureka Airport	39.61652912	-115.9983727	Large N-array
TDA	BQ 4	TDA sensor	200	Eureka Airport	39.61656311	-115.998334	Large N-array
TDA	BQ 5	TDA sensor	200	Eureka Airport	39.61653614	-115.9982894	Large N-array
TDA	BP 1	TDA sensor	200	Eureka Airport	39.61654933	-115.998579	Large N-array
TDA	BP 2	TDA sensor	200	Eureka Airport	39.61654556	-115.9985301	Large N-array
TDA	BP 3	TDA sensor	200	Eureka Airport	39.61651148	-115.9985766	Large N-array
TDA	BP 4	TDA sensor	200	Eureka Airport	39.61655246	-115.9986164	Large N-array
TDA	BP 5	TDA sensor	200	Eureka Airport	39.6165886	-115.9985852	Large N-array
TDA	AX 1	TDA sensor	200	Eureka Airport	39.61646076	-115.9973911	Large N-array
TDA	AX 2	TDA sensor	200	Eureka Airport	39.61648133	-115.9974156	Large N-array
TDA	AX 3	TDA sensor	200	Eureka Airport	39.61648015	-115.9973568	Large N-array

TDA	AX 4	TDA sensor	200	Eureka Airport	39.6164330 4	-115.9973639	Large N-array
TDA	AX 5	TDA sensor	200	Eureka Airport	39.6164363 2	-115.9974145	Large N-array
TDA	BT 1	TDA sensor	200	Eureka Airport	39.6164591 7	-115.9976089	Large N-array
TDA	BT 2	TDA sensor	200	Eureka Airport	39.6164478 1	-115.9975688	Large N-array
TDA	BT 3	TDA sensor	200	Eureka Airport	39.6164409 4	-115.9976325	Large N-array
TDA	BT 4	TDA sensor	200	Eureka Airport	39.6164798 4	-115.9976417	Large N-array
TDA	BT 5	TDA sensor	200	Eureka Airport	39.6164835 8	-115.9975813	Large N-array
UH	redvox_1173028730		800	Eureka, NV	39.6008547 6	-116.0061335	Single station
UH	redvox_0000000022		800	Nevada	39.6172724 1	-115.9979189	Single station
UH	redvox_1637622001		800	Nevada	40.0603215 4	-114.525342	Single station
UH	redvox_1637622002		800	Nevada	40.0694193 6	-114.5299165	Single station
UH	redvox_1637622006		800	Nevada	40.1184172	-114.5319345	Single station
UH	redvox_1637622007		800	Nevada	40.2289711 7	-114.4351343	Single station
UH	redvox_1637622008		800	Nevada	40.3516639 4	-114.2376673	Single station
UH	redvox_1637622009		800	Nevada	40.4772614 3	-114.155499	Single station
UH	redvox_1637622010		800	Nevada	40.5926042 1	-114.1392218	Single station
UH	redvox_0000000096		800	Nevada	40.6452582 2	-114.1235271	Single station
UH	redvox_0000000095		800	Nevada	40.7109708 8	-114.0889773	Single station

UH	redvox_0000000094		800	West Wendover Airport	40.7278619	-114.0218836	Array
UH	redvox_0000000091		800	West Wendover Airport	40.72804373	-114.0211986	Array
UH	redvox_0000000093		800	West Wendover Airport	40.72782152	-114.0205354	Array
UH	redvox_0000000092		800	West Wendover Airport	40.728606	-114.0211872	Array
UH	redvox_1637653010		800	Nevada	40.7124639	-113.1244734	Single station
UH	redvox_0000000110		800	Clive, UT	40.70939688	-113.1214597	Single station
UH	redvox_0000000106		800	Clive, UT	40.7088681	-113.1167137	Single station
UH	redvox_1637656001		800	Clive, UT	40.7165156	-113.1127525	Single station
UH	redvox_0000000103		800	Dugway, UT	40.25711486	-112.7404369	Single station
UH	redvox_0000000104		800	Dugway, UT	40.25731765	-112.7404951	Single station
UH	redvox_1637610021		800	Nevada	39.69948222	-115.8906106	Single station
UH	redvox_1637610022		800	Eureka, NV	39.7076942	-115.8617927	Single station
INL	redvox_1637622022	Samsung S22	800	Idaho Falls, ID	43.65981128	-111.844751	Single station
INL	redvox_1637622023	Samsung S22	800	Idaho Falls, ID	43.49978502	-112.0490684	Single station
INL	redvox_1637622024	Samsung S22	800	Idaho Falls, ID	43.49979985	-112.0491303	Single station
INL	redvox_1637622025	Samsung S22	800	Idaho Falls, ID	43.50714182	-111.9710928	Single station
INL	redvox_1637622026	Samsung S22	800	Idaho Falls, ID	43.48783296	-112.0784373	Single station
INL	redvox_1637622029	Samsung S22	800	Idaho Falls, ID	43.49990583	-112.0491253	Single station

INL	redvox_163762220 30	Samsung S22	800	Idaho Falls, ID	43.487829 29	-112.07843 18	Single station
SMU	SN10	Sapphire		Eureka Airport	39.61727	-116.00037	Array
SMU	SN12	Sapphire		Eureka Airport	39.61704	-116.0004	Array
SMU	SN09	Sapphire		Eureka Airport	39.61691	-116.00064	Array
SMU	SN08	Sapphire		Eureka Airport	39.61691	-116.0001	Array
OSU	Loc04 - Center	Chaparral Physics, 64S	1000	West Wendov er Airport	40.7280	-114.0212	Array
OSU	Loc03	Chaparral Physics, 64S	1000	West Wendov er Airport	40.7286	-114.0211	Array
OSU	Loc02	Chaparral Physics, 64S	1000	West Wendov er Airport	40.7278	-114.0205	Array
OSU	Loc01	Chaparral Physics, 64S	1000	West Wendov er Airport	40.7279	-114.0219	Array
OSU	WERD 10 - center	WERD, ISSM 23	400	West Wendov er Airport	40.7280	-114.0212	Single sensor
OSU	WERD 9	WERD, ISSM 23	400	West Wendov er Airport	40.7282	-114.0210	Single sensor
OSU	WERD 7	WERD, ISSM 23	400	West Wendov er Airport	40.7278	-114.0213	Single sensor
OSU	WERD 5	WERD, ISSM 23	400	West Wendov er Airport	40.7281	-114.0214	Single sensor
OSU	WERD 3	WERD, ISSM 23	400	West Wendov er Airport	40.7281	-114.0218	Single sensor
OSU	WERD 6	WERD, ISSM 23	400	West Wendov er Airport	40.7276	-114.0219	Single sensor
OSU	WERD 4	WERD, ISSM 23	400	West Wendov er Airport	40.7278	-114.0222	Single sensor
OSU	GEM 185	GEM, 1.01 Flight version	100	West Wendov er Airport	40.7277	-114.0208	Single sensor
OSU	GEM 186	GEM, 1.01 Flight version	100	West Wendov er Airport	40.7281	-114.0208	Single sensor
OSU	GEM 187 - center	GEM, 1.01 Flight version	100	West Wendov er Airport	40.7280	-114.0212	Single sensor

OSU	GEM 074	GEM, 1.01 Flight version	100	West Wendover Airport	40.4924	-114.0425	Single sensor
OSU	GEM 092	GEM, 1.01 Flight version	100	West Wendover Airport	40.4254	-114.0155	Single sensor

Appendix C

Table A2: Seismic instrument installation data. This table is available in machine readable format.

Institution	Instrument field name	Latitude (N) [deg]	Longitude (E) [deg]	Comments
SNL	EA-S1	39.61727	-116.00026	
SNL	EA-S2	39.61551	-115.99598	
SNL	EA-S3	39.61203	-116.00454	
SNL	EA-S4	39.61013	-116.00019	
SNL	EA-S5	39.60808	-116.01050	
SNL	EA-S6	39.60755	-116.00766	
SNL	EA-S7	39.60702	-116.00482	
SNL	EA-S8	39.60623	-116.00057	
SNL	EA-S9	39.60286	-116.00646	
SNL	EA-S10	39.59980	-116.00269	
SNL	EA-S11	39.59782	-116.00742	
SNL	EA-S12	39.59347	-116.00436	
SNL	HA1-SNC	39.61702	-115.99792	Co-located with infrasound
SNL	HA1-SN	39.61727	-115.99791	Co-located with infrasound
SNL	HA2	39.63969	-115.78261	Co-located with infrasound
SNL	HA2	39.63945	-115.78200	Co-located with infrasound
SNL	HA3	39.54050	-115.77453	Co-located with infrasound
SNL	HA3	39.54073	-115.77453	Co-located with infrasound
LANL	OREXA	39.61099	-116.00293	Co-located with infrasound
LANL	OREXB	39.60899	-116.01174	Co-located with infrasound
LANL	OREXC	39.60404	-116.00464	Co-located with infrasound
LANL	OREXD	39.73720	-115.67409	Co-located with infrasound
LANL	OREXE	39.70430	-115.67603	Co-located with infrasound
LANL	OREXF	39.68588	-115.67698	Co-located with infrasound
UM	A1	39.61424	-115.99951	
UM	A2	39.61422	-115.99834	
UM	A3	39.61345	-115.99894	
UM	A4	39.61183	-115.99774	
UM	A5	39.61182	-115.99658	
UM	A6	39.61103	-115.99717	
UM	A7	39.60709	-115.99781	
UM	A8	39.60709	-115.99663	
UM	A9	39.60625	-115.99723	
UM	A10	39.60712	-116.00141	
UM	A11	39.60710	-116.00023	
UM	A12	39.60629	-116.00083	

UM	A13	39.60951	-116.00676	
UM	A14	39.60950	-116.00559	
UM	A15	39.60872	-116.00619	
UM	A16	39.61191	-116.00494	
UM	A17	39.61189	-116.00376	
UM	A18	39.61109	-116.00437	
UM	A19	39.61159	-116.00432	
UM	A20	39.61150	-115.99716	
UM	Refraction West	39.61113563	-116.00468	South end of line
UM	Refraction East	39.61096743	-115.99691	SouthWest end of line
JHU	S1	39.49957	-116.50945	Array centre
JHU	S2	39.49919	-116.51052	Uprange 1
JHU	S3	39.49883	-116.51157	Uprange 2
JHU	S4	39.49844	-116.51262	Uprange 3
JHU	S5	39.49790	-116.50855	South 1
JHU	S6	39.50036	-116.50994	North 1
JHU	S7	39.50117	-116.51045	North 2
JHU	S8	39.49991	-116.50838	Downrange 1
JHU	S9	39.50027	-116.50731	Downrange 2
JHU	S10	39.50060	-116.50623	Downrange 3
JHU	S11	39.49874	-116.50920	South 2

Appendix D

Table A3: GPS instrument installation data.

Institution	Instrument field name	Latitude (N) [deg]	Longitude (E) [deg]	Elevation [m]
LANL	West Runway	39.608664	-116.011496	1811.8
LANL	Mid-North Runway	39.607281	-116.004027	1810.4
LANL	Mid-South Runway	39.603620	-116.004756	1812.0
LANL	South Runway	39.595354	-116.007202	1814.4
LANL	North Runway	39.612798	-116.002877	1810.3

References

Afraimovich, E., Kosogorov, E., Perevalova, N., Plotnikov, A., 2001. The use of GPS arrays in detecting shock-acoustic waves generated during rocket launchings. Journal of Atmospheric and Solar-Terrestrial Physics 63, 1941-1957.

Ajluni, T., Everett, D., Linn, T., Mink, R., Willcockson, W., Wood, J., 2015. OSIRIS-REx, returning the asteroid sample, 2015 IEEE aerospace conference. IEEE, pp. 1-15.

Albert, S., Bowman, D., Silber, E., Dannemann Dugick, F., 2023. The AtmoSOFAR channel: First direct observations of an elevated acoustic duct. Earth and Space Science 10, e2023EA003149.

Anderson, J.F., Johnson, J.B., Bowman, D.C., Ronan, T.J., 2018. The Gem infrasound logger and custom-built instrumentation. Seismological Research Letters 89, 153-164.

Anderson, J.F., Johnson, J.B., Mikesell, T.D., Liberty, L.M., 2023. Remotely imaging seismic ground shaking via large-N infrasound beamforming. Communications Earth & Environment 4, 399.

Arrowsmith, S., Hale, J., Burlacu, R., Pankow, K., Stump, B., Hayward, C., Randall, G., Taylor, S., 2011. Infrasound Signal Characteristics from Small Earthquakes, 2011 Monitoring Research Review: Ground-Based Nuclear Explosion Monitoring Technologies.

Arrowsmith, S., ReVelle, D., Edwards, W., Brown, P., 2008a. Global Detection of Infrasonic Signals from Three Large Bolides. Earth, Moon, and Planets 102, 357-363.

Arrowsmith, S.J., Drob, D.P., Hedlin, M.A.H., Edwards, W., 2007. A joint seismic and acoustic study of the Washington State bolide: Observations and modeling. Journal of Geophysical Research 112, 1-14.

Arrowsmith, S.J., Hedlin, M.A.H., Stump, B., Arrowsmith, M.D., 2008b. Infrasonic Signals from Large Mining Explosions. Bulletin of the Seismological Society of America 98, 768-777.

Avdellidou, C., Vaubaillon, J., 2019. Temperatures of lunar impact flashes: mass and size distribution of small impactors hitting the Moon. Monthly Notices of the Royal Astronomical Society 484, 5212-5222.

Balachandran, N.K., Donn, W.L., 1971. Characteristics of Infrasonic Signals from Rockets. Geophysical Journal of the Royal Astronomical Society 26, 135-148.

Banfield, D., Spiga, A., Newman, C., Forget, F., Lemmon, M., Lorenz, R., Murdoch, N., Viudez-Moreiras, D., Pla-Garcia, J., Garcia, R.F., Lognonné, P., Karatekin, Ö., Perrin, C., Martire, L., Teanby, N., Hove, B.V., Maki, J.N., Kenda, B., Mueller, N.T., Rodriguez, S., Kawamura, T., McClean, J.B., Stott, A.E., Charalambous, C., Millour, E., Johnson, C.L., Mittelholz, A., Määttänen, A., Lewis, S.R., Clinton, J., Stähler, S.C., Ceylan, S., Giardini, D., Warren, T., Pike, W.T., Daubar, I., Golombek, M., Rolland, L., Widmer-Schnidrig, R., Mimoun, D., Beucler, É., Jacob, A., Lucas, A., Baker, M., Ansan, V., Hurst, K., Mora-Sotomayor, L., Navarro, S., Torres, J., Lepinette, A., Molina, A., Marin-Jimenez, M., Gomez-Elvira, J., Peinado, V., Rodriguez-Manfredi, J.-A., Carcich, B.T., Sackett, S., Russell, C.T., Spohn, T., Smrekar, S.E., Banerdt, W.B., 2020. The atmosphere of Mars as observed by InSight. Nature Geoscience 13, 190-198.

Belton, M.J., 2004. Mitigation of hazardous comets and asteroids. Cambridge University Press, Cambridge, UK.

Beshore, E., Lauretta, D., Boynton, W., Shinohara, C., Sutter, B., Everett, D., Gal-Edd, J., Mink, R., Moreau, M., Dworkin, J., 2015. The OSIRIS-REx asteroid sample return mission, 2015 ieee aerospace conference. IEEE, pp. 1-14.

Blaske, C.H., O'Rourke, J.G., Desch, S.J., Borrelli, M.E., 2023. Meteors May Masquerade as Lightning in the Atmosphere of Venus. Journal of Geophysical Research: Planets 128, e2023JE007914.

Blewitt, G., Hammond, W.C., Kreemer, C., Plag, H.-P., Stein, S., Okal, E., 2009. GPS for real-time earthquake source determination and tsunami warning systems. Journal of geodesy 83, 335-343.

Blom, P., Gammans, C., Delbridge, B., Carmichael, J.D., 2024. Prediction of regional infrasound produced by supersonic sources using a ray-based Mach cone source. The Journal of the Acoustical Society of America 155, 1667-1681.

Bowman, D., Lees, J., Cutts, J., Komjathy, A., Young, E., Seiffert, K., Boslough, M., Arrowsmith, S., 2019. Geoacoustic observations on drifting balloon-borne sensors, Infrasound monitoring for atmospheric studies. Springer, pp. 125-171.

Bowman, D.C., Albert, S.A., 2018. Acoustic event location and background noise characterization on a free flying infrasound sensor network in the stratosphere. Geophysical Journal International 213, 1524-1535.

Bowman, D.C., Krishnamoorthy, S., 2021. Infrasound from a buried chemical explosion recorded on a balloon in the lower stratosphere. Geophysical Research Letters 48, e2021GL094861.

Bowman, D.C., Lees, J.M., 2018. Upper Atmosphere Heating From Ocean-Generated Acoustic Wave Energy. Geophysical Research Letters 45, 5144-5150.

Brachet, N., Brown, D., Bras, R., Cansi, Y., Mialle, P., Coyne, J., 2010. Monitoring the Earth's Atmosphere with the Global IMS Infrasound Network, in: Le Pichon, A., Blanc, E., Hauchecorne, A. (Eds.), Infrasound Monitoring for Atmospheric Studies. Springer Netherlands, pp. 77-118.

Brissaud, Q., Krishnamoorthy, S., Jackson, J.M., Bowman, D.C., Komjathy, A., Cutts, J.A., Zhan, Z., Pauken, M.T., Izraelevitz, J.S., Walsh, G.J., 2021. The First Detection of an Earthquake From a Balloon Using Its Acoustic Signature. Geophysical Research Letters 48, e2021GL093013.

Bronshten, V.A., 1983. Physics of meteoric phenomena. Fizika meteornykh iavlenii, , Moscow, Izdatel'stvo Nauka, 1981 Dordrecht, D. Reidel Publishing Co, Dordrecht, Holland.

Brown, P., Spalding, R.E., ReVelle, D.O., Tagliaferri, E., Worden, S.P., 2002. The flux of small near-Earth objects colliding with the Earth. Nature 420, 294-296.

Brown, P.G., Assink, J.D., Astiz, L., Blaauw, R., Boslough, M.B., Borovicka, J., Brachet, N., Brown, D., Campbell-Brown, M., Ceranna, L., Cooke, W., de Groot-Hedlin, C., Drob, D.P., Edwards, W., Evers, L.G., Garces, M., Gill, J., Hedlin, M., Kingery, A., Laske, G., Le Pichon, A., Mialle, P., Moser, D.E., Saffer, A., Silber, E., Smets, P., Spalding, R.E., Spurny, P., Tagliaferri, E., Uren, D., Weryk, R.J., Whitaker, R., Krzeminski, Z., 2013. A 500-kiloton airburst over Chelyabinsk and an enhanced hazard from small impactors. Nature 503, 238-241.

Caudron, C., Taisne, B., Perttu, A., Garcés, M., Silber, E.A., Mialle, P., 2016. Infrasound and seismic detections associated with the 7 September 2015 Bangkok fireball. Geoscience Letters 3, 1-7.

Ceplecha, Z., Borovička, J., Elford, W.G., ReVelle, D.O., Hawkes, R.L., Porubčan, V., Šimek, M., 1998. Meteor Phenomena and Bodies. Space Science Reviews 84, 327-471.

Chapman, C.R., 2008. Meteoroids, Meteors, and the Near-Earth Object Impact Hazard. Earth, Moon, and Planets 102, 417-424.

Cumming, G.L., 1989. Alberta bolide of June 1, 1982: interpretation of photographic and seismic records. Canadian Journal of Earth Sciences 26, 1350-1355.

D'Auria, L., Marotta, E., Martini, M., Ricciolino, P., 2006. Seismic and acoustic detection of a bolide airburst in the Gulf of Naples (southern Italy). J. Geophys. Res. 111, B10307.

Daubar, I.J., Fernando, B.A., Garcia, R.F., Grindrod, P.M., Zenhäusern, G., Wójcicka, N., Teanby, N.A., Stähler, S.C., Posiolova, L., Horleston, A.C., Collins, G.S., Charalambous, C., Clinton, J., Banks, M.E., Froment, M., Lognonné, P., Panning, M., Banerdt, W.B., 2023. Two Seismic Events from InSight Confirmed as New Impacts on Mars. The Planetary Science Journal 4, 175.

den Ouden, O.F.C., Assink, J.D., Oudshoorn, C.D., Filippi, D., Evers, L.G., 2021. The INFRA-EAR: a low-cost mobile multidisciplinary measurement platform for monitoring geophysical parameters. Atmos. Meas. Tech. 14, 3301-3317.

Devillepoix, H.A.R., Cupák, M., Bland, P.A., Sansom, E.K., Towner, M.C., Howie, R.M., Hartig, B.A.D., Jansen-Sturgeon, T., Shober, P.M., Anderson, S.L., Benedix, G.K., Busan, D., Sayers, R., Jenniskens, P., Albers, J., Herd, C.D.K., Hill, P.J.A., Brown, P.G., Krzeminski, Z., Osinski, G.R., Aoudjehane, H.C., Benkhaldoun, Z., Jabiri, A., Guennoun, M., Barka, A., Darhmaoui, H., Daly, L., Collins, G.S., McMullan, S., Suttle, M.D., Ireland, T., Bonning, G., Baeza, L., Alrefay, T.Y., Horner, J., Swindle, T.D., Hergenrother, C.W., Fries, M.D., Tomkins, A., Langendam, A., Rushmer, T., O'Neill, C., Janches, D., Hormaechea, J.L., Shaw, C., Young, J.S., Alexander, M., Mardon, A.D., Tate, J.R., 2020. A Global Fireball Observatory. Planetary and Space Science 191, 105036.

Drolshagen, G., Koschny, D., Drolshagen, S., Kretschmer, J., Poppe, B., 2017. Mass accumulation of earth from interplanetary dust, meteoroids, asteroids and comets. Planetary and Space Science 143, 21-27.

Edwards, W.N., Eaton, D.W., Brown, P.G., 2008. Seismic observations of meteors: Coupling theory and observations. Reviews of Geophysics 46.

Edwards, W.N., Eaton, D.W., McCausland, P.J., ReVelle, D.O., Brown, P.G., 2007. Calibrating infrasonic to seismic coupling using the Stardust sample return capsule shockwave: Implications for seismic observations of meteors. Journal of Geophysical Research: Solid Earth 112.

Evans, L.B., Bass, H.E., Sutherland, L.C., 1972. Atmospheric Absorption of Sound: Theoretical Predictions. The Journal of the Acoustical Society of America 51, 1565-1575.

Evers, L.G., Haak, H.W., 2003. Tracing a meteoric trajectory with infrasound. Geophysical Research Letters 30, 1-4.

Fang, G., Li, Y.E., Zhao, Y., Martin, E.R., 2020. Urban Near-Surface Seismic Monitoring Using Distributed Acoustic Sensing. Geophysical Research Letters 47, e2019GL086115.

Fernando, B., Charalambous, C., Saliby, C., Sansom, E., Larmat, C., Buttsworth, D., Hicks, D., Johnson, R., Lewis, K., McCleary, M., Petricca, G., Schmerr, N., Zander, F., Inman, J., 2024. Seismoacoustic measurements of the OSIRIS-REx re-entry with an off-grid Raspberry PiShake. Seismica 3.

Fitzgerald, T.J., 1997. Observations of total electron content perturbations on GPS signals caused by a ground level explosion. Journal of Atmospheric and Solar-Terrestrial Physics 59, 829-834.

Followill, F.E., Wolford, J.K., Candy, J.V., 1997. Advanced array techniques for unattended ground sensor applications, United States.

Forbes, J.M., Roble, R.G., 1990. Thermosphere-ionosphere coupling: An experiment in interactive modeling. Journal of Geophysical Research: Space Physics 95, 201-208.

Francis, S.R., Johnson, M.A., Queen, E., Williams, R.A., 2024. Entry, Descent, and Landing Analysis for the OSIRIS-REx Sample Return Capsule, 46th Annual AAS Guidance, Navigation and Control (GN&C) Conference, Breckenridge, CO.

Fujita, K., Yamamoto, M.-y., Abe, S., Ishihara, Y., Iiyama, O., Kakinami, Y., Hiramatsu, Y., Furumoto, M., Takayanagi, H., Suzuki, T., Yanagisawa, T., Kurosaki, H., Shoemaker, M., Ueda, M., Shiba, Y., Suzuki, M., 2011. An Overview of JAXA's Ground-Observation Activities for HAYABUSA Reentry. Publications of the Astronomical Society of Japan 63, 961-969.

Garcés, M.A., Bowman, D., Zeiler, C., Christe, A., Yoshiyama, T., Williams, B., Colet, M., Takazawa, S., Popenhagen, S., 2022. Skyfall: Signal Fusion from a Smartphone Falling from the Stratosphere. Signals 3, 209-234.

Garcia, R.F., Daubar, I.J., Beucler, É., Posiolova, L.V., Collins, G.S., Lognonné, P., Rolland, L., Xu, Z., Wójcicka, N., Spiga, A., Fernando, B., Speth, G., Martire, L., Rajšić, A., Miljković, K., Sansom, E.K., Charalambous, C., Ceylan, S., Menina, S., Margerin, L., Lapeyre, R., Neidhart, T., Teanby, N.A., Schmerr, N.C., Bonnin, M., Froment, M., Clinton, J.F., Karatekin, O., Stähler, S.C., Dahmen, N.L., Durán, C., Horleston, A., Kawamura, T., Plasman, M., Zenhäusern, G., Giardini, D., Panning, M., Malin, M., Banerdt, W.B., 2022. Newly formed craters on Mars located using seismic and acoustic wave data from InSight. Nature Geoscience 15, 774-780.

Giardini, D., Lognonné, P., Banerdt, W.B., Pike, W.T., Christensen, U., Ceylan, S., Clinton, J.F., van Driel, M., Stähler, S.C., Böse, M., Garcia, R.F., Khan, A., Panning, M., Perrin, C., Banfield, D., Beucler, E., Charalambous, C., Euchner, F., Horleston, A., Jacob, A., Kawamura, T., Kedar, S., Mainsant, G., Scholz, J.R., Smrekar, S.E., Spiga, A., Agard, C., Antonangeli, D., Barkaoui, S., Barrett, E., Combes, P., Conejero, V., Daubar, I., Drilleau, M., Ferrier, C., Gabsi, T., Gudkova, T., Hurst, K., Karakostas, F., King, S., Knapmeyer, M., Knapmeyer-Endrun, B., Llorca-Cejudo, R., Lucas, A., Luno, L., Margerin, L., McClean, J.B., Mimoun, D., Murdoch, N., Nimmo, F., Nonon, M., Pardo, C., Rivoldini, A., Manfredi, J.A.R., Samuel, H., Schimmel, M., Stott, A.E., Stutzmann, E., Teanby, N., Warren, T., Weber, R.C., Wieczorek, M., Yana, C., 2020. The seismicity of Mars. Nature Geoscience 13, 205-212.

Gran, R., 2023. NASA Finds Likely Cause of OSIRIS-REx Parachute Deployment Sequence, in: NASA (Ed.), OSIRIS-REx Mission, NASA's Goddard Space Flight Center, Greenbelt, Maryland.

Hartog, A.H., 2017. An introduction to distributed optical fibre sensors. CRC press.

Ishihara, Y., 2004. The 2003 Kanto large bolide's trajectory determined from shockwaves recorded by a seismic network and images taken by a video camera. Geophysical Research Letters 31, 2-5.

Ishihara, Y., Hiramatsu, Y., Yamamoto, M.-y., Furumoto, M., Fujita, K., 2012. Infrasound/seismic observation of the Hayabusa reentry: Observations and preliminary results. Earth, Planets and Space 64, 655-660.

Janches, D., Heinselman, C.J., Chau, J.L., Chandran, A., Woodman, R., 2006. Modeling the global micrometeor input function in the upper atmosphere observed by high power and large aperture radars. Journal of Geophysical Research: Space Physics 111, A07317.

Jenniskens, P., Albers, J., Tillier, C.E., Edgington, S.F., Longenbaugh, R.S., Goodman, S.J., Rudlosky, S.D., Hildebrand, A.R., Hanton, L., Ciceri, F., Nowell, R., Lyytinen, E., Hladiuk, D., Free, D., Moskovitz, N., Bright, L., Johnston, C.O., Stern, E., 2018. Detection of meteoroid impacts by the Geostationary Lightning Mapper on the GOES-16 satellite. Meteoritics & Planetary Science 53, 2445-2469.

Kalashnikova, O., Horányi, M., Thomas, G.E., Toon, O.B., 2000. Meteoric smoke production in the atmosphere. Geophysical Research Letters 27, 3293-3296.

Krehl, P.O.K., 2011. Shock wave physics and detonation physics — a stimulus for the emergence of numerous new branches in science and engineering The European Physical Journal H36, 85-152.

Krishnamoorthy, S., Bowman, D.C., 2023. A "Floatilla" of Airborne Seismometers for Venus. Geophysical Research Letters 50, e2022GL100978.

Krishnamoorthy, S., Bowman, D.C., Komjathy, A., Pauken, M.T., Cutts, J.A., 2020. Origin and mitigation of wind noise on balloon-borne infrasound microbarometers. J. Acoust. Soc. Am. 148, 2361-2370.

Langston, C.A., 2004. Seismic ground motions from a bolide shock wave. Geophysical Research Lettters 109, 1-23.

Lauretta, D., Balram-Knutson, S., Beshore, E., Boynton, W., Drouet d'Aubigny, C., DellaGiustina, D., Enos, H., Golish, D., Hergenrother, C., Howell, E., 2017. OSIRIS-REx: sample return from asteroid (101955) Bennu. Space Science Reviews 212, 925-984.

Le Pichon, A., 2002. Trail in the atmosphere of the 29 December 2000 meteor as recorded in Tahiti: Characteristics and trajectory reconstitution. Journal of Geophysical Research 107, 1-10.

Lin, T.-L., Langston, C.A., 2009a. Thunder-induced ground motions: 1. Observations. Journal of Geophysical Research: Solid Earth 114.

Lin, T.-L., Langston, C.A., 2009b. Thunder-induced ground motions: 2. Site characterization. Journal of Geophysical Research: Solid Earth 114.

Lindsey, N.J., Martin, E.R., Dreger, D.S., Freifeld, B., Cole, S., James, S.R., Biondi, B.L., Ajo-Franklin, J.B., 2017. Fiber-Optic Network Observations of Earthquake Wavefields. Geophysical Research Letters 44, 11,792-711,799.

Lognonné, P., Banerdt, W.B., Pike, W.T., Giardini, D., Christensen, U., Garcia, R.F., Kawamura, T., Kedar, S., Knapmeyer-Endrun, B., Margerin, L., Nimmo, F., Panning, M., Tauzin, B., Scholz, J.R., Antonangeli, D., Barkaoui, S., Beucler, E., Bissig, F., Brinkman, N., Calvet, M., Ceylan, S., Charalambous, C., Davis, P., van Driel, M., Drilleau, M., Fayon, L., Joshi, R., Kenda, B., Khan, A., Knapmeyer, M., Lekic, V., McClean, J., Mimoun, D., Murdoch, N., Pan, L., Perrin, C., Pinot, B., Pou, L., Menina, S., Rodriguez, S., Schmelzbach, C., Schmerr, N., Sollberger, D., Spiga, A., Stähler, S., Stott, A., Stutzmann, E., Tharimena, S., Widmer-Schnidrig, R., Andersson, F., Ansan, V., Beghein, C., Böse, M., Bozdag, E., Clinton, J., Daubar, I., Delage, P., Fuji, N., Golombek, M., Grott, M., Horleston, A., Hurst, K., Irving, J., Jacob, A., Knollenberg, J., Krasner, S., Krause, C., Lorenz, R., Michaut, C., Myhill, R., Nissen-Meyer, T., ten Pierick, J., Plesa, A.C., Quantin-Nataf, C., Robertsson, J., Rochas, L., Schimmel, M., Smrekar, S., Spohn, T., Teanby, N., Tromp, J., Vallade, J., Verdier, N., Vrettos, C., Weber, R., Banfield, D., Barrett, E., Bierwirth, M., Calcutt, S., Compaire, N., Johnson, C.L., Mance, D., Euchner, F., Kerjean, L., Mainsant, G., Mocquet, A., Rodriguez Manfredi, J.A., Pont, G., Laudet, P., Nebut, T., de Raucourt, S., Robert, O., Russell, C.T., Sylvestre-Baron, A., Tillier, S., Warren, T., Wieczorek, M., Yana, C., Zweifel, P., 2020. Constraints on the shallow elastic and anelastic structure of Mars from InSight seismic data. Nature Geoscience 13, 213-220.

Luo, Y., Yao, Y., Shan, L., 2020. Analysis of Ionospheric Disturbances Caused by the 2018 Bering Sea Meteor Explosion Based on GPS Observations. Sensors 20, 3201.

Marcillo, O., Johnson, J.B., Hart, D., 2012. Implementation, Characterization, and Evaluation of an Inexpensive Low-Power Low-Noise Infrasound Sensor Based on a Micromachined Differential Pressure Transducer and a Mechanical Filter. Journal of Atmospheric and Oceanic Technology 29, 1275-1284.

Matoza, R., Fee, D., Green, D., Mialle, P., 2019. Volcano infrasound and the international monitoring system, Infrasound monitoring for atmospheric studies. Springer, pp. 1023-1077.

Matoza, R.S., Fee, D., Assink, J.D., Iezzi, A.M., Green, D.N., Kim, K., Toney, L., Lecocq, T., Krishnamoorthy, S., Lalande, J.-M., Nishida, K., Gee, K.L., Haney, M.M., Ortiz, H.D., Brissaud, Q., Martire, L., Rolland, L., Vergados, P., Nippress, A., Park, J., Shani-Kadmiel, S., Witsil, A., Arrowsmith, S., Caudron, C., Watada, S., Perttu, A.B., Taisne, B., Mialle, P., Le Pichon, A., Vergoz, J., Hupe, P., Blom, P.S., Waxler, R., De Angelis, S., Snively, J.B., Ringler, A.T., Anthony, R.E., Jolly, A.D., Kilgour, G., Averbuch, G., Ripepe, M., Ichihara, M., Arciniega-Ceballos, A., Astafyeva, E., Ceranna, L., Cevuard, S., Che, I.-Y., De Negri, R., Ebeling, C.W., Evers, L.G., Franco-Marin, L.E., Gabrielson, T.B., Hafner, K., Harrison, R.G., Komjathy, A., Lacanna, G., Lyons, J., Macpherson, K.A., Marchetti, E., McKee, K.F., Mellors, R.J., Mendo-Pérez, G., Mikesell, T.D., Munaibari, E., Oyola-Merced, M., Park, I., Pilger, C., Ramos, C., Ruiz, M.C., Sabatini, R., Schwaiger, H.F., Tailpied, D., Talmadge, C., Vidot, J., Webster, J., Wilson, D.C., 2022. Atmospheric waves and global seismoacoustic observations of the January 2022 Hunga eruption, Tonga. Science 377, 95-100.

Meech, K.J., Weryk, R., Micheli, M., Kleyna, J.T., Hainaut, O.R., Jedicke, R., Wainscoat, R.J., Chambers, K.C., Keane, J.V., Petric, A., Denneau, L., Magnier, E., Berger, T., Huber, M.E., Flewelling, H., Waters, C., Schunova-Lilly, E., Chastel, S., 2017. A brief visit from a red and extremely elongated interstellar asteroid. Nature 552, 378-381.

Miller, K.L., Torr, D.G., Richards, P.G., 1986. Meridional winds in the thermosphere derived from measurement of F 2 layer height. Journal of Geophysical Research: Space Physics 91, 4531-4535.

Moorhead, A.V., Brown, P.G., Campbell-Brown, M.D., Heynen, D., Cooke, W.J., 2017. Fully correcting the meteor speed distribution for radar observing biases. Planetary and Space Science 143, 209-217.

Mutschlecner, J., Whitaker, R., 2006. Infrasonic Signals from the Henderson, Nevada, Chemical Explosion, Los Alamos National Laboratory.

Nawab, S., Dowla, F., Lacoss, R., 1985. Direction determination of wideband signals. IEEE Transactions on Acoustics, Speech, and Signal Processing 33, 1114-1122.

Nishikawa, Y., Yamamoto, M.-y., Sansom, E.K., Devillepoix, H.A.R., Towner, M.C., Hiramatsu, Y., Kawamura, T., Fujita, K., Yoshikawa, M., Ishihara, Y., Hamama, I., Segawa, N., Kakinami, Y., Katao, H., Inoue, Y., Bland, P.A., 2022. Modeling of 3D trajectory of Hayabusa2 re-entry based on acoustic observations. Publications of the Astronomical Society of Japan 74, 308-317.

Nunn, C., Garcia, R.F., Nakamura, Y., Marusiak, A.G., Kawamura, T., Sun, D., Margerin, L., Weber, R., Drilleau, M., Wieczorek, M.A., Khan, A., Rivoldini, A., Lognonné, P., Zhu, P., 2020. Lunar Seismology: A Data and Instrumentation Review. Space Science Reviews 216, 89.

Obenberger, K., Bowman, D., Dao, E., 2022. Identification of acoustic wave signatures in the ionosphere from conventional surface explosions using MF/HF Doppler sounding. Radio Science 57, e2021RS007413.

Ortiz, H.D., Matoza, R.S., Tanimoto, T., 2022. Autocorrelation Infrasound Interferometry on Mars. Geophysical Research Letters 49, e2021GL096225.

Ortiz, J.L., Aceituno, F.J., Quesada, J.A., Aceituno, J., Fernández, M., Santos-Sanz, P., Trigo-Rodríguez, J.M., Llorca, J., Martín-Torres, F.J., Montañés-Rodríguez, P., Pallé, E., 2006. Detection of sporadic impact flashes on the Moon: Implications for the luminous efficiency of hypervelocity impacts and derived terrestrial impact rates. Icarus 184, 319-326.

Ortiz, J.L., Madiedo, J.M., Morales, N., Santos-Sanz, P., Aceituno, F.J., 2015. Lunar impact flashes from Geminids: analysis of luminous efficiencies and the flux of large meteoroids on Earth. Monthly Notices of the Royal Astronomical Society 454, 344-352.

Otsuka, Y., Kotake, N., Tsugawa, T., Shiokawa, K., Ogawa, T., Effendy, Saito, S., Kawamura, M., Maruyama, T., Hemmakorn, N., 2006. GPS detection of total electron content variations over Indonesia and Thailand following the 26 December 2004 earthquake. Earth, planets and space 58, 159-165.

Peña-Asensio, E., Visuri, J., Trigo-Rodríguez, J.M., Socas-Navarro, H., Gritsevich, M., Siljama, M., Rimola, A., 2024. Oort cloud perturbations as a source of hyperbolic Earth impactors. Icarus 408, 115844.

Perevalova, N., Shestakov, N., Voeykov, S., Takahashi, H., Guojie, M., 2015. Ionospheric disturbances in the vicinity of the Chelyabinsk meteoroid explosive disruption as inferred from dense GPS observations. Geophysical Research Letters 42, 6535-6543.

Pilger, C., Ceranna, L., Ross, J.O., Le Pichon, A., Mialle, P., Garcés, M.A., 2015. CTBT infrasound network performance to detect the 2013 Russian fireball event. Geophysical Research Letters 42, 2523-2531.

Pilger, C., Gaebler, P., Hupe, P., Ott, T., Drolshagen, E., 2020. Global Monitoring and Characterization of Infrasound Signatures by Large Fireballs. Atmosphere 11, 83.

Pilger, C., Hupe, P., Gaebler, P., Ceranna, L., 2021. 1001 Rocket Launches for Space Missions and Their Infrasonic Signature. Geophysical Research Letters 48, e2020GL092262.

Plane, J.M., 2012. Cosmic dust in the earth's atmosphere. Chemical Society Reviews 41, 6507-6518.

Plooster, M.N., 1970. Shock Waves from Line Sources. Numerical Solutions and Experimental Measurements. Physics of Fluids 13, 2665-2675.

Popenhagen, S.K., Bowman, D.C., Zeiler, C., Garcés, M.A., 2023. Acoustic Waves From a Distant Explosion Recorded on a Continuously Ascending Balloon in the Middle Stratosphere. Geophysical Research Letters 50, e2023GL104031.

Popova, O.P., Jenniskens, P., Emel'yanenko, V., Kartashova, A., Biryukov, E., Khaibrakhmanov, S., Shuvalov, V., Rybnov, Y., Dudorov, A., Grokhovsky, V.I., Badyukov, D.D., Yin, Q.-Z., Gural, P.S., Albers, J., Granvik, M., Evers, L.G., Kuiper, J., Kharlamov, V., Solovyov, A., Rusakov, Y.S., Korotkiy, S., Serdyuk, I., Korochantsev, A.V., Larionov, M.Y., Glazachev, D., Mayer, A.E., Gisler, G., Gladkovsky, S.V., Wimpenny, J., Sanborn, M.E., Yamakawa, A., Verosub, K.L., Rowland, D.J., Roeske, S., Botto, N.W., Friedrich, J.M., Zolensky, M.E., Le, L., Ross, D., Ziegler, K., Nakamura, T., Ahn, I., Lee, J.I., Zhou, Q., Li, X.-H., Li, Q.-L., Liu, Y., Tang, G.-Q., Hiroi, T., Sears, D., Weinstein, I.A., Vokhmintsev, A.S., Ishchenko, A.V., Schmitt-Kopplin, P., Hertkorn, N., Nagao, K., Haba, M.K., Komatsu, M., Mikouchi, T., 2013. Chelyabinsk Airburst, Damage Assessment, Meteorite Recovery, and Characterization. Science 342, 1069-1073.

Posiolova, L.V., Lognonné, P., Banerdt, W.B., Clinton, J., Collins, G.S., Kawamura, T., Ceylan, S., Daubar, I.J., Fernando, B., Froment, M., Giardini, D., Malin, M.C., Miljković, K., Stähler, S.C., Xu, Z., Banks, M.E., Beucler, É., Cantor, B.A., Charalambous, C., Dahmen, N., Davis, P., Drilleau, M., Dundas, C.M., Durán, C., Euchner, F., Garcia, R.F., Golombek, M., Horleston, A., Keegan, C., Khan, A., Kim, D., Larmat, C., Lorenz, R., Margerin, L., Menina, S., Panning, M., Pardo, C., Perrin, C., Pike, W.T., Plasman, M., Rajšić, A., Rolland, L., Rougier, E., Speth, G., Spiga, A., Stott, A., Susko, D., Teanby, N.A., Valeh, A., Werynski, A., Wójcicka, N., Zenhäusern, G., 2022. Largest recent impact craters on Mars: Orbital imaging and surface seismic co-investigation. Science 378, 412-417.

ReVelle, D., 1974. Acoustics of meteors.

ReVelle, D.O., 1976. On meteor-generated infrasound. Journal of Geophysical Research 81, 1217-1230.

Revelle, D.O., 1997. Historical Detection of Atmospheric Impacts by Large Bolides Using Acoustic-Gravity Wavesa. Annals of the New York Academy of Sciences 822, 284-302.

ReVelle, D.O., Edwards, W., Sandoval, T.D., 2005. Genesis—An artificial, low velocity "meteor" fall and recovery: September 8, 2004. Meteoritics & Planetary Science 40, 895-916.

ReVelle, D.O., Edwards, W.N., 2006. Stardust-An Artificial, Low Velocity "Meteor" Fall and Recovery: 15 January 2006.

Ronan, T.J., 2017. Fluvial seismo-acoustics: Characterizing temporally dependent river conditions through near river seismic and acoustic signals, p. 9.

Rosenblatt, B.B., Johnson, J.B., Anderson, J.F., Kim, K., Gauvain, S.J., 2022. Controls on the frequency content of near-source infrasound at open-vent volcanoes: A case study from Volcán Villarrica, Chile. Bulletin of Volcanology 84, 103.

Sansom, E.K., Devillepoix, H.A., Yamamoto, M.-y., Abe, S., Nozawa, S., Towner, M.C., Cupák, M., Hiramatsu, Y., Kawamura, T., Fujita, K., 2022. The scientific observation campaign of the Hayabusa-2 capsule re-entry. Publications of the Astronomical Society of Japan 74, 50-63.

Sarli, B.V., Tsuda, Y., 2017. Hayabusa 2 extension plan: Asteroid selection and trajectory design. Acta Astronautica 138, 225-232.

Scamfer, L.T., Anderson, J.F., 2023. Exploring Background Noise With a Large-N Infrasound Array: Waterfalls, Thunderstorms, and Earthquakes. Geophysical Research Letters 50, e2023GL104635.

Seyfried, M., Lohse, K., Marks, D., Flerchinger, G., Pierson, F., Holbrook, W.S., 2018. Reynolds Creek Experimental Watershed and Critical Zone Observatory. Vadose Zone Journal 17, 180129.

Shimada, S., Fujinawa, Y., Sekiguchi, S., Ohmi, S., Eguchi, T., Okada, Y., 1990. Detection of a volcanic fracture opening in Japan using Global Positioning System measurements. Nature 343, 631-633.

Silber, E.A., 2024. The utility of infrasound in global monitoring of extraterrestrial impacts: A case study of the 23 July 2008 Tajikistan bolide. The Astronomical Journal.

Silber, E.A., Boslough, M., Hocking, W.K., Gritsevich, M., Whitaker, R.W., 2018. Physics of meteor generated shock waves in the Earth's atmosphere – A review. Advances in Space Research 62, 489-532.

Silber, E.A., Bowman, D.C., Albert, S., 2023a. A Review of Infrasound and Seismic Observations of Sample Return Capsules since the End of the Apollo Era in Anticipation of the OSIRIS-REx Arrival. Atmosphere 14, 1473.

Silber, E.A., Bowman, D.C., Ronac Giannone, M., 2023b. Detection of the Large Surface Explosion Coupling Experiment by a sparse network of balloon-borne infrasound sensors. Remote Sensing 15, 542.

Silber, E.A., Brown, P., 2019. Infrasound Monitoring as a Tool to Characterize Impacting Near-Earth Objects (NEOs), in: Le Pichon, A., Blanc, E., Hauchecorne, A. (Eds.), Infrasound Monitoring for Atmospheric Studies: Challenges in Middle Atmosphere Dynamics and Societal Benefits. Springer International Publishing, Cham, pp. 939-986.

Silber, E.A., Brown, P.G., 2014. Optical observations of meteors generating infrasound—I: Acoustic signal identification and phenomenology. Journal of Atmospheric and Solar-Terrestrial Physics 119, 116-128.

Silber, E.A., ReVelle, D.O., Brown, P.G., Edwards, W.N., 2009. An estimate of the terrestrial influx of large meteoroids from infrasonic measurements. J. Geophys. Res. 114, E08006.

Slad, G., Merchant, B.J., 2021. Evaluation of Low Cost Infrasound Sensor Packages, United States.

Stopa, J.E., Cheung, K.F., Garcés, M.A., Badger, N., 2012. Atmospheric infrasound from nonlinear wave interactions during Hurricanes Felicia and Neki of 2009. Journal of Geophysical Research: Oceans 117.

Swaim, T., Spillman, K., Hough, E., Yap, Z., Jacob, J., Elbing, B., 2023. Development and evaluation of windscreen designs for high altitude balloons. Proceedings of Meetings on Acoustics 51.

Tatum, T.A., Anderson, J.F., Ronan, T.J., 2023. Whitewater Sound Dependence on Discharge and Wave Configuration at an Adjustable Wave Feature. Water Resources Research 59, e2023WR034554.

Trigo-Rodríguez, J.M., Dergham, J., Gritsevich, M., Lyytinen, E., Silber, E.A., Williams, I.P., 2021. A Numerical Approach to Study Ablation of Large Bolides: Application to Chelyabinsk. Advances in Astronomy 2021, 8852772.

Tsikulin, M., 1970. Shock waves during the movement of large meteorites in the atmosphere. DTIC Document AD 715-537, Nat. Tech. Inform. Serv., Springfield, Va

Vera Rodriguez, I., Isken, M.P., Dahm, T., Lamb, O.D., Wu, S.M., Kristjánsdóttir, S., Jónsdóttir, K., Sanchez-Pastor, P., Clinton, J., Wollin, C., 2023. Acoustic Signals of a Meteoroid Recorded on a Large-N Seismic Network and Fiber-Optic Cables. Seismological Society of America 94, 731-745.

Watanabe, J.-i., Ohkawa, T., Sato, M., Ohnishi, K., Iijima, Y., 2011. Fragmentation of the HAYABUSA Spacecraft on Re-Entry. Publications of the Astronomical Society of Japan 63, 955-960.

Whipple, F., 1930. The great Siberian meteor and the waves, seismic and aerial, which it produced. Quarterly Journal of the Royal Meteorological Society 56, 287-304.

Yamada, T., Yoshihara, K., 2022. Chapter 24 - Hayabusa2 sample-return capsule: System description and re-entry flight, in: Hirabayashi, M., Tsuda, Y. (Eds.), Hayabusa2 Asteroid Sample Return Mission. Elsevier, pp. 477-508.

Yamamoto, M.-y., Ishihara, Y., Hiramatsu, Y., Kitamura, K., Ueda, M., Shiba, Y., Furumoto, M., Fujita, K., 2011. Detection of acoustic/infrasonic/seismic waves generated by hypersonic re-entry of the HAYABUSA

capsule and fragmented parts of the spacecraft. Publications of the Astronomical Society of Japan 63, 971-978.

Yang, Y.-M., Komjathy, A., Langley, R.B., Vergados, P., Butala, M.D., Mannucci, A.J., 2014. The 2013 Chelyabinsk meteor ionospheric impact studied using GPS measurements. Radio Science 49, 341-350.